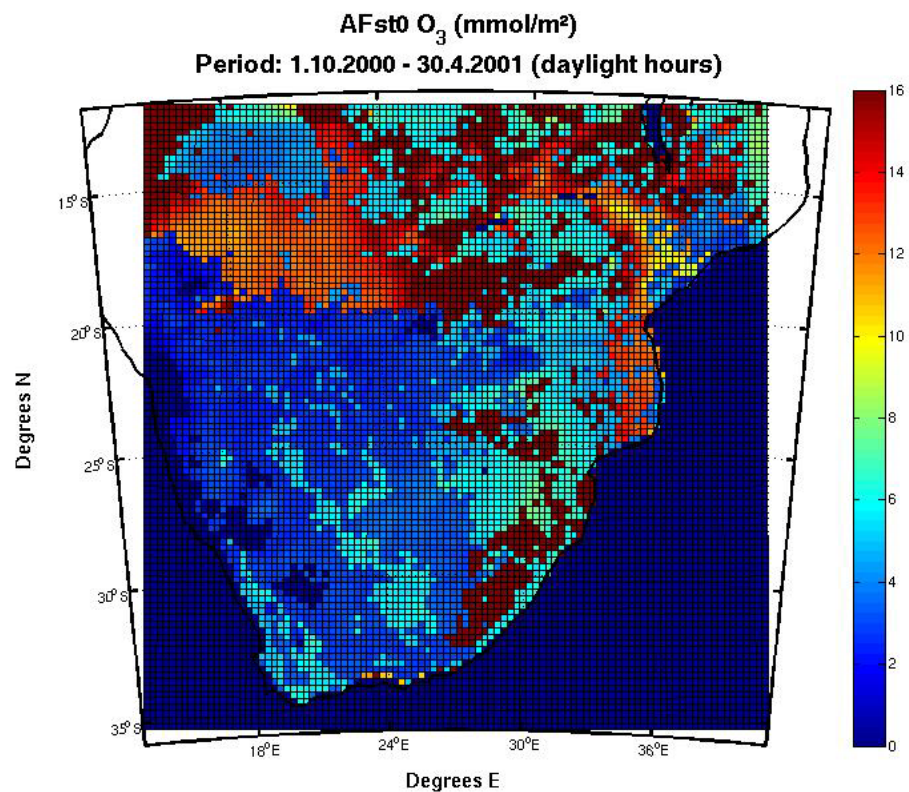


Formation of ozone due to chemical precursors and its impact on vegetation

Implementing WRF-Chem in parameterizing the dose of ozone to vegetation in the southern part of Africa

Johanne H. Rydsaa



UNIVERSITY OF OSLO

FACULTY OF MATHEMATICS AND NATURAL SCIENCES

Formation of ozone due to chemical precursors and its impact on vegetation

Implementing WRF-Chem in parameterizing the dose of ozone to vegetation in the southern part of Africa

Johanne H. Rydsaa



Master Thesis in Geosciences

Discipline: Meteorology

Department of Geosciences

Faculty of Mathematics and Natural Sciences

UNIVERSITY OF OSLO

15.06.2010

© Johanne H. Rydsaa, 2010

Tutor(s): Frode Stordal, Terje Berntsen (UiO)

This work is published digitally through DUO – Digitale Utgivelser ved UiO

<http://www.duo.uio.no>

It is also catalogued in BIBSYS (<http://www.bibsys.no/english>)

All rights reserved. No part of this publication may be reproduced or transmitted, in any form or by any means, without permission.

Intense research during the past few decades has established that the today's background concentration of ozone can cause adverse effects on vegetation. These effects include reduction in crop yield, tree growth and species composition. One main objective of this thesis is to provide an estimate of the total stomatal dose of ozone to the vegetation of the Southern African area over a maize growing season. For this purpose the WRF-Chem model is implemented, a mesoscale weather prediction system, fully coupled with a chemistry module. To validate the model, results for the stomatal flux are compared to fluxes derived from eddy covariance data gathered in Castelporziano, Italy, during the spring and summer period of 2007. Implementing dependance on the evaporative power of the ambient atmosphere is found to reduce overestimation of the modelled stomatal flux during dry periods.

The ozone concentrations simulated for Southern Africa are within the range of 20-45ppb, similar to those estimated for the same period by Zunckel et al.(2006). Peak values in the range of 70-100 ppb occurred throughout the period, values well above the threshold levels at which plant damage can be expected. The stomatal flux of ozone is accumulated to yield the total stomatal dose of ozone to the vegetation across the domain over the full 7 month period. The highest doses are found in the south-eastern part of the modelled domain, exceeding 16mmol/m² over the accumulation period. High doses reflect the combination of high mean ozone concentrations, sensitive land use categories, and low mean temperatures due to high geographical elevation.

Acknowledgements

I would like to first and foremost thank my supervisor Frode Stordal for his contagious enthusiasm, patience and encouraging guidance throughout the completion of this thesis.

Also, a big thanks to all of the helpful people of the MetOs section, especially Gunnar Wollan, the nice computer-oracle, always helpful and kind, for rescuing me on many occasions and always being helpful to solve any of my problems, self-made or other.

A very big thanks to Øivind Hodnebrog, for letting me use his emissions program, for all his help and guidance regarding the mysteries of WRF-Chem, for his patience and niceness, making it easy to ask even the silliest questions and always taking the time to answer them.

I would also like to thank my fellow students for encouragement, practical help, and many nice and much needed coffee-breaks. One fellow student in particular, Magnus, deserves extra big thanks for listening and supporting me in times of frustration

Finally, I would like to thank Dr. Giacomo Gerosa and his colleagues Angelo Finco, and Richardo Marzuoli for receiving us so warmly during our visit in Brechia in March, and for being so extremely helpful in meeting our every need for data for validation of the model, taking the time to screen and analyze data and provide both raw and screened, published and unpublished data for my thesis. It is greatly appreciated.



Picture taken during our visit in Brechia. From left: Angelo Finco, Frode Stordal, Johanne H. Rydsaa and Giacomo Gerosa.

March 15. 2010, Brechia, Italy.

Contents

Abstract

Acknowledgements	5
Contents.....	6
1 Introduction	8
1.1 Background.....	8
1.2 Purpose of study	9
2 Theory.....	10
2.1 Near Surface Ozone.....	10
2.1.1 Rules and guidelines	12
2.1.2 Precursors and their sources.....	13
2.1.3 Production and Loss of near Surface Ozone	18
2.2 Impact of ozone on vegetation	25
2.2.1 Plant physiology	27
2.2.2 Adverse effects	29
2.2.3 Risk assessment.....	30
3 Methods and Data	40
3.1 The Weather Research and Forecasting model (WRF)	40
3.2 WRF-Chem	42
3.3 Simulations and model setup	43
3.3.1 Simulations	43
3.3.2 Settings.....	45
3.3.3 Emissions.....	46
3.4 Dry deposition in WRF-Chem.....	47
3.5 Measured data	58
4 Results and Discussion	61
4.1 Castelporziano, Italy.....	61
4.1.1 Vapour Pressure Deficit limitations.....	77
4.2 Southern Africa	83
5 Summary and concluding remarks	94
5.1 Suggestions for future directions	96
Appendix A.....	97
List of figures.....	107
Bibliography	113

1 Introduction

1.1 Background

Extensive research over the recent decades has shown that the present day background concentrations of ozone are sufficiently high to cause adverse effects to both cultivated and wild vegetation, in addition to human health. The adverse effects of ozone on vegetation were first recognized in the 1950s, and have today been shown to cause reduction in crop yield, tree growth and species composition. Reduction in crop yield, and in crop economic value due to visible injuries, implies severe economic loss in many regions of the world. (Emberson, Ashmore et al. 2000; Ashmore 2005; Fowler 2008)

The background concentration in the Northern Hemisphere has more than doubled since pre-industrial times to reach the present day background concentration of 35-40ppb (Fowler 2008). The increase is a result of higher emissions of ozone precursor gasses, such as NO_x (NO and NO₂), volatile organic compounds (VOCs), and carbon monoxide (CO). The precursor gases are emitted from a wide range of both natural and anthropogenic sources. Peak concentration episodes exceeding present day guideline threshold values are still frequent in many regions of the world, despite efforts to control the emission of ozone precursors.

Precursor emissions in Europe and North America are today declining; however, increase in gaseous air pollution has been experienced in many rapidly industrializing countries of Asia, Africa and South America over the past few decades. This is mainly as a result of higher energy demand caused by rapid economic growth, industrialization and urbanization. Research has concluded that ozone at present day concentrations can have severe impacts on vegetation in many regions of developing countries. Predicted increase in the global ozone background concentrations combined with trends of increasing precursor emissions imply that the impact of ozone on crops and forests in many of these areas could be significant over the future decades (Ashmore 2005).

In the southern part of Africa there are a number of areas where air pollution in general and ozone in particular is perceived to be a problem. The South African Highveld is a highly industrialized and densely populated area with high emissions of ozone precursors, leading to high ozone concentrations in the surrounding areas (Emberson, Ashmore et al. 2000). Monitoring of the surface ozone concentrations across the area has shown that the concentrations often exceeds the threshold value of 40ppb, at which adverse effects on the vegetation can be expected. Zunckel et al (2006) found strong indications of risk of ozone induced damage on vegetation in the southern part of Africa. By modelling a domain covering the African mainland south of 13°S over the maize growing season of the year 2000, they found that ozone concentrations within the domain was sufficiently high to expect adverse effects on crops and forests within the area.

There are different metrics in use to predict and assess the risk of ozone-induced adverse effects to vegetation. The traditional ones are concentration based indices, based on the assumption that higher ambient air concentrations of ozone induce a higher risk of damage to the vegetation. However, it is today well established that the risk of damage to plants is more closely linked to the actual absorbed dose of ozone (Mills 2004; Ashmore 2005;

Simpson, Ashmore et al. 2007). Based on this, intense research conducted over the past decade has led to the development of flux based assessment strategies, with the ability to take into account the effect of climatic conditions on the uptake of ozone in vegetation. Most of this research has been done in Europe and North America.

1.2 Purpose of study

Zunckel et al. (2006) came to the conclusion that the ozone concentrations in the area of Southern Africa are high enough to cause adverse effects to vegetation in the area, an assessment based on the accumulated concentration index AOT40. To our knowledge little research has been done regarding flux-based risk assessment in the southern part of Africa. One main objective of this thesis is therefore to give an estimate of the accumulated flux of ozone to the vegetation in the southern part of Africa over a typical maize growing period. The seven month long growing season of 2000-2001 has been simulated to compare the results with the ones found by Zunckel et al. (2006). For this purpose the Weather Research and Forecasting model coupled with chemistry (WRF-Chem) has been applied.

A secondary objective is to validate the WRF-Chem estimates of the stomatal flux of ozone into the vegetation, by comparing modelled estimates with measurements gathered during a field campaign executed by Gerosa et al. (2009) in Castelporziano, Italy, during the spring and summer period of 2007. The findings of this validation are applied to the simulations of the Southern African domain, to provide an estimate of the total dose to the vegetation, and discuss the uncertainties within it.

The complex processes regulating the ambient air concentrations of ozone in the troposphere are highly dependent on the concentrations of ozone precursor gases in general, and NO_x in particular. Ozone as a natural component of the troposphere, and its role as an increasingly important air pollutant is presented in the first chapter, along with the main chemical processes of the different NO_x regimes in Chapter 2.1. The adverse effects of ozone as a toxic oxidant on vegetation are presented in more detail in Chapter 2.2, and different risk assessment strategies are presented.

A presentation of the WRF-Chem model is given in Chapter 3, with special focus on the dry deposition scheme, as it is especially important for the results of this study. Finally the results of the simulations are presented and discussed in Chapter 4. The simulations made in Italy, along with comparisons with measured results are presented first to give an indication of the model accuracy in predicting the stomatal flux. Possible improvement strategies are tested, and the results are applied to the final presentation of the total accumulated dose of ozone to vegetation in the Southern African domain over the maize growing season of 2000-2001.

A summary of the results and some concluding remarks are given in Chapter 5.

2 Theory

2.1 Near Surface Ozone

There are two major sources of ozone in the troposphere. The first one is transport from the stratosphere, the other one photochemical production in the troposphere. They have been estimated to account for roughly 540 Tg yr^{-1} and 4500 Tg yr^{-1} , respectively (Fowler 2008). The production processes are photochemical reactions between naturally or anthropogenically emitted precursor gasses such as NO_x and VOCs. This makes ozone a secondary pollutant. The reaction rates are controlled by the availability of the precursor gasses, meteorological conditions such as intensity of solar radiation, temperature, pressure, and the concentration of water vapour. There are two main sinks of ozone from the troposphere; destruction by photochemical processes, and destruction by dry deposition to the surface. The photochemical production and -destruction terms are by far the largest. Whether they yield a net production or destruction, and its efficiency, is determined by the availability of precursor gases and climatic conditions, as will be explained in Chapter 2.1.3. In the boundary layer, dry-deposition is the main sink, the modelling of which will be one of the main focuses of this thesis. The effect of dry deposition of ozone on vegetation is described in Chapter 2.2.

The average tropospheric lifetime of ozone has been estimated to be about 22 days (Brasseur, Orlando et al. 1999). It varies with height, from 1-2 days in the boundary layer, to several weeks higher up in the troposphere. As the lifetime of ozone increases with altitude, so does the transport-range. Both ozone and some ozone precursor gasses in the upper troposphere have tropospheric lifetimes long enough to be transported over vast distances, and thus can become important sources for ozone and ozone production in remote areas, making ozone not only a regional, but a global pollution problem.

The mean background concentration¹ of ozone in the Northern Hemisphere has more than doubled since pre-industrial times to reach the present day background concentration of 35-40ppb (Fowler 2008). Figure 2-1 shows modelled global concentrations of surface ozone in pre-industrial times compared to present day.

¹ The term “background concentration” describes the concentration of O_3 produced from naturally emitted precursor gasses within a region, together with O_3 transported to the region derived from all sources. It is the remaining concentration without the emissions of anthropogenic ozone precursors within the region.

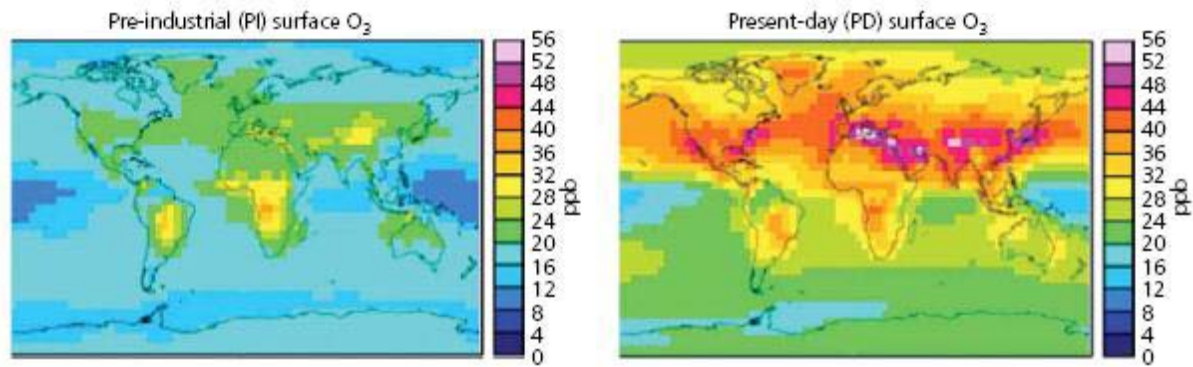


Figure 2-1: Modelled changes in surface ozone concentrations from pre-industrial times to 2008. Multi-model annual surface mean mixing ratio in ppb for pre-industrial times (left) and 2008 (right). (Modified from Fowler et al. 2008).

The lowest concentrations are found in the remote marine boundary layer, where there are low emissions of NO_x , inhibiting effective ozone production

Episodes of very high surface ozone concentration can occur in areas of high emissions under warm, sunny conditions. One example is France during the summer of 2003, where ozone mixing ratios in many cases exceeded 200ppb. In some cities in USA and South America, and some metropolitan areas in Asia, even values of 400 ppb are a common feature (Fowler et al. 2008, and references therein).

2.1.1 Rules and guidelines

The pollutonal impact of ground level ozone was first recognized in the 1950's, and measures to control ozone precursor emissions have been in place in USA and Japan since the 1960's, and in Europe since the 1970's. Since ozone hemispheric background only recently has received attention as a global problem, there have not been any measures taken yet to control ozone on a global scale. To avoid damage to human health the WHO guideline threshold value for ozone concentrations are 50ppb (daily 8 hour average) (WHO 2006). There are some regional agreements in place. Table 2-1 displays some of the air quality standards developed to control ozone.

Table 2-1: Air quality standards and other indices used for ozone. (From Fowler et al. (2008))

	Human Health	Vegetation
Global Measures		
The World Health Organization (WHO) provides guidelines for human health that are based on a combination of epidemiological and human exposure evidence	50 ppb daily 8-h mean	N/A
Regional Measures		
UNECE – Gothenburg Protocol EMEP² domain only	Critical level for human health 60 ppb as an 8-h average (expressed as AOT 60 for purposes of integrated assessment modeling)	Critical level to prevent significant yield loss in sensitive arable crops: AOT40 of 3000 ppb-h over a typical three month growing season* Critical level to prevent significant growth reduction in young trees: AOT40 of 5000 ppb-h accumulated over a growing season.
EU: The EU Directive on Ambient Air and Clean Air for Europe, defines targets to 2010 along with longer term objectives (timeframe not defined)	Target value: 60 ppb not to be exceeded on more than 25 days per year averaged over 3 years (maximum daily 8-h mean) (to be achieved by 2010) Longer term objective: 60 ppb (maximum daily 8-h mean) within a calendar year	Target value: AOT40 calculated from 1 hour values 9000 ppb-h over 3 months(May-July) averaged value over 5 years Long-term objective: AOT40 calculated from 1h values. 3000ppb-h over 3 months(May-July)
EU Alert threshold for O₃	Information threshold 90ppb per hour Alert threshold: 120ppb	N/A

*Metrics of risk assessment are presented in more detail in Chapter 2.2.3.

The Gothenburg protocol, which came into effect in 2005, sets a national legally binding emission ceilings for NO_x, VOC, ammonia and sulfur to 2010. The protocol has been ratified

² EMEP is the European Cooperative Programme for Monitoring and Evaluation of the Long-range Transmission of Air Pollutants in Europe.

by 24 countries within the UNECE region³. The UNECE region is the only area in the world with a regional policy framework in place to control ozone specifically.

As seen in Table 2-1, the AOT40 index is used to define critical levels of ozone for the protection against damage. This means that ozone exposure to sensitive crops should not exceed a concentration of 40ppb more than 3000 day lit hours accumulated over the course of a typical growing season. (More about the metrics of risk assessment in Chapter 2.2.3)

Other areas are also starting to take a more regional approach to handle general pollution and air quality issues. These may also affect the ozone levels over time. In Asia, the South Asian countries signed the 1998 Malé Declaration on control and prevention of air pollution and its likely transboundary effects in South Asia. In 2002 the Southeast Asian Nations (ASEAN) signed a legally binding agreement on transboundary haze pollution from land and forest fires. In the African region, the Air Pollution Information Network for Africa (APINA) aims to improve the African countries capacity to monitor and manage air pollution problems. APINA was founded in 1997 and acts as a link between different networks and programmes on air pollution in Africa. Southern Africa is APINA's region of main focus, but activities also are directed over the whole of Sub-Saharan Africa. In addition to these different networks and declarations, several regional networks are in place to improve urban air quality management.

2.1.2 Precursors and their sources

Ozone precursor gasses are emitted to the troposphere from a wide variety of both natural and anthropogenic sources. Species of shorter atmospheric lifetime will reflect the distribution of near-surface sources, while the distribution of longer lived species are mostly dominated by the main transport processes.

The most important precursor gasses are NO_x, which is the chemical group of NO and NO₂, carbon monoxide (CO), and volatile organic compounds (VOCs), commonly divided into methane and non-methane VOCs. As illustrated by Figure 2-2 the relative importance between them vary in different parts of the world, reflecting patterns of economic development and technological progress. Also control measures, land use and other environmental changes are important factors determining the precursor distribution

³ The UNECE region includes the EU, non-EU West-, East- and South East European countries, the Commonwealth of Independent States, North America and Canada (Fowler et al. 2008)

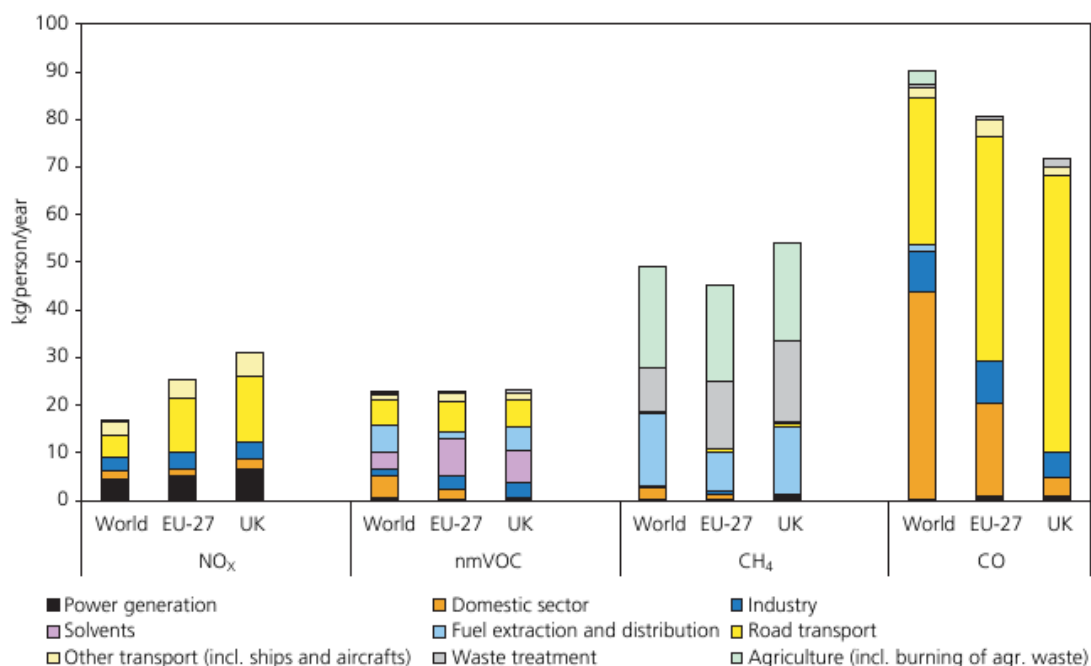
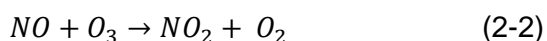
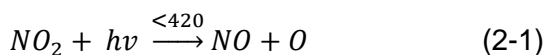


Figure 2-2: Per-capita emissions of the ozone precursors (NO_x, nmVOCs, CH₄, CO) in the year 2000, for the world, the EU-27 and the UK (From Fowler and et.al. 2008)

2.1.2.1 Odd Nitrogen, NO_x (NO and NO₂)

The emissions of odd nitrogen to the atmosphere are mostly on the form of NO. NO is readily oxidized to NO₂ (e.g by Reaction (2-2) and returns to NO by photolysis in the sunlight (Reaction 2-1)).



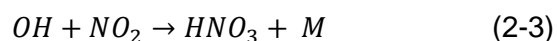
The primary anthropogenic sources of NO_x include various types of emissions from fossil fuel combustion, and contribute to a major fraction of the total release of odd nitrogen to the atmosphere. The emissions are, like combustion engines, often concentrated in densely populated and industrialized areas. Typical near ground mixing ratios are 2-5ppb in these areas.

Estimates of natural emissions of NO_x are highly uncertain. The main natural sources are lightening, volcanic activity and bacterial activity. The following estimates, based on Logan (1983), IPCC (1994) and Davidson (1991) are found in Brasseur et al. (1999):

Table 2-2: Global budget of NO_x in the Troposphere. (Brasseur et al. 1999)

Sources or Sinks	Range	Likely (TgN yr ⁻¹)
Sources		
Fossil fuel combustion	14-28	19,9
Biomass burning	4-24	12
Release from soils	4-40	20,2
Lightening discharges	2-20	8
NH ₃ oxidation	0-10	3
Ocean surface	<1	<1
Aircraft		0,5
Injection from the stratosphere	0,6 total NO	0,1
Total sources	25-112	64
Sinks		
Wet deposition of NO ₃ ⁻ (land)	8-30	19
Wet deposition of NO ₃ ⁻ (ocean)	4-12	8
Dry deposition of NO _x	12-22	16
Total sinks	24-64	43

The major sink of NO_x in the troposphere is by Reaction (2-3). In the boundary layer, dry deposition is also an important sink.



As HNO₃ is highly soluble in water, it is readily washed out of the lower troposphere, and normally only has a lifetime of a few days. Higher up, where the water vapour mixing ratio is lower, the HNO₃ lifetime can reach the order of weeks, making HNO₃ an important reservoir gas for NO_x.

2.1.2.2 Carbon Monoxide (CO)

Carbon monoxide is both released to the atmosphere and produced by the oxidation of methane and nmVOCs, the most important one being isoprene.

As illustrated in Figure 2-2 the most important anthropogenic emissions of carbon monoxide to the atmosphere vary greatly between different countries. The road transport sector is the most important per-capita emission of CO in the United Kingdom, while in many developing countries, emissions from savannah burning, deforestation and burning of agricultural waste are the most important anthropogenic CO sources, and account for about half of the anthropogenic CO emissions in the world.

The most important natural emissions of CO are from vegetation, oceans and wild forest fires, but these are negligible to the amount of the anthropogenic emissions.

The highest concentrations of CO are found in urban and suburban highly polluted areas, and in the tropics. As CO is readily oxidized by OH it has a relatively low atmospheric lifetime of about two months, and it is globally not well mixed. Average mixing ratios in the northern hemisphere are in the range of 120-180ppbv, on the southern about 60-70ppbv (Brasseur 1999). The estimates in Table 2-3 are found in Brasseur (1999).

Table 2-3: Global Budget for Carbon Monoxide (Tg yr⁻¹). Modified from Brasseur (1999) based on Khalil and Rasmussen (1990) and Bates et al. (1995).

Sources and sinks	Magnitude (Tg yr ⁻¹)
<i>Sources</i>	
Biomass burning	300-900
Fossil fuel burning	300-600
Vegetation	50-200
Oceans	6-30
Methane oxidation	400-1000
nmVOC oxidation	300-1000
Total	1400-3700
<i>Sinks</i>	
Chemical loss (OH)	1400-2600
Uptake by sinks	150-500
Total	1550-3100

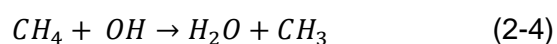
From Table 2-3 one can see that the main sources of CO in the troposphere are emissions from biomass- and fossil fuel burning, and production from methane and nmVOC oxidation.

2.1.2.3 Methane (CH₄)

Methane is the most abundant greenhouse gas in the troposphere after water vapour and CO₂. Methane has a tropospheric lifetime of several years, and is thus well mixed in the global troposphere. This gives methane an important role in the tropospheric chemistry in general, and in the photochemical production of ozone.

The average mixing ratio in the northern hemisphere troposphere has increased over the past two hundred years from a stable value of 700ppb, to the present day value of about 1750ppb.

The major sink of methane in the troposphere is oxidation by OH.



Methane is produced in soil and ocean as an end product in the decomposition of organic matter, and the production rate is highest in tropical wetlands.

The majority of the emissions today are from anthropogenic sources such as coal mining, natural gas loss, waste- and biomass burning, cultivated wetlands like rice paddies, ruminant animals and landfill. Also natural sources, such as swamps, lakes, tundra, boreal marches and termites, release a large amount of methane into the troposphere. The following estimates of methane sources and sinks in the atmosphere are from the IPCC (1994, 1996) and found in Brasseur (1999).

Table 2-4: Estimated Sinks and Sources of Methane in the Atmosphere (Tg CH₄ yr⁻¹).
(Modified from Brasseur (1999), from the IPCC (1994, 1996))

Sources and sinks	Range	Likely
<i>Natural</i>		
Wetlands	30-80	65
Termites	10-50	20
Ocean	5-50	10
Freshwater	1-25	5
Geological	5-15	10
<i>Total</i>		160
<i>Anthropogenic</i>		
Fossil fuel Related		100
Waste management		90
Enteric fermentation	65-100	85
Biomass Burning	20-80	40
Rice Paddies	20-100	60
<i>Total</i>		375
<i>Total Sources</i>		535
<i>Sinks</i>		
Reaction with OH	405-575	490
Removal in Stratosphere	32-48	40
Removal by soils	15-45	30
<i>Total sinks</i>		560
Atmospheric increase	35-40	37

2.1.2.4 Non-methane Volatile Organic Compounds (nmVOCs)

Non-methane VOCs are numerous, and a wide range of biogenic nmVOCs are emitted from different types of terrestrial plant species. The most important one is isoprene (C₅ H₈, 2-methyl-1, 3-butadiene) due to its high emission rate and reactivity with OH. Global emission rates have been estimated to be of the order of 500- 750 Tg y⁻¹. The release of emissions from vegetation is highly variable, and dependent on solar radiation and temperature. The oxidation chain of isoprene is complicated, and results in production of ozone if there is NO_x available.

Anthropogenically produced nmVOCs are not by far as abundant in the troposphere as natural ones and the emission rates are highly uncertain. As illustrated in Figure 2-2, the main emission sources are from solvents, transport-sector and the domestic sector in industrialized countries, and mostly from biomass-burning in many developing countries. Estimates of global emissions shown in Table 2-5 are found in Brasseur (1999).

Table 2-5: Estimates of Global nmVOC Emissions (Tg C yr⁻¹). Modified from Brasseur (1999), adapted from Singh and Zimmerman (1992), and Guenther et al. (1995).

Sources	Emissions (Tg C yr ⁻¹)
<i>Anthropogenic</i>	
Transportation	22
Stationary source fuel combustion	4
Industrial processes	17
Biomass burning, Forest fires	45
Organic solvents	15
<i>Total</i>	103
<i>Natural</i>	
<i>Oceanic</i>	
Light Hydrocarbons	5-10
C ₉ -C ₂₈ <i>n</i> -alkenes	1-26
<i>Terrestrial</i>	
Microbial production	6
<i>Emissions from vegetation</i>	
Isoprene	500
Monoterpenes	125
Other (extremely uncertain)	520
<i>Total</i>	~1170
<i>Total emissions</i>	~1273

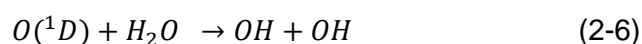
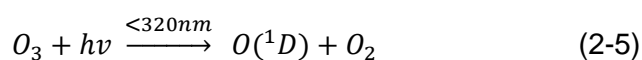
2.1.3 Production and Loss of near Surface Ozone

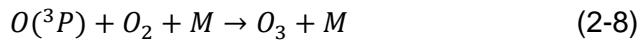
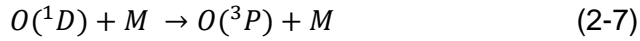
The average lifetime of ozone in the troposphere increases with altitude, from 1-2 days in the boundary layer, to a few weeks in the upper troposphere. In the following the main chemical production and loss processes are presented. In addition to chemical loss, the total loss rate is determined by dry deposition in the boundary layer, the details of which are presented in Chapter 2.2.

2.1.3.1 The Hydroxyl Radical (OH)

The hydroxyl radical (OH) is important in the photochemical production and loss mechanisms of ozone. OH initializes the oxidizing chains of CH₄, nmVOCs and CO, which in turn either produces or removes ozone, depending on the abundance of NO_x (see next section).

The primary source of OH is through the photolysis of ozone itself. At wavelengths shorter than 320nm, photolysis of ozone will produce photochemically excited oxygen atoms, O(¹D). These atoms have two possibilities. At lower altitudes, where the water vapour mixing ratio is high, the most efficient reaction is with H₂O to form hydroxyl radicals (2-6). At higher altitudes, the temperature decreases, and so does the water vapour mixing ratio. The fate of the majority of the excited oxygen atoms here will be to collide with some inert molecule, quenching it to ground state oxygen, O(³P) (2-7). O(³P) will in turn react with O₂ and re-form O₃ (2-8). The inert molecule M will most often be O₂ or N₂, as they are the most abundant gases in the troposphere.





The production efficiency of the hydroxyl radical will be determined by the reaction rates of reactions (2-6) and (2-7). It can then be expressed approximately as

$$\frac{d[OH]}{dt} = \frac{2k_{2-6}[H_2O]j_{O_3}[O_3]}{(k_{2-7})}$$

(2-9)

Where j_{O_3} is the rate constant for the photolysis of ozone into $O(^1D)$, k_{2-6} and k_{2-7} are the reaction rate coefficients.

As OH is highly reactive, its tropospheric lifetime is of a few seconds or less. The concentration is highly varying, and strongly dependent on the solar flux, the ozone concentration, and the abundance of hydrocarbon species.

2.1.3.2 The role of NO_x

The availability of NO_x determines if there will be a net production or net destruction of ozone in the atmosphere. Different cyclic processes dominate within the different mixing ratio ranges of NO_x , the efficiency of which determines the production and loss rates of ozone. Figure 2-3 illustrates the ozone production and loss of the different NO_x regimes. In the following the dominant processes of each NO_x regime are presented.

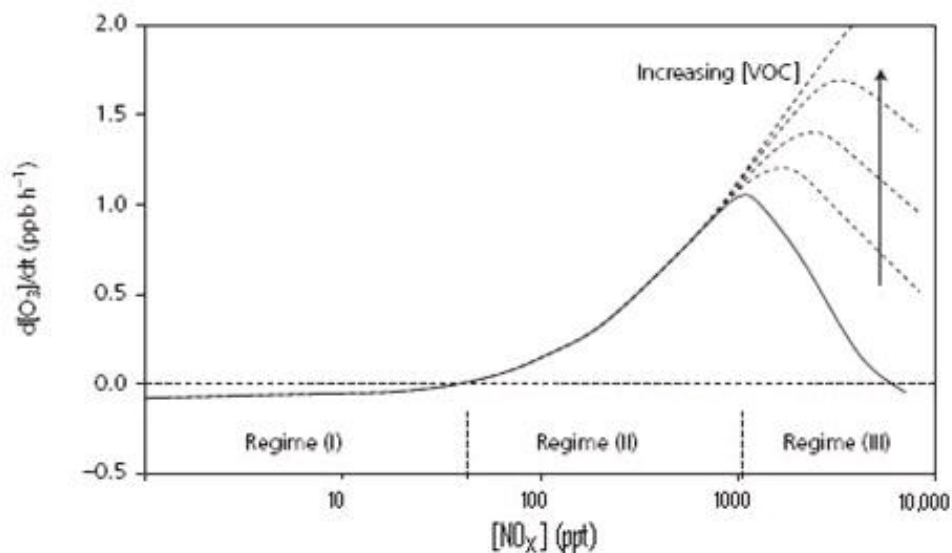
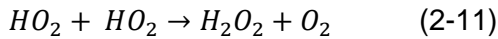
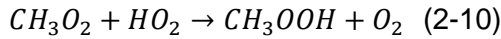


Figure 2-3: Ozone production and loss dependent on NO_x in different regimes The solid line corresponds to CH_4/CO oxidation, yielding either O_3 production or loss. Broken curves illustrate the effect of additional nmVOC inputs. (From Fowler et al. 2008)

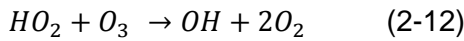
2.1.3.3 Very low NO_x

In the remote parts of the marine boundary layer the lowest values of NO_x concentrations are found. Mixing ratios in these regions can be less than ~55ppt NO_x, and characterized by a net ozone loss, as illustrated in Figure 2-3, regime 1.

As seen in Figure 2-4, the oxidation processes of CO and CH₄ produce peroxide radicals, which in low NO_x environments react with each other to produce chain terminating peroxides by reactions 2-10 and 2-11;



At near-zero NO_x concentrations terminating reactions compete with interconversion of HO_x resulting in catalytic loss of ozone by reactions 2-12 and 2-13;



Another important loss mechanism for ozone in lower, remote altitudes is the production reactions of OH radicals, as shown in Reactions (2-5) and (2-6).

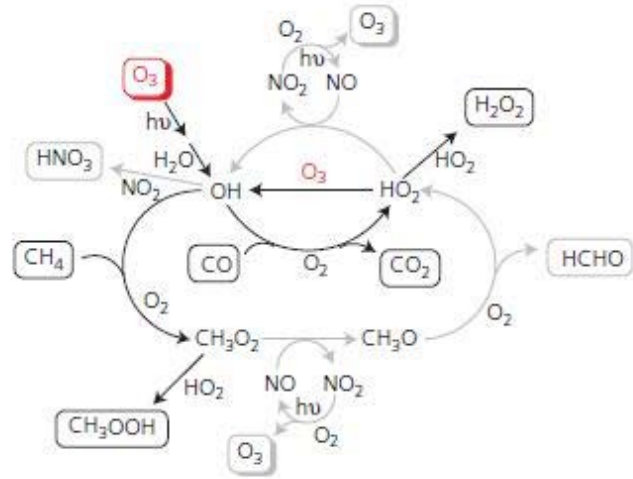


Figure 2-4: Schematic representation of the main O₃ production and loss processes in the very low-NO_x regime. The dominant processes are shown in black. From (Fowler and et.al. 2008).

The overall gross rate of photochemical destruction of ozone in these regions can be described as

$$L(O_3) = (fj_{2-5} + k_{2-12}[HO_2] + k_{2-13}[OH])[O_3]$$

(2-14)-

Where f is the fraction of $O(^1D)$ atoms from Reaction (2-5) that react with water vapor, resulting in the formation of OH, and can be expressed as

$$f = \frac{k_{2-6}[H_2O]}{k_{2-7}[M] + k_{2-6}[H_2O]}$$

(2-15)

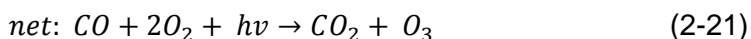
From Equation (2-15) we see that in regions of near-zero NO_x levels, the photochemical loss-rate of ozone increases with increasing ozone concentration. In some remote regions the loss rate is stably bigger than the production rate, resulting in a net loss of ozone. As transport of ozone to these regions only increases the rate of destruction, they can act as “buffer-zones” to increasing background ozone concentrations.

2.1.3.4 The Low NO_x case

The case of low to intermediate mixing ratios of NO_x, is typical for rural areas of most industrialized countries. Typical mixing ratios range from about 55ppt to 1000ppt. This regime is characterized by linearly increasing formation of O₃ with increasing NO_x mixing ratios as illustrated by Figure 2-3, regime 2.

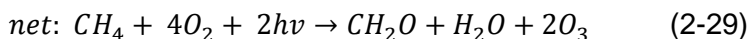
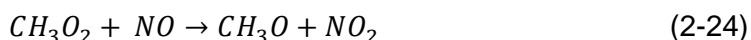
In this regime the NO_x mixing ratios are high enough to more efficiently compete with the chain terminating reactions of the previous regime, and the oxidation chains of CO and CH₄ serve as the main source of ozone. Even though the typical mean value of methane concentration is higher than that of CO, the rate coefficient of OH oxidation of CO is about 30 times higher than that of CH₄, and so the CO cycle is the most efficient one;

The CO cycle



As seen from the CO cycle, the CO oxidation by OH leads to the production of peroxide radical. While enough NO present, the peroxide radical will react with NO, leading to the conversion of NO to NO₂ resulting in the production of ozone.

The CH₄ cycle



For each methane oxidized, two peroxides are produced, as seen in the methane cycle, resulting in the production of two ozone molecules by reactions 2-23 to 2-28. The methane cycle also produces formaldehyde (CH₂O), as seen in Reaction 2-25, which in turn, under presence of NO_x, can be oxidized by OH to produce additional ozone.

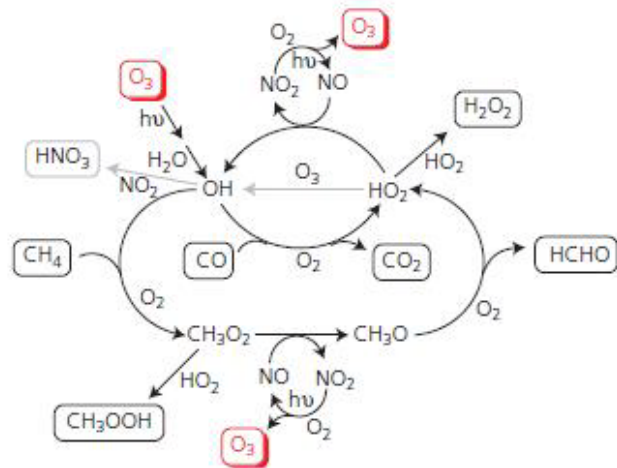
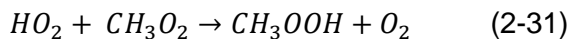
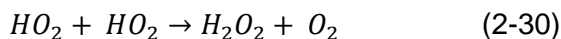


Figure 2-5: Schematic representation of the main O₃ production and loss processes in the low- NO_x regime. The dominant processes are shown in black. From (Fowle r et.al. 2008).

As in the previous regime, the rate limiting reactions of the ozone

production in this regime lies in the competitive reactions of the peroxide radicals produced in the oxidizing chains of CO and CH₄. As illustrated in Figure 2-5, the peroxide radicals can react with each other rather than NO, and thereby terminate the reaction chain leading to ozone production.



Assuming the peroxy radical concentration is nearly independent on the NO_x concentration in this regime, the ozone production rate can thus be expressed as;

$$P(O_3) = (k_{2-24}[HO_2] + k_{2-26}[CH_3O_2])[NO]$$

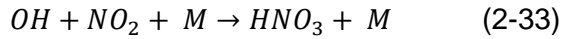
(2-32)

From Equation (2-32) it is apparent that the production rate in the low NO_x regime is independent on the CO and CH₄ input, and nearly linearly dependent on NO. As the ozone production rate is nearly linearly dependent on the NO_x input, this regime is characterized as NO_x-limited.

2.1.3.5 The high-NO_x case

Further increase of NO_x leads to mixing ratios of ~1-10ppb typically found in the continental boundary layer (CBL). In the CBL we find high emissions and concentrations of non-methane volatile organic compounds (nmVOCs), making the oxidation processes here much more complicated. In urban and suburban areas the anthropogenically emitted species of nmVOCs are dominant, while in rural areas, biogenically emitted ones like isoprene and terpene are the most abundant.

Compared to the remote atmosphere, the higher mixing ratios of both NO_x and VOCs in the continental boundary layer lead to much higher ozone production as well as loss rates. Higher mixing ratios of NO_x leads to increased loss of OH, mainly through the terminating reaction 2-33, leading to formation of the reservoir gas nitric acid.



As nitric acid is highly soluble in water it only has a lifetime of a few days in the lower troposphere, but if transported to higher elevations, can serve as an important reservoir gas for NO_x .

This implies that the formation of NO_2 no longer leads directly to ozone production, and the production rate is no longer linearly dependent on the NO_x concentration.

In addition to the described CO- and

CH_4 -oxidation cycles, the oxidation of nmVOCs is the dominant production cycles of ozone in this regime. There are countless variations of nmVOCs, but the generalized nmVOC oxidation chain can be expressed in the following way;

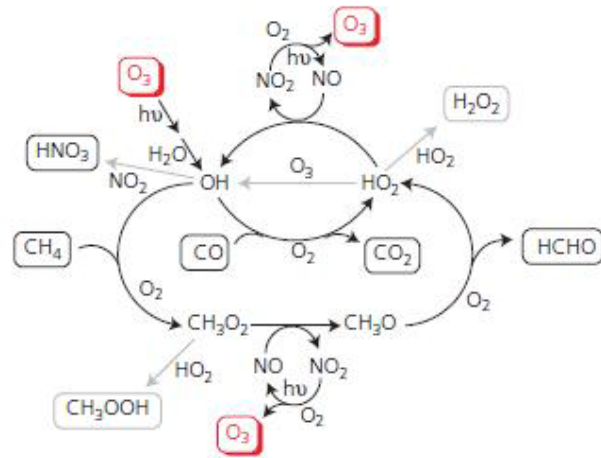
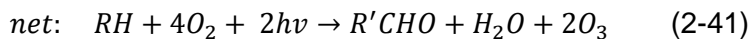
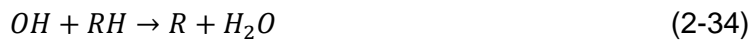


Figure 2-6: Schematic representation of the main O_3 production and loss processes in the high- NO_x regime. The dominant processes are shown in black. From (Fowler and et.al. 2008).

The generalized non-methane hydrocarbon cycle*



* RH : nm hydrocarbon

R : organic fragment

R' : organic fragment containing one less O atom than R

$R'CHO$: carbonyl products

Additional peroxy radicals may be produced through the continued oxidation of the carbonyl products of the nmVOC oxidation chain, amplifying the ozone production.

The gross chemical production rate of the high NO_x regime may be expressed as

$$P(\text{O}_3) = \left(k_{2-38}[\text{HO}_2] + \sum_{n=1}^i k_{2-36} [\text{RO}_2]_i \right) [\text{NO}]$$

(2-42)

To account for the many different nmVOCs we must sum over all of them and their representative rate coefficients to get the total ozone production rate.

From Equation (2-42) we see that the ozone production rate is strongly but non-linearly affected by the nmVOC/ NO_x ratio. As illustrated in Figure 2-3, regime 3, the more nmVOC present, the higher the production rate will be. This regime is therefore called VOC-limited.

The very high NO_x case

In addition to the three regimes illustrated in Figure 2-3, a fourth regime characterized by NO_x mixing ratios exceeding 10ppb are in some cases experienced in urban centres with high pollution. Under these conditions the large abundance of NO_x can lead to very low values of peroxide radicals. In lack of peroxide radicals, NO is oxidized by ozone directly, leading to what is called the ozone titration effect.



-if the NO_2 is lost to reservoir gas formation (e.g. by Reaction (2-33)) faster than photolysis of NO_2 leading to production of ozone again, the result is a net loss of ozone.

Due to this effect, control efforts made in polluted areas to control NO_x emissions during the past couple of decades, have in some cases lead to an unfortunate increase in ozone concentrations in some urban areas.

2.2 Impact of ozone on vegetation

The adverse effect of ozone on vegetation was first recognized in the 1950s and is today well documented (Fowler 2008). Field experiments from Europe and North America, and a few from Asia, Africa and Latin America, show that current day ozone background concentrations cause economic loss due to reductions in crop yield and crop economic value by visible injuries.

In many industrialized and urban centres of Asia, Latin-America and Africa, increases in gaseous air pollution has been experienced during recent decades, as a result of rapid economic growth, industrialization and urbanization associated with increased energy demands (Emberson, Ashmore et al. 2000). Predicted increases in global background ozone concentrations combined with increasing ozone precursor emissions imply that the future impacts of ozone to crops and forest in these areas may cause serious economic and social implications in regions of limited food supplies due to rapidly growing populations (Ashmore 2005).

According to Van Dingenen et al. (2009) the global economical loss due to ozone exposure to four major crops; wheat, rice, maize and soybean, was \$ 14-26 billion in the year 2000, 40% of the damage occurring in India and China. In the study, projected yield losses for 2030 are presented, optimistically assuming fully implemented current day air quality legislations. The results suggest a reduction of yield losses in most industrialized countries by 2030, and a slight improvement also in China. For the rest of Asia and in parts of Africa, current legislations are not sufficient to improve air quality and yield loss by 2030. (Van Dingenen, Dentener et al. 2009).

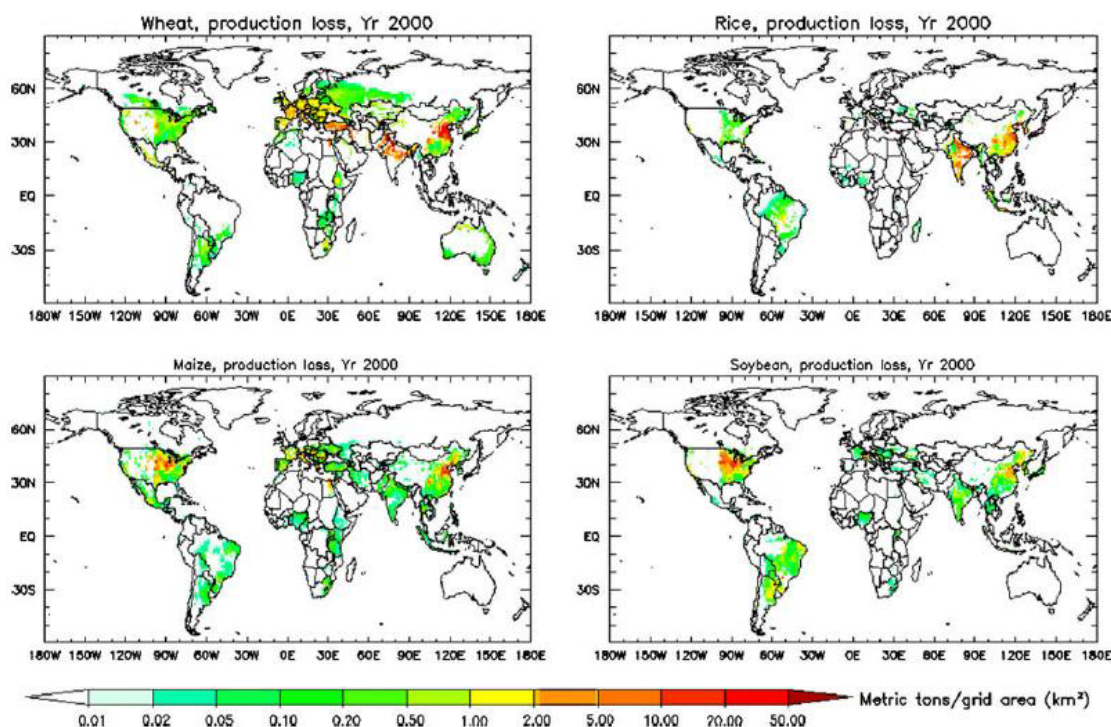


Figure 2-7: Geographical distribution of the estimated global present-day crop production loss in metric tons/km², derived from the gridded average relative yield loss (Van Dingenen, Dentener et al. 2009)

The global geographical distribution of present day crop production loss for the four species derived from average gridded relative yield loss (RYL) based on AOT40 and Mi indexes (see Chapter 2.2.3), accumulated over three months growing seasons is shown in Figure 2-7. Areas with high RYL, but low production intensity, like Africa, does not appear in this figure, but areas with low RYL, like Eastern USA, stand out due to high production intensities.

One main focus of this thesis is the Southern African region. On the African continent research on ozone induced damage to vegetation has in general been scarce. In South Africa research has shown that there are a number of areas where air pollution in general, and ozone induced damage to vegetation is perceived to be a problem (Emberson, Ashmore et al. 2000). As seen from Figure 2-7, the main reduction in crops in the southern part of Africa is in maize. According to Zuncel et al. (2006) monitoring of surface ozone across Southern Africa show that surface concentrations often exceed the threshold value used of 40 ppb, the highest values over Botswana and the Mpumalanga Highveld. As a result the Cross Border Air Pollution Project (CAPIA) was established, in order to assess the potential impact of vegetation in general, and maize specifically in five southern African countries (Zunckel, Koosailee et al. 2006). In the CAPIA project the AOT40 index was used in modeling to assess the potential risk to maize over the 2000-2001 growing season, and the results implied that the maize was indeed in risk of damage due to ozone exposure.

According to Sitch et al. (2007), another potentially important effect of increased ozone background levels in the coming years is that the limiting effect of ozone on plant photosynthetic rate can result in a decrease of the land-carbon sink, through decreased CO₂ uptake, leading to an accumulation of atmospheric CO₂. They suggest that this indirect increase in radiative forcing could exceed the direct radiative effect increased levels of tropospheric ozone has on global warming. The estimated indirect and direct effect on radiative forcing for two cases; low and high plant sensitivity is illustrated in Figure 2-8.

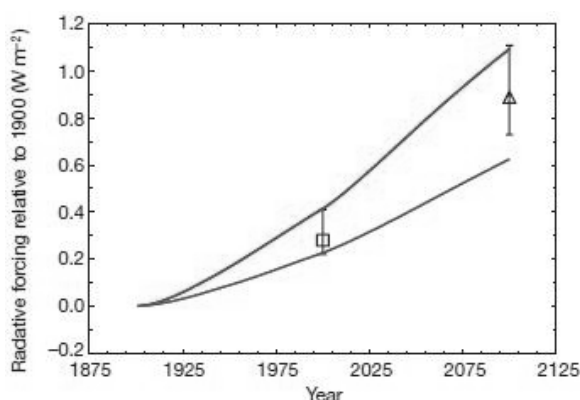


Figure 2-8: Indirect radiative forcing from O₃ increases alone compared to 1900. Derived from simulated changes in land-carbon storage. Upper line for high plant sensitivity to O₃, lower line for low sensitivity. Black bars and symbols are estimates of direct O₃ radiative forcing for 2000 (square) and 2100 (triangle). (Sitch, Cox et al. 2007)

In the following some general features of leaf anatomy are presented in Chapter 2.2.1, adverse effects of absorbed ozone on vegetation are discussed in Chapter 2.2.2 and techniques in assessing ozone risk to vegetation are presented in Chapter 2.2.3.

2.2.1 Plant physiology

All vegetation exposed to high ozone values is affected in different ways. In the following the general features of the leaf anatomy are presented, and some basic features of the processes determining ozone uptake in vegetation. The following is based primarily on Nobel (2005).

Leaf anatomy

The anatomical features and various cell types important in the photosynthesis and transpiration of a leaf are displayed in Figure 2-9.

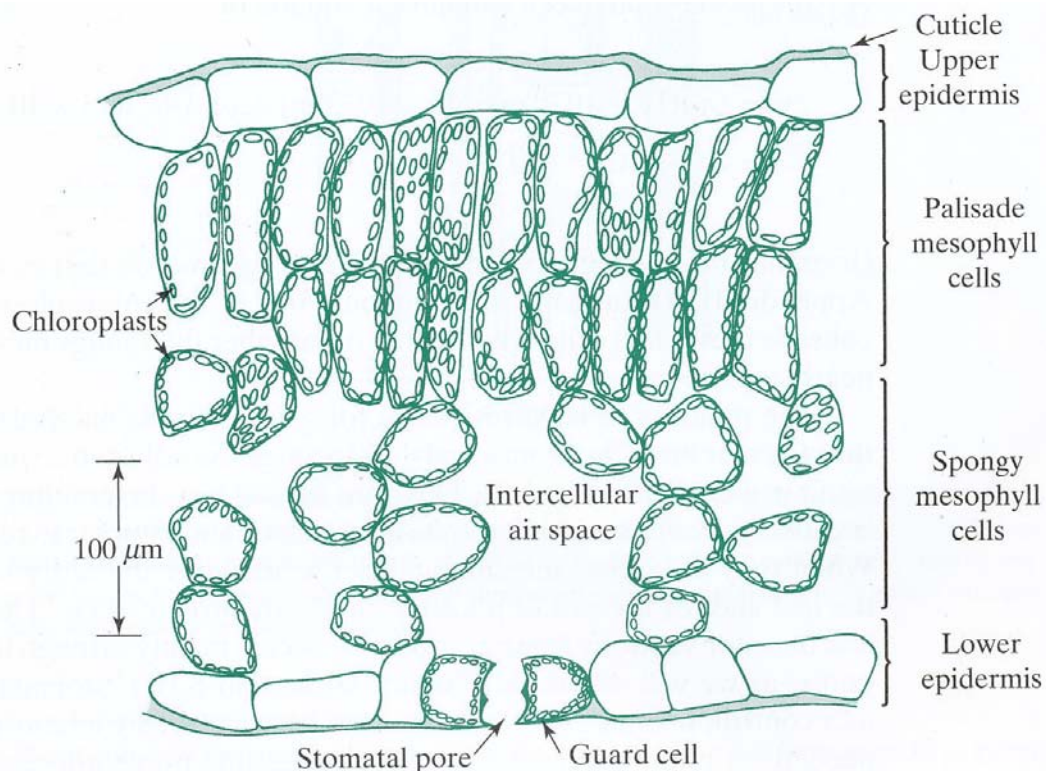


Figure 2-9: Schematic transverse section through a leaf, illustrating the arrangement of various cell types. (Nobel 2005)

Leaves are generally a few hundreds of micrometers thick. On the upper and lower sides of the leaf there is a single cell thick layer called the epidermis. This cell layer consists of usually colorless cells lacking chloroplasts (dependent on plant species), except for the guard cells appearing on each side of small pores on the leaf surface. The epidermal cells have a relatively thick waterproof layer called cuticle on the atmospheric side, contributing to prevent water loss from the leaf. In the middle of the leaf, between the epidermal layers, we find the chloroplast-containing mesophyll, consisting of “palisade” and “spongy” cells. The spongy cells are found in the middle part of the leaf, and the palisade cells in a layer just beneath the upper epidermis, often elongated at a right angle to the upper surface of the leaf. All of the mesophyll cells are loosely packed, and between them there are intercellular air spaces. Most of the surface area of the mesophyll cells is exposed to the intercellular air. The palisade mesocells often contain more chloroplasts than the spongy ones, and in many

leaves about 70% of the chloroplasts are found in the palisade cells, which are nearly twice as many as the spongy ones.

The Stomata

For gases and water vapor the easiest pathway to cross the epidermis is through the open pores on the leaf surface, adjusted by the two guard cells on each side. The pore together with the two guard cells is called a stoma (plural; stomata). There are big differences in number of stomatal pores per leaf area across plant species. Some plants have stomatal pores mostly on the lower epidermis (dicots); some have equal numbers on both sides of the leaf (monocots). In general, the area of the open pores occupy 0.2-2% of the leaf surface area.

The stomata control the entry of CO₂ into the leaf, and the exit of water vapor and photosynthetically produced O₂. The stomatal opening often depends on the CO₂ concentration in the guard cells. Upon illumination, the CO₂ concentration in the intercellular air space inside the leaf decreases due to photosynthesis. This leads to decrease of CO₂ in the guard cells, which triggers stomatal opening to allow entry of CO₂ into the leaf in order for photosynthesis to continue. It also allows for pollutants like SO₂ and ozone to enter the leaf through the open stomata. In the dark, transpiration causes CO₂ levels inside the leaf to rise, and stomata to close.

The stomata need to open in order for the plant to get CO₂ needed for the photosynthesis. In doing so, the plant will lose water vapor through the stomata, given a lower relative humidity (RH) outside the leaf. The parameter linking the flux of CO₂ and water vapor is called the water use efficiency (WUE), given as the ratio of CO₂ fixed per water vapor lost. In areas where water availability is not a limiting factor, the WUE will be low, and the water vapor flux high, and generally the photosynthetic rate is somewhat higher. In arid and dry areas plants with high WUE will dominate. The stomata will often completely or partially close during the day to regulate water loss, as the RH of the ambient air decreases (the water vapor deficit, VPD, increases), although at the expense of reduced photosynthesis. Some types of plants compensate for this by opening the stomata at night, taking up CO₂ without losing too much water.

If the plant is not exposed to any water stress, the stomatal opening in the light will generally increase with increasing temperature, up to the species- and location-specific optimal temperature for photophosphorylation⁴, often at about 30-40°C. In the dark the optimal temperature may be higher, and the stomatal opening can continue to increase at even higher temperatures.

⁴ Photophosphorylation is the production of the "molecular unit of currency" of intracellular energy transfer, Adenosine-5'-triphosphate (ATP), using the energy of sunlight.

Stomata can also respond directly to light, among other systems, through processes involving the absorption of photosynthetic photon flux (PPF) by chloroplasts in the guard cells.

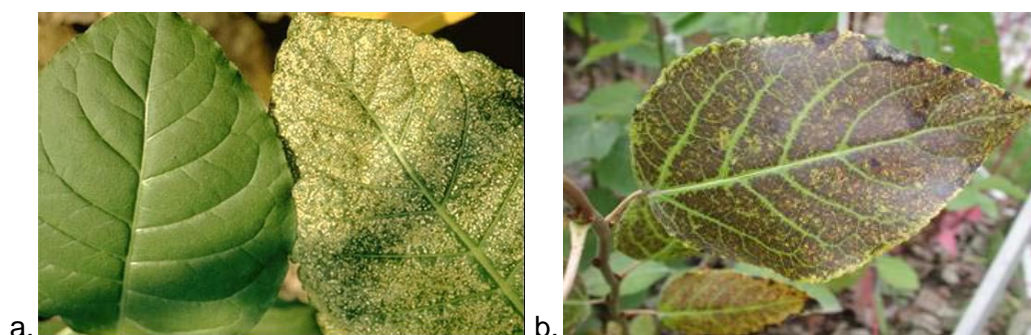
Thus, the water status, temperature and PPF can all affect the stomatal conductance, as they all influence the photosynthetic rate of the leaf. However, water vapor and gaseous components can also cross the epidermis by diffusing through the cuticular layer of the leaf surface, following a parallel pathway to the stomata into the leaf. The rate of such cuticular transfer is usually much lower than through the open stomata, but can exceed values of conductance through the almost closed stomata. In the case of old or damaged leaves, the rate of cuticular transfer can increase as the cuticular layer may be cracked or damaged.

2.2.2 Adverse effects

There are two main effects of ozone in exposed vegetation; in cases of high uptake, ozone may overwhelm the plant's capability to detoxify and repair, and cause direct damage. In cases of lower uptake, ozone may induce a range of defense reactions requiring energy which might otherwise be used in carbon assimilation, resulting in reduction in photosynthetic rate, decreased tree growth and biomass production. (Fowler et al. 2008)

The adverse effects of ozone on vegetation range from cellular and subcellular processes, to effects on leaf and plant level, which can lead to changes to the whole plant community. In the following the adverse effects on the different levels are presented.

As ozone molecules enter the leaf through the stomata it reaches the site of the mesophyll cells. Upon collision with the mesocells ozone will immediately decompose into the water film covering the substomatal cavity cells and generate reactive oxidant species (ROS). The ROS are severely toxic to the plant as they are able to initiate a cascade of biochemical reactions resulting in a wide range of adverse effects to the plant. These effects may lead to inhibition of metabolic pathways, enzymatic activities, rubisco inhibition, and disruption of the chlorophylls and alteration of the photosystems (Gerosa et al. 2010). Plants have developed various mechanisms to reduce the oxidative stress, to minimize the overall damage (Nali, Pucciariello et al. 2005). Further description of these complicated, and in some cases not yet fully understood biochemical processes, is beyond the scope of this thesis, and next is the leaf level adverse effects.



Picture 2-1: a) Healthy (left) and damaged (right) leaf of bean. Macroscopial lesions known as stipples are a sign of ozone induced damage to the plant. b) Early senescence. (Pictures from Gerosa et al. (2010))

On leaf level visible injuries as seen in Picture 2-1 are the most apparent sign of ozone damage. Ozone induces chlorosis⁵ and premature death of leaves and tissue, which can be seen on the leaf. Alterations in color, like stippling and bronzing (Picture 2-1a,b) can occur, along with deformations of the leaves by curling. Early leaf aging (after maturity) and abscission⁶ is also common signs of ozone damage (Gerosa et al. 2010). Visible injuries due to ozone are widespread, and have been recorded in over 30 crop and 80 (semi-) natural species across Europe alone (Hayes, Mills et al. 2007). It is commonly reported in North America and have also been reported in Egypt, India, South America and Taiwan (Ashmore 2005). For many crop species with a market value dependent on their visible appearance, such injuries cause an immediate loss of market value and severe economical implications for local producers. The foliar chemistry and surface characteristics caused by ozone may also have various secondary effects, such as influence on the rate of fungal attacks, and impact of insect pests (Ashmore 2005).

At plant level, increased crown transparency and alteration in branch structure can occur, and alterations in the plant flowering. The activation of repairing processes can lead to reduced photosynthesis and increased respiration, leading to reduction in biomass production and grain yield, and lower reproductive efficiency. It can also lead to reduced carbon allocation to the roots leading to reduced root development which in turn can cause higher vulnerability to other stress factors such as water stress. This can also cause a negative effect on the vegetative restart processes of the next season.

The long-term effects of ozone exposure to plant communities remain uncertain, however the above effects on plants result in a lower competitiveness, which can result in a possible alteration of the ecosystem composition. Natural selection may cause ozone sensitive species to decline as more ozone tolerant genotypes increase. In some cases this can lead to a reduction of biodiversity resulting in a decrease in the resistance to external perturbations. Differences in sensitivity between populations from different locations are also well known (Ashmore 2005).

In addition to yield reduction and visible injuries, the crop nutritional quality can be reduced as a result of ozone exposure. Although not well understood, several examples of poor crop nutritional quality, lowering the value of crops have been reported. Juice quality of fruits and oil content of seeds are examples mentioned in Ashmore (2005). Also examples of increased nutritional quality of some crops in cases of ozone exposure are known.

2.2.3 Risk assessment

There are various metrics in use in order to assess the risk of ozone- induced damage to vegetation. Some are concentration-based, like the seasonal 7hour or 12 hour mean ozone concentration during sunlit hours (M7 and M12, respectively), and seasonal cumulative

⁵ *Chlorosis* is a condition in which leaves produce insufficient chlorophyll.

⁶ *Abscission* is the process where a plant drops one or more of its parts, such as a leaf, fruit, flower or seed.

exposure indexes over some threshold (60 or 40 ppb usually) such as SUM06 and AOTX. In the following two main indexes used in Europe, the accumulated concentration based AOTX index, and the flux- based AFstY are presented, along with their advantages and disadvantages. Both of these indices include a threshold value, below which the plants capability to detoxify the incoming ozone is assumed to protect it from direct damage. However, this threshold value will realistically vary between species, meteorological conditions and genotypes.

Concentration- based approaches to assess the impact of ozone on vegetation are the most traditional ones. They are based on the assumption that higher ozone concentrations in the ambient air above the canopy leads to more damage to the vegetation. The most widely used concentration- based metric used in Europe is the AOTX (Accumulated exposure Over a Threshold of X ppb), which according to Mills (2004) can be defined as

$$AOTX = \int \max (C - X, 0) dt$$

(2-44)

where C is the ozone concentration at canopy height, and X is the threshold value in ppb, above which the plants are assumed to be damaged. The integral is to be evaluated over time, in principle over the growing season. Only daylight hours should be accumulated, and for this various implementations are used.

The UNECE concentration-based threshold X for crops and forest is 40 ppb. The seasonal accumulated exposure above 40 ppb (AOT40) is normally expressed as a cumulative exposure given in (ppm h) or (ppb h). The UNECE accumulate only hours of clear-sky global radiation exceeding 50W m⁻², usually over a three month growing season, depending on the species. The EU uses a somewhat easier approach, accumulating over all hours between 8 am to 8 pm local time.

Current UNECE critical levels and legislations are based on AOT40-effect relationships, which are numerous and have been developed from experiments in controlled environments. Mills et al. (2007) collected data from over 700 published papers to establish AOT40 –yield response relationships for 19 crops, divided in to three sensitivity categories (sensitive crops, moderately sensitive, and ozone resistant). The averaged response relationship for each of the categories is plotted in Figure 2-10.

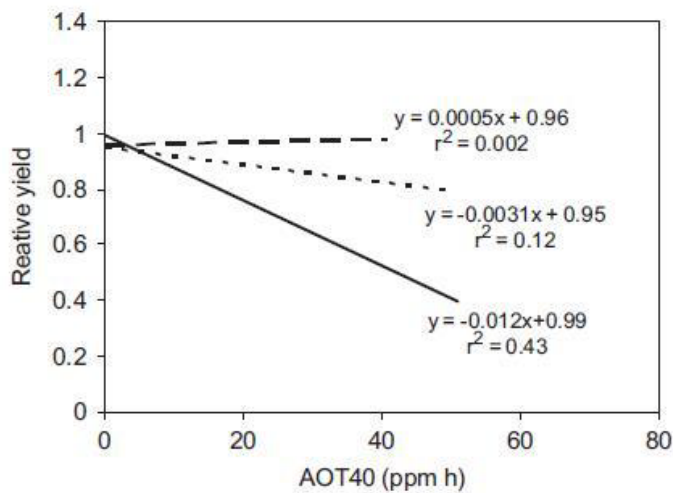


Figure 2-10: Response functions combined into three sensitivity categories. Solid line represents sensitive crops (wheat, water melon, pulses, cotton, turnip, tomato, onion, soybean and lettuce), dotted line moderately sensitive (sugar beet, potato, oilseed rape, tobacco, rice, maize, grape and broccoli), and stippled line resistant crops (barley and fruit represented by plum and strawberry). (Mills, Buse et al. 2007)

The advantage of the concentration based approach is that the only parameter needed to determine risk is the ozone concentration. The disadvantage is that the ozone concentration used should be as close to the canopy top as possible. In measurements usually the height of 3 meters above ground is used. Due to the large vertical gradients in concentrations near ground due to turbulence, modelled ozone concentrations at plant canopy are also associated with uncertainties.

As high ambient air ozone concentration does not imply actual uptake of ozone in the vegetation, it has in recent years become evident that it is not the most suitable index for determining the risk to plants. In situations where high solar intensity, temperatures and drought coincides with high ozone concentrations, the AOTX index would give high risk values. As explained in Chapter 2.2.1, the stomata might in such conditions close to conserve water, and in doing so, prevent ozone from entering the plant. This would indeed lower the risk of ozone-induced damage. At the same time ambient ozone concentrations well below 40 ppb have been estimated to induce adverse effects on some sensitive species. Significant fluxes of ozone into wheat was modelled by (Danielsson, Karlsson et al. 2003) at concentrations of 24ppb, much lower than 40 ppb. This implies that the current mean global background concentrations are well within the range at which ozone-induced damage to sensitive vegetation can occur (Ashmore 2005). This aspect has in recent years led to requirements that risk assessment should take into account the fact the effect on the leaf is more closely related to the actual flux into the leaf, than the ozone concentration in the surrounding air. This has led to the development of the flux based approach, which relates risk to the absorbed stomatal ozone dose, by utilizing stomatal conductance parameterizations. AFstY (Accumulated stomatal Flux over thresholds of $Y \text{ nmol m}^{-2}\text{s}^{-1}$) is according to Mills (2004) defined as

$$AFstY = \int \max (Fst - Y, 0) dt$$

(2-45)

where Fst is the stomatal flux and Y is the threshold below which no plant damage is expected to occur, given in $\text{nmol m}^{-2}\text{s}^{-1}$ (Mills 2004). The threshold value is usually

empirically determined from open top- chamber experiments (see next page). The flux-based approach is thought to be built on a more correct biological basis, as it accounts for the fact that only the ozone that actually enters the plant has the potential to induce damage, and the various meteorological and environmental factors determining the stomatal flux.

However, the measurements of ozone fluxes require advanced instruments of high temporal resolution, and advanced techniques to measure perturbations in the vertical wind component, w' . Application of this approach requires the development of flux-response relationships, determining the actual damage done per absorbed dose. This has at present only been developed for a few species. The flux based approach nor the exposure-based index, take into account for the variation in the plants detoxification potential, which may, as the flux, vary with environmental conditions, plant species and age.

According to Simpson et al. (2007), the spatial distribution of modelled risk to crops and forests in Europe, show big differences depending on the metric used. Figure 2-11 shows the modelled risk of ozone induced damage to crops (represented by wheat) across Europe for the year 2000 using the EMEP MSC-W photo-oxidant model. Using the AOT40 metrics derived from 3 m and canopy-top ozone values, the distribution show a stronger north-south gradient in distribution, while applying the flux based index with threshold value of $6 \text{ nmol O}_3 \text{ m}^{-2} \text{ s}^{-1}$ per projected leaf area (PLA), gives a more evenly distributed risk prediction.

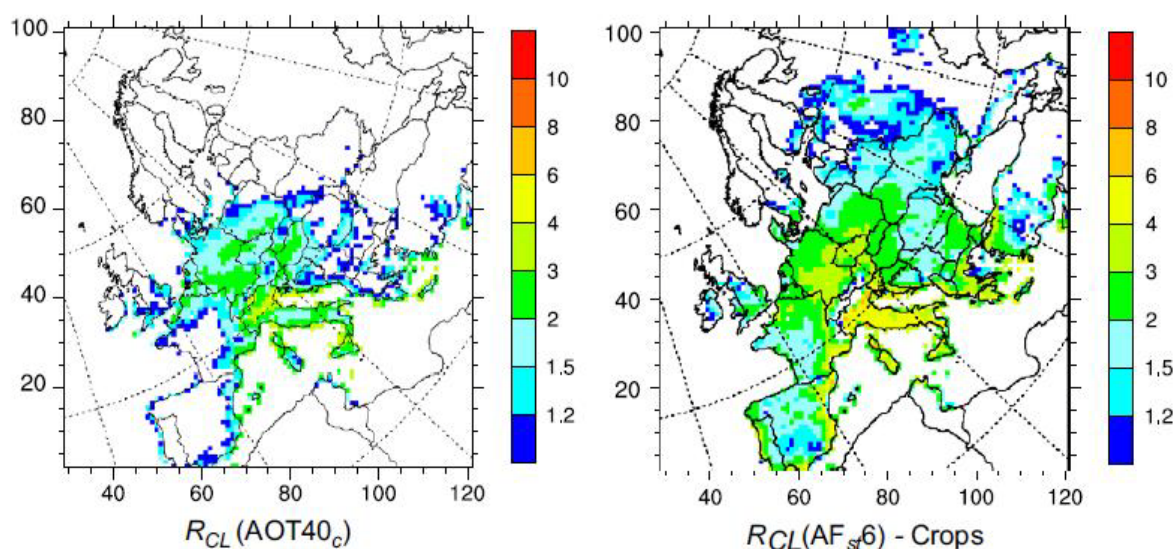


Figure 2-11: Modelled R_{CL} values for crops across Europe for the year 2000. R_{CL} (the relative exceedance above the critical value (CL), 3000ppb h for AOT40 metrics, 1 mmol m^{-2} for Afst6) represents the ratio of modelled flux or exposure to the relevant critical level for AOT40 metrics (left), and Afst 6 metrics (right), and are only displayed for $R_{CL} > 1.0$. (From Simpson, Ashmore et al. 2007).

Measuring methods

There are various ways of measuring ozone effect on leaves and plants. Investigations have been carried out in open fields, with plants exposed to the ambient air ozone concentration, and naturally occurring climatic conditions (e.g. Gerosa, Vitale et al. 2005; Gerosa, Finco et al. 2009b). For experiments in controlled environments one can use open top chambers, in

which one can regulate the ozone exposure (with or without charcoal filtered air), comparing the plant development in an “ozone-free” atmosphere to the response of plants in various controlled ozone concentrations. It is also possible to regulate environmental factors such as the water status by irrigation (e.g. Gerosa, Marzuoli et al. 2008; Gerosa, Marzuoli et al. 2009c).

Stomatal conductance algorithms

The flux based approach as described above, is based on the use of a stomatal conductance algorithm. In order to estimate the damaging dose of ozone to the plant, one needs to first estimate the stomatal flux, given as various functions of the ambient ozone concentration, the climatic conditions and species-specific values. In the following the two methods utilized to parameterize dose in this thesis are presented.

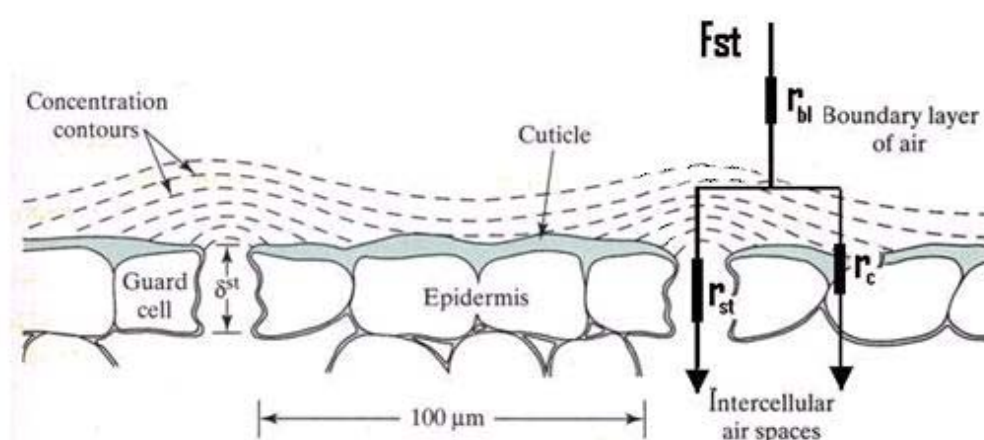


Figure 2-12: The stomatal conductance algorithm estimates the flux of ozone through the stoma by utilizing the resistance analogy. (Modified from Nobel (2005))

The stomatal flux of ozone into a plant leaf is given as the conductance times the ozone concentration of the air surrounding the plant canopy. It can be expressed

$$F_{st} = g \times C$$

(2-46)

where g is the conductance ($g = 1/r$ where r is the resistance), and C is the ambient concentration. The conductance is found using the resistance analogy. This analogy reflects Ohm's law⁷ for electrical currents in a circuit. The resistances in the analogy are used to

⁷ **Ohm's law** states that the current(I) through a conductor between two points is directly proportional to the potential difference or voltage(U) across the two points, and inversely proportional to the resistance(R) between them: $U=RI$

account for the biological, meteorological and chemical processes controlling the flux of each gas, illustrated in Figure 2-12. The flux density of the gas molecules and the difference in gas concentration across the canopy reflect the current and the voltage, respectively. As seen in Figure 2-12, the resistances in the analogy can be placed in both parallel and series, to best account for the physical processes they are representing.

In this thesis the dry deposition scheme of the WRF-Chem weather forecasting model is used to predict the stomatal flux of ozone. The scheme is based on the article of Wesely (1989). The aim of the scheme is to calculate the dry deposition rate of ozone to the surface, and in doing so as accurately as possible, it takes into account the stomatal influence in the deposition. This allows for the application of this thesis, namely using it to estimate the flux of ozone into the surface vegetation. Further description of the dry deposition routine is found in Chapter 3.4.

The Jarvis approach

The multiplicative conductance model based on the Jarvis algorithm for stomatal conductance (Jarvis 1976), has been used in a number of studies which have estimated stomatal flux to be related to risk to vegetation (e.g. Emberson, Ashmore et al. 2000; Danielsson, Karlsson et al. 2003; Pleijel, Danielsson et al. 2007; Gerosa, Marzuoli et al. 2009d). The DO₃SE (Deposition of Ozone and Stomatal Exchange) model currently used by the European Monitoring and Evaluation Program (EMEP) is also based on this algorithm, and further details of that can be found in Mills (2004).

There are many variations in applying the algorithm. According to Mills(2004), the algorithm's expression for stomatal conductance, g_{sto} can be written as

$$g_{sto} = g_{max}[\min(f_{phen}, f_{O_3})]f_{light} \times \max\{f_{min}, (f_{temp}f_{VPD}f_{swp})\},$$

where g_{sto} is given in nmol O₃ m⁻² PLA⁻¹, and g_{max} is the species-specific maximum stomatal conductance given in the same units. As g_{max} rarely occurs in the field due to environmental and phenological limitations, it is derived from experiments in controlled environments like open top chambers, and from field studies. The parameters of f_{phen} , f_{O_3} , f_{light} , f_{temp} , f_{swp} and f_{VPD} are all values between 0 and 1, and allow for modification of the maximum possible conductance, dependent on the phenology, and the various environmental factors of available sunlight, temperature and the water status, given as the vapor pressure deficit of the ambient air and the soil water potential. The most limiting factor of the f_{O_3} and f_{phen} is used. The ozone-function only comes into effect when early senescence from ozone damage is more influential than normal senescence. In addition a $\sum VPD$ function is also included to account for the water vapor transpiring which often occur during the afternoon, which may lead to a lowering of the stomatal conductance due to low water potential in the leaf.

The dependency of the stomatal conductance on the different environmental variables is found using the boundary line technique. A line representing the maximum influence of the specific variable on the conductance is fitted and represent the respected f -functions.

The Jarvis approach has been used by Pleijel et al. (2007) (P2007 hereafter) in developing flux- based dose-response relationships for wheat and potato in Europe. Following is a short description of each f -function as suggested for wheat and potato in P2007.

The phenology function can either be based on a fixed number of days, e.g. from the start of the growing period (A_{start}) to the end (A_{end}), or on effective temperature sum (tt) accumulation. The latter means accumulating the days with temperature above a base temperature of 0°C over the growing season, and is accepted to more accurately describe temperature influence on plant development. The growing season is in this case expressed as the number of f_c temperature days before anthesis and tuber initiation to f_d temperature days after, in wheat and potato. With the parameters (f_a) and (f_b) representing the limitation of stomatal conductance at the start and the end of the accumulation period respectively, the phenology functions for before, and after anthesis are described with the following expressions

$$f_{phen} = 1 - \left(\frac{f_a - 1}{f_c} \right) tt$$

(2-47)

$$f_{phen} = 1 - \left(\frac{1 - f_b}{f_d} \right) tt$$

(2-48)

It is assumed that crop leaves attain their maximum stomatal conductance (g_{max}) under mid anthesis, and declines along with senescence. The phenology relationship for wheat used in P2007 is shown in Figure 2-13.

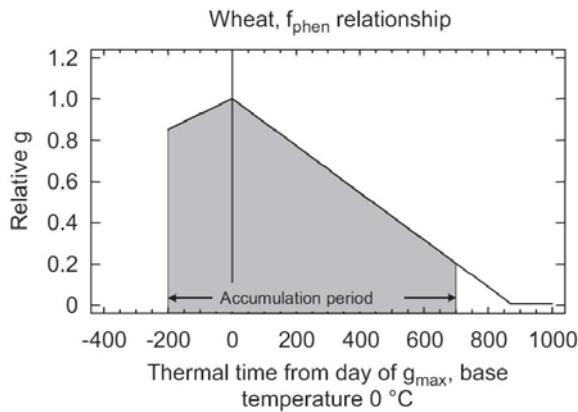


Figure 2-13: The parameterization used for the phenology function (f_{phen}) for wheat. (From P2007)

The function used to describe the dependency of the conductance on light is shown in Figure 2-14 a) and is given as

$$f_{light} = 1 - e^{-L PFD}$$

(2-49)

Where L is a species specific constant, and PFD is the photosynthetic photon flux density given in ($\mu\text{mol m}^{-2}\text{s}^{-1}$).

The temperature parameterization shown in Figure 2-14b), takes into account the species specific variation of the temperature dependency around the optimal temperature for conductance.

$$f_{temp} = \left[\frac{(T - T_{min})(T_{max} - T)}{(T_{opt} - T_{min})(T_{max} - T_{opt})} \right]^{bt}, \quad T_{min} < T < T_{max}$$

(2-50)

Where T is the surface air temperature, and T_{max} to T_{min} is the range between which $f_{temp} > f_{min}$. T_{opt} is the optimal temperature and bt is given as

$$bt = \frac{T_{max} - T_{opt}}{T_{opt} - T_{min}}$$

(2-51)

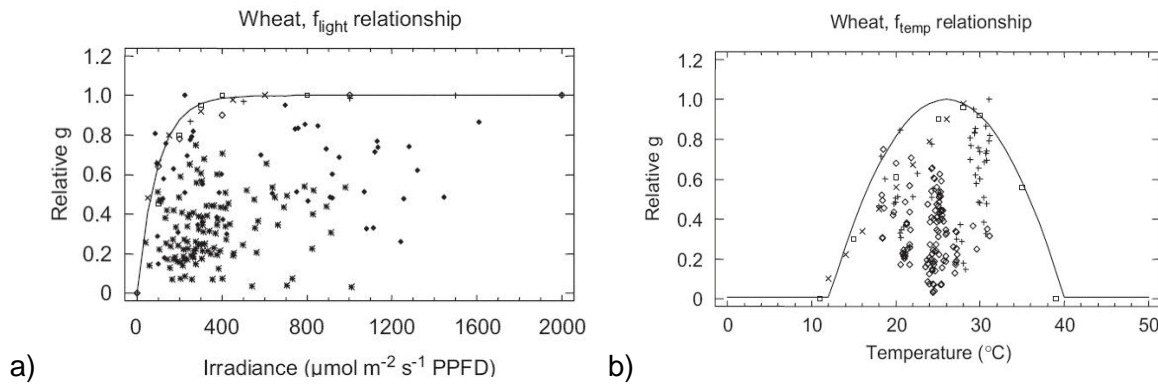


Figure 2-14: a) The function of f_{light} , representing the short-term response of light on the stomatal conductance. b) The function of f_{temp} , representing the short-term response of temperature on the stomatal conductance. The boundary line is used to define the maximal influence on the conductance. All the data points used are from different investigations, for references see P2007. (From P2007)

At high VPD values of the ambient air surrounding the canopy the stomata will almost immediately close in order to preserve water. This effect is accounted for by the f_{VPD} – function seen in Figure 2-15a). The expression for the VPD function can be written;

$$f_{VPD} = \min \left\{ 1, \max \left[f_{min}, \frac{(1 - f_{min})(VPD_{min} - VPD)}{VPD_{min} - VPD_{max}} + f_{min} \right] \right\}$$

(2-52)

The VPD may also have a different effect on the stomata opening, not accounted for in the f_{VPD} -function. In the late afternoon the air temperature often decreases, and some times, a decrease in the VPD will follow (given that the RH stays more or less the same). This will according to the f_{VPD} function give an increase in the stomatal opening, which in many cases is small in mid-day high VPD conditions. Non the less, the plant does often lose more water through transpiration than what is replaced from the roots during the day, which reduces the chance of stomata opening again in the afternoon, as the waters water potential is already

reduced. This effect is accounted for by the second VPD function, which accumulates the high-VPD hours during the day. If the VPD sum exceeds the critical VPD limit, the re-opening of the stomata in the afternoon is considered unlikely.

$$\text{If } \sum VPD \geq \sum VPD_{crit} \text{ then}$$

$$g_{st, hour\ n+1} \leq g_{st, hour\ n}$$

(2-53)

This means that if VPD exceeds VPD_{crit} , and the stomatal conductance of the present hour, $g_{st, hour\ n+1}$, is higher than the preceding hour, $g_{st, hour\ n}$, then the value for the stomatal conductance is replaced with that of the preceding hour, and is thereby always less or equal to the preceding hour given that the VPD value is over the species specific critical value.

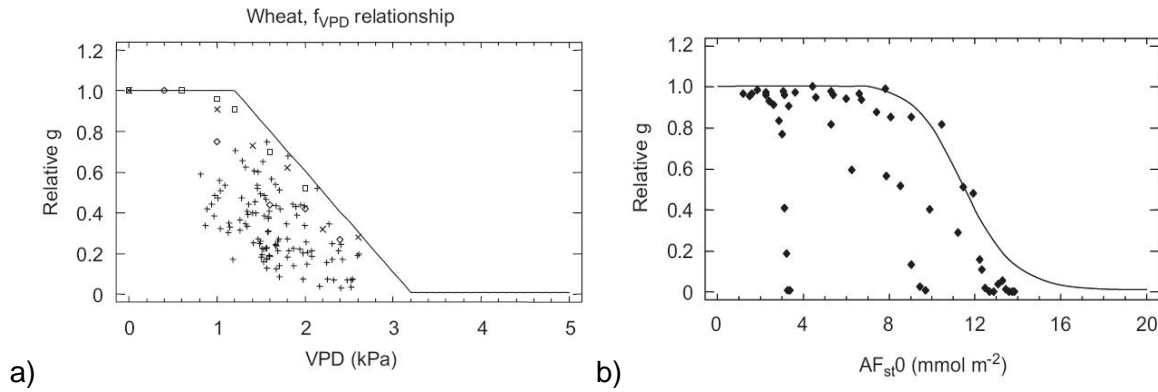


Figure 2-15: a) The VPD-function representing the short-term response of ambient air VPD on the stomatal conductance. The boundary line is used to define the maximal influence on the conductance. All the data points used are from different investigations, for references see P2007. b) The ozone function f_{O_3} , describing the long-term effect of ozone induced leaf senescence for wheat. $AF_{st\ 0}$ is the accumulated flux with no flux threshold. (From P2007)

The last of the functions is the ozone function, which accounts for the ozone concentrations influence on the stomatal conductance through early senescence (Figure 2-15b). The ozone function only comes into effect when high ozone exposure cause ozone induced senescence to dominate the natural senescence accounted for by the phenology function. The ozone function for spring wheat used in P2007 is given as

$$f_{O_3} = \left(1 + \left(\frac{AF_{st\ 0}}{11.5} \right)^{10} \right)^{-1}$$

(2-54)

And for potato

$$f_{O_3} = \left(1 + \left(\frac{AOT\ 0}{40} \right)^5 \right)^{-1}$$

(2-55)

AFst 0 in the first function is the accumulated flux from A_{start} , and AOT 0 is simply the accumulated sum of the hourly mean concentration from A_{start} in $\text{nmol m}^{-2} \text{s}^{-1}$. These functions are based on the assumption that the ozone induced decline in stomatal conductance after anthesis, is proportional to early senescence due to ozone.

3 Methods and Data

3.1 The Weather Research and Forecasting model (WRF)

The Weather Research and Forecasting model (WRF) is a mesoscale weather prediction system. It is a model with a wide variety of applications, across scales ranging from large-eddy to global simulations. Applications include real-time numerical weather prediction, data assimilation development and studies, parameterized-physics research, regional climate simulations, air quality modeling, atmosphere-ocean coupling, and idealized simulations (Wang, Bruyère et al. 2010).

WRF was developed as a collaboration, principally among the National Center for Atmospheric Research (NCAR), the National Oceanic and Atmospheric Administration (the National Centers for Environmental Prediction (NCEP), the Forecast Systems Laboratory (FSL), the Air Force Weather Agency (AFWA), the Naval Research Laboratory, the University of Oklahoma, and the Federal Aviation Administration (FAA).

The principal components of the WRF system are the dynamics solvers, physics packages that interface with the solvers, programs for initialization, the WRF Pre-Processing System (WPS), WRF-Var, and WRF-Chem. There are two dynamics solvers: the Advanced Research WRF (ARW) solver (originally referred to as the Eulerian mass solver) developed primarily at NCAR, and the NMM (Nonhydrostatic Mesoscale Model) solver developed at NCEP. The main components of the WRF modeling system is shown in Figure 3-1.

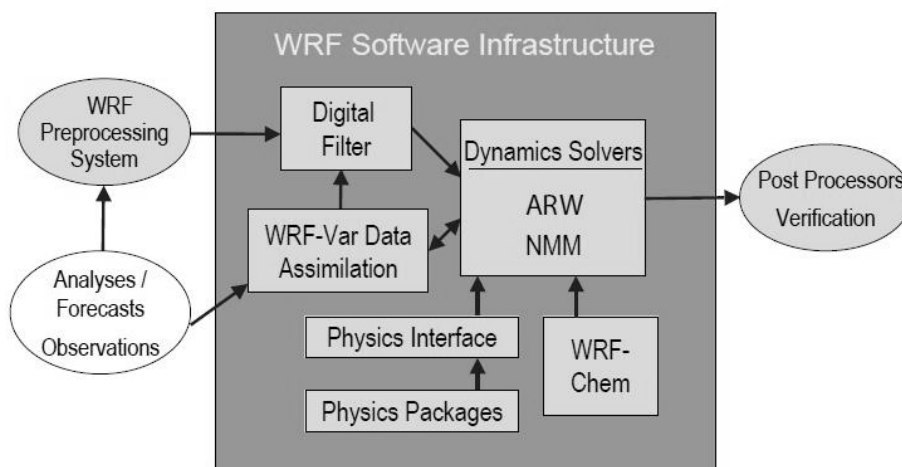


Figure 3-1: The WRF model system components. (From Skamarock, Klemp et al. 2008)

In this thesis Version 3 of the WRF modeling system is used, a subset of the WRF modeling system including the Advanced Research WRF dynamical solver (ARW) together with physics schemes and dynamics/numerical options compatible with the solver, WRF-Chem and WRF-Var.

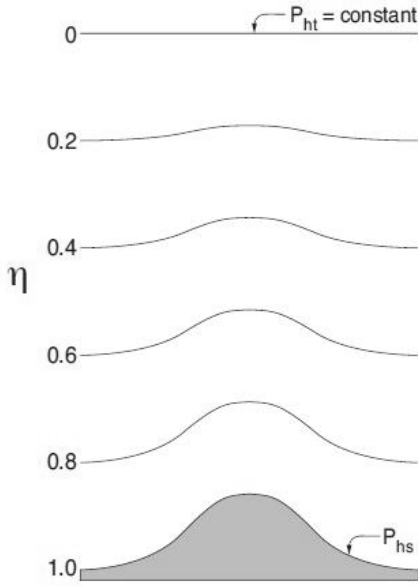


Figure 3-2: The terrain-following hydrostatic-pressure vertical coordinate η , and P_{ht} is the pressure at the top constant pressure surface. (From Skamarock, Klemp et al. 2008)

The ARW is an Eulerian and nonhydrostatic fully compressible model, with a hydrostatic option. It is conservative for scalar variables. It uses terrain following, dry hydrostatic pressure vertical coordinate (also called a mass vertical coordinate) with permitted vertical stretching. The top of the model is a constant pressure surface (see Figure 3-2) and the vertical coordinate varies between the value 1 at the surface to 0 at the top. The vertical coordinate is defined as

$$\eta = \frac{p_h - p_{ht}}{p_{hs} - p_{ht}} \quad (3-1)$$

where p_h is the hydrostatic component of the pressure, and p_{ht} and p_{hs} are the values for the top and surface boundaries, respectively (Skamarock, Klemp et al. 2008).

The ARW uses a time-split integration scheme. Slow and low frequency modes are integrated using a third-order Runge-Kutta scheme, while higher frequency acoustic modes are integrated using smaller timesteps for numerical

stability. The large timestep (in seconds) should be chosen to be less than six times the grid cell distance (in kilometers) to avoid numerical instability (Further description of the time-integration scheme in e.g. Wicker and Skamarock 2002).

For the spatial discretisation ARW uses a staggered Arakawa C grid, as seen in Figure 3-3. Normal velocities are staggered half a grid cell from the thermo-dynamic variables. These variables are defined at the points indicated by the θ , called mass-points. The diagnostic variables (pressure p and the inverse density α) and the moisture variables are defined at the mass points. The vertical mass coordinate η is defined at the (i, j) mass points, and the geopotential is defined at the w -points seen in the vertical grid of Figure 3-3.

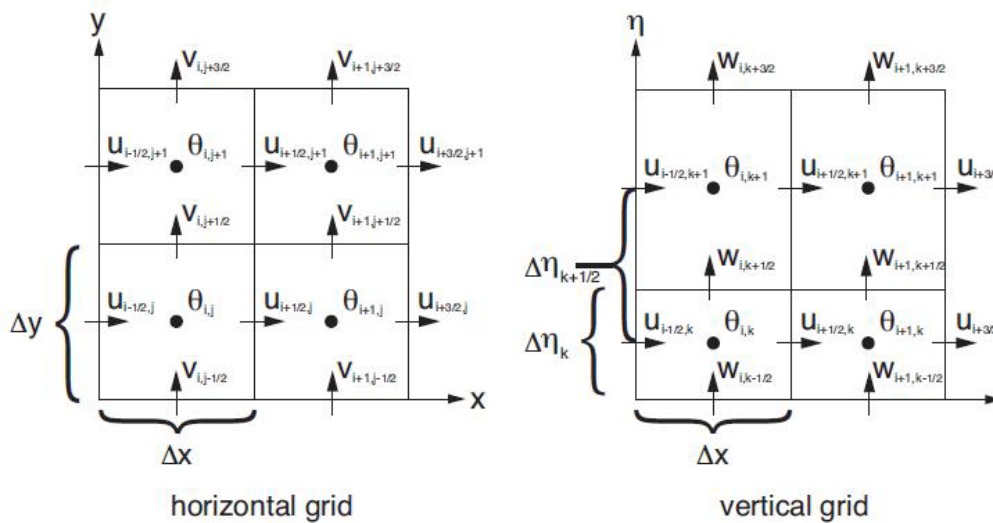


Figure 3-3: Horizontal and vertical grids used in the ARW. (From Skamarock, Klemp et al. 2008)

The ARW also support one- and two way nesting in the horizontal grid to produce a finer resolution domain with boundary conditions provided from the parent domain. In the case of nesting, the coarser grid is integrated first, in order to provide boundary conditions for the finer one. In the case of two way nesting, the result of the finer grid integration in turn replaces the results of the first integration, for points within the finer grid domain. The ARW also support moving nested grids (Skamarock, Klemp et al. 2008).

3.2 WRF-Chem

WRF-Chem is WRF coupled with chemistry, and the chemistry module is completely embedded in WRF. Uses include forecasting chemical-weather, testing air pollution abatement strategies and planning and forecasting for field campaigns. It can also be used in analyzing measurements from field campaigns and analyzing the assimilation of satellite and in-situ chemical measurements.

The developing of WRF-Chem was a collaboration between different institutions, including The Department of Commerce/National Oceanic and Atmospheric Administration (NOAA), The Cooperative Institute for Research in Environmental Sciences (CIRES), The University Corporation for Atmospheric Research (UCAR), the National Centre for Atmospheric Research (NCAR), The Max Plank Institute, The University of Chile (Peckham, Georg A. Grell et al. 2009).

The chemistry package presently consists of the following main components, in most cases with multiple options; dry deposition (see Chapter 3.4 below), biogenic emissions, anthropogenic emissions, gas-phase chemical mechanisms, photolysis schemes, and aerosol schemes with direct and indirect effect through interaction with atmospheric radiation, photolysis and microphysics, together with options for tracer and transport separated from the chemistry, and a plumerise model. A summary of the choices made and the general setup for the simulations of this thesis are presented in Chapter 3.3.2.

The chemistry component of the model uses the same grid, timestep, and the same physics schemes for subgrid-scale transport, as the meteorological part of the model, making the chemistry fully coupled and “online” with the dynamical part of the model. For our purpose the WRF-Chem package is used to estimate the ozone distribution and deposition. The mass balance equation for the change of the abundance of a species μ can according to Jacob (1999) be written as

$$\frac{d\mu}{dt} = P - L\mu + E - \mu D + T$$

(3-2)

where P and L is the in situ chemical production and loss of the specie, respectively, which is handled by the models chemical mechanism. E is emission, which in the case of ozone is represented indirectly through the emission of its precursor gases. D is the destruction by deposition, for ozone by dry deposition, handled by the dry deposition scheme of the chemical package, which is described in more detail in Chapter 3.4. T is the the transport, and all transport of chemical components is calculated by the meteorological part of the model (which is mass and scalar preserving). According to Grell et al. (2005) the mass

conservation equation and the scalar conservation equation calculated in the ARW can be written

$$\rho_t + \nabla \cdot (\nabla \rho) = 0 \quad (3-3)$$

$$(\rho\mu)_t + \nabla \cdot (\nabla \rho\mu) = 0 \quad (3-4)$$

where ρ_t is the column mass of air at time t , ∇ is the velocity, and μ is a scalar mixing ratio. The model exactly (to machine round off) preserves mass and scalar mass as these equations are discretized in a finite volume formulation.

3.3 Simulations and model setup

3.3.1 Simulations

The WRF-Chem model was run for three periods; two shorter test periods for comparing data with measurements made by Gerosa et al. (2009) in Castelporziano outside Rome, Italy, and one long simulation over an entire maize growing season in the southern part of Africa, in order to estimate the accumulated flux of ozone to vegetation over that time. The domains and resolutions are presented in Table 3-1 below.

Table 3-1: Resolution, dimensions and timestep of each of the simulations.

Domain	Horizontal resolution	Dimensions	Vertical layers*	Δt
Italy	27km x 27 km	100 x 100	27	120s
Nested; Italy 2	9km x 9km	100 x 94	27	40s
Southern Africa	27km x 27km	100 x 100	27	120s

*The 27 vertical layers stretch from the ground up to 50hPa, normally just above the tropopause.

Italy

The model was run for two separate periods during the 2007 in order to compare results with measurements made by Gerosa et al. (2009) in Castelporziano, outside Rome, Italy, in order to assess the performance of the model. The two periods of May 20-26 and June 22-28 were selected by the availability and quality of measured data for comparison. The length of six days in each period was chosen as a compromise between being long enough to give enough data for comparison with measurements, and short enough to avoid having to restart the model to keep the meteorological part from deviating too much from the initial conditions, and also because of high demand on computing time.

As initial conditions for the meteorology, data from the ECMWF⁸ model, interpolated to a resolution of $0.25^\circ \times 0.25^\circ$ are used. The data contains analyzed fields every six hours, and also serve as boundary conditions for the outer domain.

The simulations were run using a one-way nested domain setup, displayed in Figure 3-4. The big domain covers large parts of Europe and the Mediterranean, and the smaller zooms in on the middle and northern part of Italy. The site of measurements for comparison is covered by the inner domain.

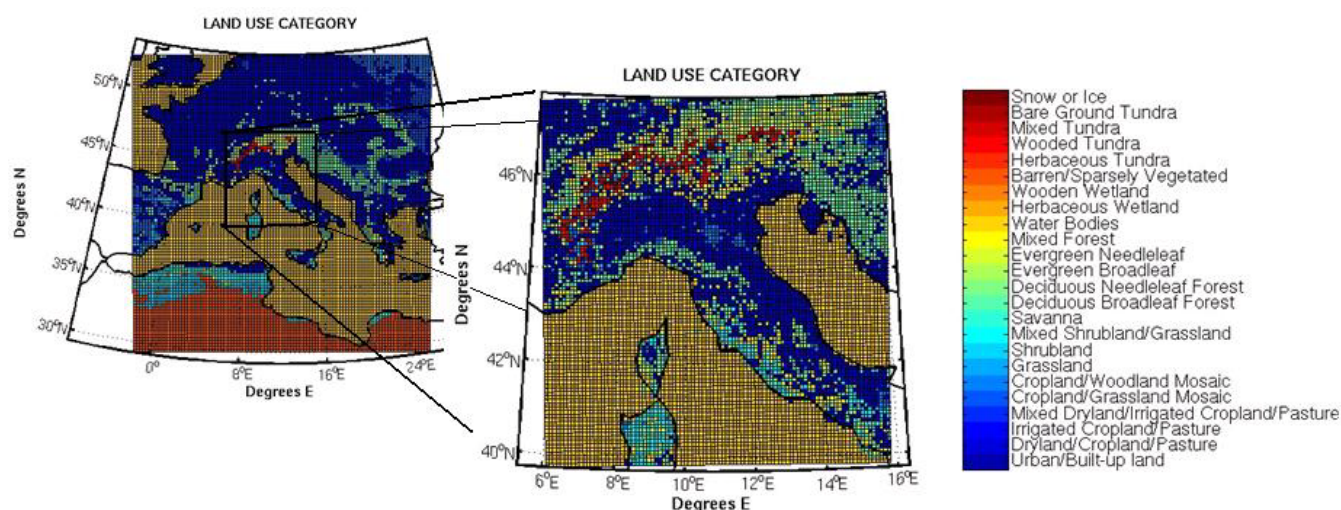


Figure 3-4: The two European domains plotted with their 24 USGS landuse category, plotted in matlab.

Southern Africa

A seven month long simulation, from October 1st 2000, to April 30th 2001 has been executed in order to estimate the accumulated flux of ozone over an entire maize growing season. The growing season of 2000-2001 was chosen in order to compare the results to those of Zunckel, et al.(2006).

The simulations have been executed by re-initializing the meteorology every seven days. Data interpolated to a resolution of $0.25^\circ \times 0.25^\circ$ from the ECMWF⁹ model are used as initial- and boundary conditions for the meteorology. For every re-initialization, the chemistry field of the previous day has been used as initial conditions for the chemistry module.

The domain covers mainland Africa, south of 13°S , with a resolution of $27\text{km} \times 27\text{km}$. The domain is presented in Figure 3-5.

⁸ ECMWF is the European Centre for Medium-range Weather Forecast.

⁹ ECMWF is the European Centre for Medium-range Weather Forecast.

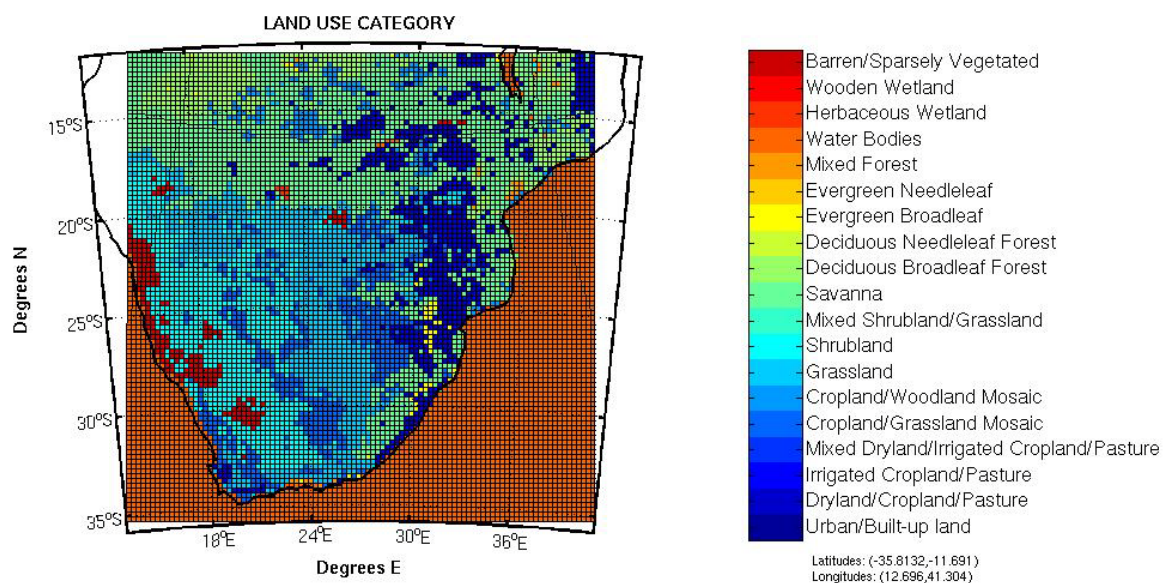


Figure 3-5: The southern African domain, with the 24 category USGS landuse categories.

3.3.2 Settings

For the gas phase chemistry the RADM2 mechanism was chosen, which gives a good balance between chemical detail, accuracy in predictions and run time. Inorganic species included in the RADM2 mechanism are 14 stable species, 4 reactive intermediates, and 3 abundant stable species (oxygen, nitrogen and water). The organic species included are 26 stable species and 16 peroxy radicals, where similar organic species are grouped together through the use of reactivity weighting (Grell, Peckham et al. 2005). Details of the organic chemistry of the RADM2 mechanism is found in Middleton et al. (1990). The reactions included in RADM2 are listed in Appendix B. A quasi steady-state approximation is used to predict chemical production and loss. Initial and boundary conditions for the prognostic gas-phase variables consist of laterally invariant vertical profiles representing a clean, mid-latitude oceanic conditions (Based on McKeen, Wotawa et al. 2002). The downside to using the RADM2 scheme in this context, is its lack of a wet-deposition scheme. In cases of rain this might cause an overestimation of the NO_x concentration (see Eq.2-3, page 1534) and thus possibly in some cases the ozone concentration.

Table 3-2: The choices for physics schemes made for the simulations in this study.

Physics schemes	
Photolysis	Madronich F-TUV photolysis scheme
Boundary layer	Mellor-Yamada-Janjic TKE scheme
Surface layer	Monin-Obukhov (Janjic) scheme
Microphysics	Lin et al. scheme
Land-Surface Physics	Noah land-surface model

For photolysis the Madronich F-TUV photolysis scheme was chosen. It is coupled with hydrometeors, aerosols, and convective parameterizations. The Madronich F-TUV scheme

available in WRF V3.1 is computationally faster, although it does not work with all aerosol options. As aerosols are not included in these simulations, this is of little importance.

Boundary layer scheme chosen is the Mellor-Yamada-Janjic turbulent kinetic energy (TKE) scheme. The parameterization of turbulence in the planetary boundary layer and in the free atmosphere is described in Janjic (2002), and represents implementation of the Mellor-Yamada Level 2.5 turbulence closure model, over the entire range of atmospheric turbulent regimes.

The surface layer parameterization is done by the Monin-Obukhov (Janjic) scheme (Janjic 2002), based on the Monin-Obukhov similarity theory. For the microphysics the Lin et al. scheme is chosen as a sophisticated microphysics scheme, suitable for use in research studies. For the land-surface physics the unified Noah land-surface model is used.

3.3.3 Emissions

The biogenic emissions are computed online using a biogenic emission module (based on the description of Guenther, Zimmerman et al. 1994; Simpson 1995; Schoenemeyer, Richter et al. 1997). The module treats the emissions of isoprene, monoterpenes, other biogenic VOC (OVOC), and nitrogen emission by the soil. For the use in the RADM2 photochemistry module, the emissions of monoterpenes and OVOC are broken into parts and divided into the appropriate species classes. The isoprene emissions of agricultural and grassland areas, emissions of monoterpenes, OVOC, and nitrogen are treated as functions of the temperature only. The emission of isoprene by forests depends on both temperature and photosynthetic active radiation (PAR). It should be noted that the emissions are based on the 24 USGS landuse system classification, which does not include any tree-species information or fractional coverage, and so the emissions can only be roughly estimated.

For the anthropogenic emissions the RETRO 0.5° x 0.5° resolution emissions inventory has been used (RETRO 2006), and for Europe also the INERIS 0.1° x 0.1° inventory were used. The INERIS data are EMEP emissions (<http://www.emep.int>), downscaled from a 50km x 50km grid, by the INERIS1 group (personal communication; Bertrand Bessagnet), for the FP7 CityZen project, using GlobCover data (<http://ionia1.esrin.esa.int>), and is only available within the EMEP covered area.

A Fortran programme developed by Hodnebrog (2008) has been used to convert and regrid the emissions data to the appropriate metrics and WRF grid, and to convert the emissions into the grouped RADM2 species appropriate as WRF-input. It also rewrite the data to binary files suitable as input files to WRF-Chem (for more detailed information on the emissions programme, see Hodnebrog 2008).

Examples of combined RETRO and INERIS for the ozone precursors NO_x and CO - emissions for the European domain (for mid-day June 2007) are shown in Figure 3-6 together with RETRO NO_x and CO emissions from the Southern African domain (mid-day December 2000).

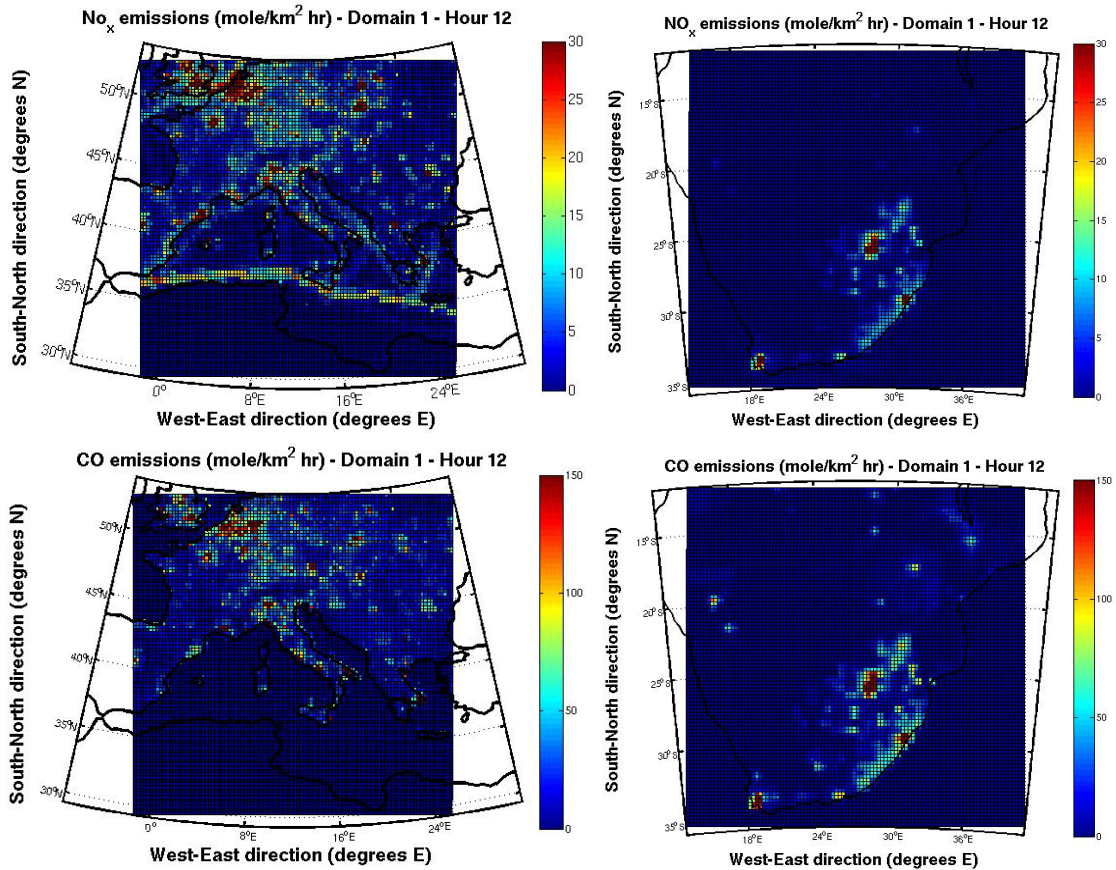


Figure 3-6: Emissions of NO_x (top panels) and CO (bottom panels). European emissions for June 2007 12:00 local time (left panels), emissions in the Southern African domain for December 2000, 12:00 local time (right panels). All emissions are in mole/km²hr.

In the South African domain the emissions are dominated by the heavily industrialized South African Highveld and biomass burning.

3.4 Dry deposition in WRF-Chem

One main focus of this thesis is dry deposition and fluxes of ozone from the surrounding atmosphere into the surface vegetation. For this purpose the WRF-Chem dry deposition scheme has been utilized. In the following is a detailed description of the WRF-Chem dry deposition scheme.

The dry deposition of gaseous species and aerosols in WRF-Chem is based on the article by M. L. Wesely, “*Parameterization of surface resistances to gaseous dry deposition in regional-scale numerical models*” (Wesely 1989). (The deposition of SO₂ has been replaced by parameterizations based on the article by Erisman et al. (1994)).

Wesely uses the “Big-leaf” approach, where the surface vegetation is treated as one big canopy. To account for the different properties of various types of vegetation, the dry deposition scheme is coupled with the soil/vegetation scheme. 24 USGS (US Geological Survey) land use categories, and five seasonal categories are used to classify the plant/soil properties. The USGS 30 “ resolution landuse categories are interpolated to the simulation domain in the WPS/geogrid program. Some of the landuse categories are in the Wesely

scheme grouped together, by giving them the same value for the constants included in the dry deposition scheme that are only land-use and season dependent, as described in Table 3-3 below.

Table 3-3: USGS landuse categories and corresponding Wesely type and/or season.

USGS Landuse category	Wesely type
1: Urban and built-up land	1: urban land
2: Dryland cropland and pasture	2: agricultural land
3: Irrigated cropland and pasture	2: agricultural land
4: Mixed dry/irrigated cropland and pasture	2: agricultural land
5: Cropland/grassland mosaic	2: agricultural land
6: Cropland/woodland mosaic	4: deciduous forest
7: Grassland	3: range land
8: Shrubland	3: range land
9: Mixed shrubland/grassland	3: range land
10: Savanna	3: range land ,always summer
11: Deciduous broadleaf forest	4: deciduous forest
12: Deciduous needleleaf forest	5: coniferous forest, autumn and winter modi
13: Evergreen broadleaf forest	4: deciduous forest,always summer
14: Evergreen needleleaf forest	5: coniferous forest
15: Mixed Forest	6: mixed forest including wetland
16: Water Bodies	7 water, both salt and fresh
17: Herbaceous wetland	9: nonforested wetland
18: Wooded wetland	6: mixed forest including wetland
19: Barren or sparsely vegetated	8: barren land, mostly desert
20: Herbaceous Tundra	9: nonforested wetland
21: Wooded Tundra	6: mixed forest including wetland
22: Mixed Tundra	6: mixed forest including wetland
23: Bare Ground Tundra	8: barren land, mostly desert
24: Snow or Ice	- Always winter
25: No data	8: barren land, mostly desert

The five seasonal categories are:

1. Autumn with unharvested cropland
 2. Late autumn with frost, no snow
 3. Midsummer with lush vegetation
 4. Transitional spring with partial green coverage.
 5. Winter, snow on ground and subfreezing
- (Wesely 1989)

The flux of trace gases and particles from the atmosphere to the surface is calculated by multiplying the deposition velocity for each gas with the gas concentration in the bottom layer of the model.

$$F_x = v_{x,y} \Delta C_z$$

(3-5)

where ΔC_z is the difference in concentration of the trace gas between the bottom layer of the model, and inside the canopy and ground. The concentration inside the vegetation and in the soil is assumed to be zero, and so the difference will simply be the trace gas concentration in the air surrounding the canopy, in the model bottom layer. $v_{x,y}$ is the spatially varying

deposition velocity. The deposition velocity is dependent on the gas properties, the vegetation, and various meteorological parameters.

Wesely (1989) calculates the deposition velocity utilizing the resistance analogy (see Chapter 2.2.3). The deposition velocity reflects the conductance, and is given as the reciprocal of the overall surface resistance.

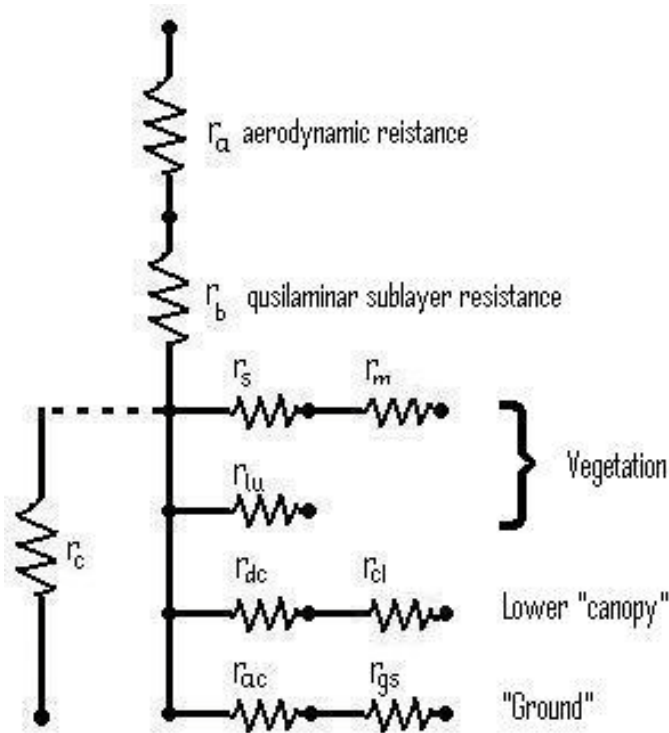


Figure 3-7: Schematic diagram of the pathway resistances used in the Wesely module. (Modified from Wesely (1989))

From the resistance network introduced by Wesely (1989), which can be seen in Figure 3-7, we can see that the total surface deposition velocity v_d is given as the sum of the reciprocal of three resistances placed in series.

$$v_d \equiv [r_a + r_b + r_c]^{-1}$$

(3-6)

r_a represents the aerodynamic resistance of the turbulent air between a specified height above the canopy and the surface. r_b gives the resistance of the quasilaminar sub layer adjacent to the surface, and r_c represents the bulk surface resistance, including the plant canopy and the soil, and is computed as the sum of seven minor resistances, to account for the various processes controlling the flux of gas particles deposited at the surface.

Computing r_a and r_b

The aerodynamic resistance depends only on meteorological properties of the turbulent air above the canopy. In the dry deposition scheme the reciprocal of the sum of the aerodynamical and the quasilaminar sublayer resistances is used to calculate a deposition velocity at a reference height, based on the work by McRae, Goodin et al. (1982)

$$v_g = \frac{F}{c(z_r)} = \frac{1}{(r_a + r_b)}$$

(3-7)

This velocity forms an upper limit rate at which particles and gaseous material is removed at the surface, the “big leaf” canopy, with resistance r_c .

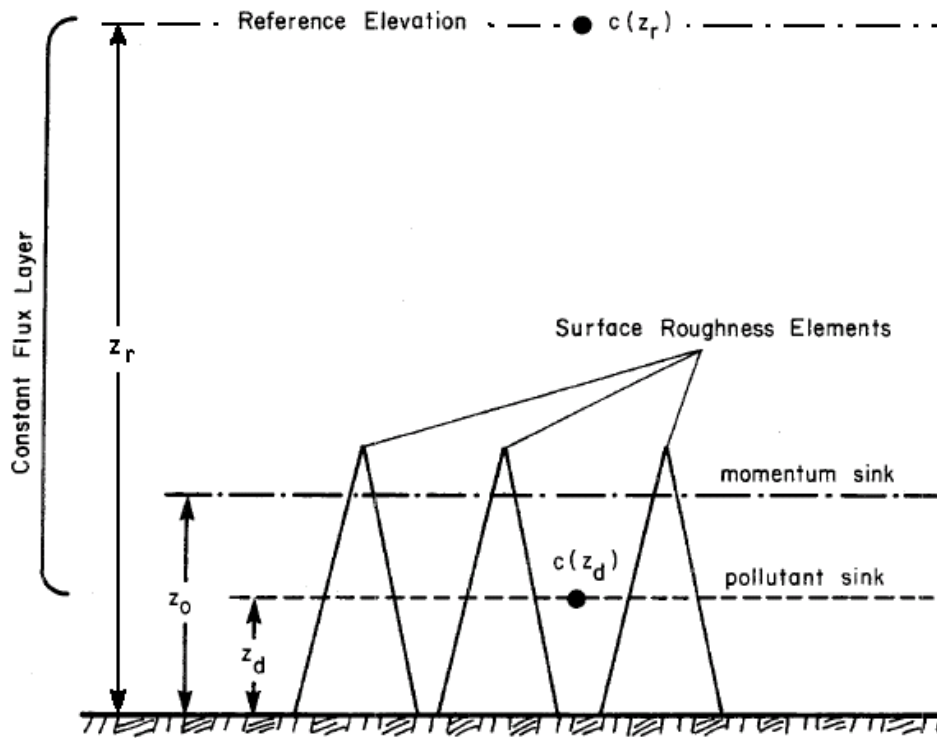


Figure 3-8: Idealized representation of the airshed surface.(modified from (McRae, Goodin et al. 1982))

An idealized representation of the surface is shown in Figure 3-8. The reference elevation is set equal to 2 meters above the surface in WRF. z_0 is the surface roughness length associated with momentum sink. z_d is the zero-plane displacement, where the pollutant concentration is assumed to tend to zero.

Some assumptions are made in calculating v_g . Within the layer $0 \leq z \leq z_r$ the deposition is assumed to be one-dimensional, steady state, and as a constant flux without re-entrainment. The deposition flux can then be described as

$$F = [K_p(z) + D] \frac{dc}{dz} + v_t c(z)$$

(3-8)

$K_p(z)$ represents the pollutant eddy diffusion coefficient, and D is the molecular diffusion coefficient of the material in air. The v_t represents the terminal settling deposition velocity for particulate material, which for gaseous material can be set equal to zero. Integrating the expressions for the flux F given in (3-7) and (3-8), we get

$$\int_{z_d}^{z_r} \frac{dz}{[K_p(z) + D]} = \int_{c(z_d)}^{c(z_r)} \frac{dc}{[v_g c(z_r) - v_t c(z)]}$$

(3-9)

The settling velocity v_t is assumed to be zero for gaseous material, so Equation (3-9) can be written as

$$v_g = \frac{\left[1 - \frac{c(z_d)}{c(z_r)}\right]}{\int_{z_d}^{z_r} \frac{dz}{[K_p(z) + D]}}$$

(3-10)

Since the dry deposition velocity is computed for the surface layer of the atmosphere, an expression for the pollutant eddy diffusion coefficient $K_p(z)$ is given using the Monin-Obukhov similarity theory.

$$K_p(z) = k \frac{u_* z}{\phi_p\left(\frac{z}{L}\right)}$$

(3-11)

The velocity shear, $\frac{\partial u}{\partial z}$ is given as

$$\frac{\partial u}{\partial z} = \frac{u_*}{kz} \phi_m\left(\frac{z}{L}\right)$$

(3-12)

where k is von Kármán's constant, u_* is the friction velocity, and L is the Monin-Obukhov length. ϕ_p and ϕ_m are universal functions for respectively pollution transport and momentum, determined by experiments. For this model, the following expressions have been determined for the various stability conditions;

$$\phi_m\left(\frac{z}{L}\right) = \begin{cases} 1 + 4.7\left(\frac{z}{L}\right) & \text{stable; } \left(\frac{z}{L}\right) > 0 \\ 1 & \text{neutral; } \left(\frac{z}{L}\right) = 0 \\ \left[1 - 15\left(\frac{z}{L}\right)\right]^{-\frac{1}{4}} & \text{unstable; } \left(\frac{z}{L}\right) < 0 \end{cases}$$

(3-13)

$$\phi_p\left(\frac{z}{L}\right) = \begin{cases} 0.74 + 4.7\left(\frac{z}{L}\right) & \text{stable; } \left(\frac{z}{L}\right) > 0 \\ 0.74 & \text{neutral; } \left(\frac{z}{L}\right) = 0 \\ 0.74\left[1 - 9\left(\frac{z}{L}\right)\right]^{-\frac{1}{2}} & \text{unstable; } \left(\frac{z}{L}\right) < 0 \end{cases}$$

(3-14)

In the surface layer, the contribution to the diffusion by molecular diffusion is considered to be negligible compared to that of the turbulent diffusion. Applying this to Equation (3-10), and substituting for $K_p(z)$, the expression for the upper limit velocity becomes

$$v_g = \frac{k \left[1 - \frac{c(z_d)}{c(z_r)}\right]}{\int_{z_d}^{z_r} \frac{1}{zu_* k} \phi_p\left(\frac{z}{L}\right) dz}$$

(3-15)

Further the assumption is made that u_* does not vary with height in the surface layer, and thus can be removed from the integral, and $\phi_p \cong 1$ for $z_d \leq z \leq z_0$, and so the equation can be expanded to give

$$v_g = \frac{k^2 u(z_r) \left[1 - \frac{c(z_d)}{c(z_r)}\right]}{\left[\int_{z_0}^{z_r} \phi_m\left(\frac{z}{L}\right) \frac{dz}{z}\right] \left[\ln\left(\frac{z_0}{z_d}\right) + \int_{z_0}^{z_r} \phi_p\left(\frac{z}{L}\right) \frac{dz}{z}\right]}$$

(3-16)

However, transfer over the quasilaminar sublayer adjacent to the surface is also dependent on the diffusivity of the material being transferred. To account for this, based on the assumptions made by Wesely and Hicks (1977), a substitution of a surface transfer function is made;

$$\ln\left(\frac{z_0}{z_d}\right) = 2\left(\frac{Sc}{Pr}\right)^{2/3}$$

(3-17)

where Sc is the Schmidt number¹⁰ and Pr is the Prandtl number¹¹ for air. In WRF the values for these parameters are $Sc = 1.15$, og $Pr = 1.0$.

The complete expression for the upper limit deposition velocity is now given as

$$v_g = \frac{k^2 u(z_r) \left[1 - \frac{c(z_d)}{c(z_r)} \right]}{\left[\int_{z_0}^{z_r} \phi_m \left(\frac{z}{L} \right) \frac{dz}{z} \right] \left[2 \left(\frac{Sc}{Pr} \right)^{2/3} + \int_{z_0}^{z_r} \phi_p \left(\frac{z}{L} \right) \frac{dz}{z} \right]}$$

(3-18)

From Equation 3-18 it is apparent that the velocity varies with meteorological conditions like stability. This implies that under typical conditions there will be a significant diurnal variation in the deposition, and that the velocity calculated is sensitively dependent on the height above the surface.

The upper limit deposition velocity is now calculated at the reference height of 2 meters above ground. The flux of material removal at the reference height is given as

$$F \equiv -K_p(z) \frac{\partial c}{\partial z} \Big|_{z=z_r} = -v_g(z_r) c(z_r)$$

(3-19)

To calculate the flux we need the value of gas concentration at the reference height of two meters. As the model only calculates the average grid cell gas concentration, an equivalent deposition velocity is calculated, which together with the cell average gas concentration will give the correct value for the flux at the reference height.

¹⁰ Schmidt number is the ratio of the shear component for diffusivity to the diffusivity for mass transfer
 $D: Sc = \frac{\nu}{D}$

¹¹ The Prandtl number is a dimensionless number approximating the ratio of momentum diffusivity (kinematic viscosity), ν and thermal diffusivity α . $Pr = \frac{\nu}{\alpha}$

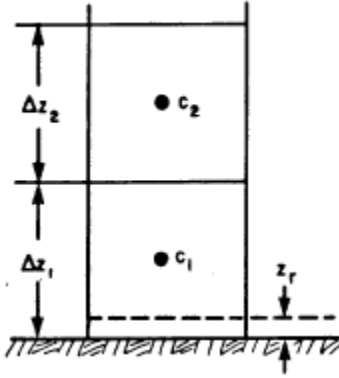


Figure 3-9: Simple illustration of the models two bottom layer cells. (McRae, Goodin et al. 1982)

To calculate the equivalent deposition velocity it is assumed that most of the model bottom layer is within the surface or constant flux layer. Then the cell deposition velocity can be given as

$$\overline{v_g} = \frac{v_g(z_r)c(z_r)}{c_1}$$

(3-20)

where c_1 represent the average value of the vertical gas concentration distribution in the range of $z_r \leq z \leq \Delta z$, Δz being the height of the cell. It can be expressed as

$$c_1 = \frac{1}{\Delta z - z_r} \int_{z_r}^{\Delta z} c(z) dz$$

(3-21)

Within the constant flux layer the concentration at any height can now be written as

$$c(z) = c(z_r) \left[1 + v_g(z_r) \int_{z_r}^{\Delta z} \frac{1}{K_{p(z)}} dz \right]$$

(3-22)

And the final cell average deposition velocity $\overline{v_g}$ can be expressed as

$$\overline{v_g} = \frac{v_g(z_r)}{1 + \frac{v_g(z_r)}{ku_*(\Delta z - z_r)} \int_{z_r}^{\Delta z} \int_{z_r}^z \phi_p \left(\frac{x}{L} \right) \frac{dx}{x} dz}$$

(3-23)

The integrals needed to evaluate the denominator integrals of this expression can be found in in Appendix A.

The graph in Figure 3-10 illustrates the variation of the cell average deposition velocity as a function of atmospheric stability and the cell height.

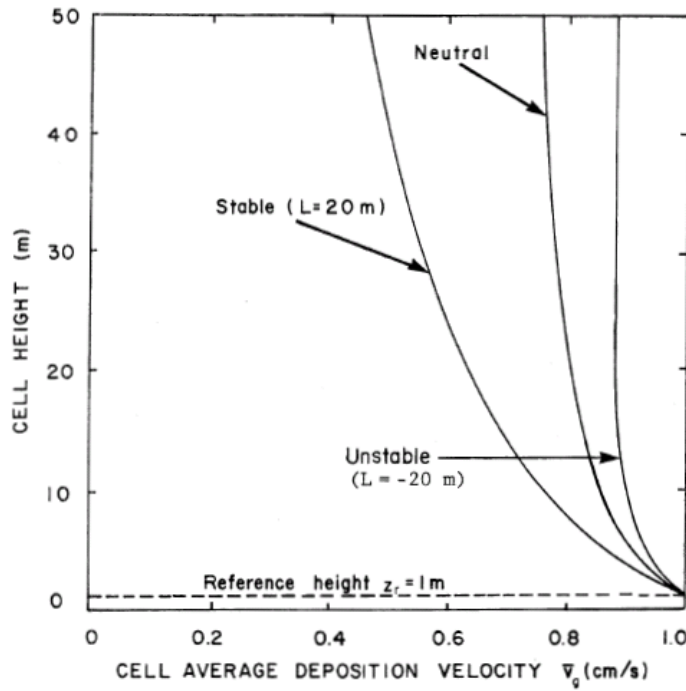


Figure 3-10: Variation of the average deposition velocity as a function of atmospheric stability and the cell height. ($z_0 = 0.01\text{ m}$, $u = 2.5\text{ m/s}$, $v_g(z_r) = 0.01\text{ m/s}$) (McRae, Goodin et al. 1982)

Calculation of r_c

The bulk surface resistance consists of seven resistances, placed in four parallel pathways (see Figure 3-7). Mathematically the expression for r_c can be written

$$r_c = \left[\frac{1}{r_s + r_m} + \frac{1}{r_{lu}} + \frac{1}{r_{dc} + r_{cl}} + \frac{1}{r_{ac} + r_{gs}} \right]^{-1}$$

(3-24)

The assumption is made that the concentration representative of the mesophyll, upper and lower canopy, and soil substrates are in equilibrium with the air concentration, and equal to zero. It is clearly stated in Wesely (1989) that the separate resistances in this expression should not be given too much emphasis separately, but are scaled and developed to give the best possible result of the overall surface resistance r_c . Here follows a short description of each of the resistances and the parameters used in expressing them, for more details, see Wesely (1989).

The stomatal resistance is describing of the resistance encountered by the trace gas as it passes through the stomatal openings of the leaves. As described in Chapter 2.2.1, the stomatal openings depend on various meteorological parameters. In the Wesely expression for stomatal resistance the surface temperature and the solar radiation is accounted for;

$$r_s = r_i \{ 1 + [200(G + 0.1)^{-1}]^2 \} \{ 400[T_s(40 - T_s)]^{-1} \}$$

(3-25)

where G is the solar irradiation in Wm^{-1} , and T_s is the surface air temperature between 0 and $40^\circ C$. Outside this temperature range the resistance is set to the very large value, to implement the assumption that the stomatal transfer has stopped. r_i represent the minimum stomatal resistance for water vapor, included to increase the minimum value of the stomatal resistance to account for the effect of water stress on the stomatal transfer (Wesely and Hicks 1977). For values for r_i see Appendix A.

After passing through the stomata, the gas encounters the mesophyll resistance. The expression for the mesophyll resistance for gas x is given as

$$r_{mx} = \left(\frac{H^*}{3000} + 100f_o \right)^{-1}$$

(3-26)

This resistance is computed utilizing two key parameters. The first one is H^* , the effective Henry's law constant, which is used to scale the rates of uptake by wet and moist surfaces to that of SO_2 . By utilizing this parameter, the assumption is made that uptake after dissolution is quite effective. This applies to the extracellular water in the substomatal cavities, and to all wet surfaces and water bodies outside the plant. The other parameter f_o , is the reactivity factor for oxidation of biological substances. Three values are used to scale the gas' reactivity relative to that of ozone.

- $f_o = 1$; the gas is as highly reactive as ozone.
- $f_o = 0.1$; the gas is slightly reactive, used to allow rapid uptake through plant stomata and mesophyll.
- $f_o = 0$; non-reactive.

More details regarding the values of H^* and f_o are found in Wesely (1989). A table of values for H^* and f_o is found in Appendix A.

The expression for the mesophyll resistance is based on the assumption that there are two effective parallel pathways into the substomatal mesophyll, one for gases of high solubility, like SO_2 , and one for highly reactive gases, like O_3 . This implies that the mesophyll resistance for these two gases are near zero, and for simplicity, the value of the mesophyll resistance is set equal to zero for both O_3 and SO_2 .

The combined minimum stomatal and mesophyll resistance of substance x is calculated by scaling the stomatal resistance by the ratio of the molecular diffusivity of water vapor, D_{H_2O} , and that of the gas in interest, D_x .

$$r_{smx} = r_s \frac{D_{H_2O}}{D_x} + r_{mx}$$

(3-27)

Parallel to the stomatal pathway for gas deposition to the canopy is the cuticular pathway, the resistance of which is expressed as;

$$r_{lux} = r_{lu}(10^{-5}H^* + f_o)^{-1}$$

(3-28)

where r_{lu} are empirically determined values found in Appendix A. Again this expression allows for two parallel pathways for transfer, one for highly soluble gases and one for highly reactive gases.

If the surface is wetted by dew or rain, the expression for the cuticular resistance is changed. For SO_2 the uptake is expected to increase by a wetted surface, and the expression is simply set to a low value; $r_{lus} = 100 \text{ s m}^{-1}$. For ozone, the dew functions as an extra barrier for uptake, which is expected to be retarded, and the expression becomes

$$r_{luo} = \left[\frac{1}{3000} + \frac{1}{3r_{lu}} \right]^{-1}$$

(3-29)

The second term on the right hand side of this expression takes into account the reduced dry area available for transfer.

In the case of rain-wetted surfaces, the expression for SO_2 is replaced by

$$r_{lus} = \left[\frac{1}{5000} + \frac{1}{3r_{lu}} \right]^{-1}$$

(3-30)

The equivalent term for O_3 is

$$r_{luo} = \left[\frac{1}{1000} + \frac{1}{3r_{lu}} \right]^{-1}$$

(3-31)

For other gases than SO_2 or O_3 the following term is used for either dew or rain wetted surfaces, taking into account the three factors of reduced dry area, solubility in water and reactivity factor, respectively, for the terms on the right hand side.

$$r_{lux} = \left[\frac{1}{3r_{lu}} + 10^{-7}H^* + \frac{f_o}{r_{luo}} \right]^{-1}$$

(3-32)

On the next branch of the resistance network in Figure 3-7, we find the resistance of the exposed surfaces in the lower part of the canopy, such as twigs, bark and leaves.

$$r_{clx} = \left[\frac{H^*}{10^5 r_{cls}} + \frac{f_o}{r_{clo}} \right]^{-1}$$

(3-33)

The two terms on the right hand side have the same function as in previous terms, and the values for r_{clo} are found in Appendix A.

Placed in series on the same branch of the network tree is the resistance of buoyant convection in the canopy. This is to account for the mixing forced by buoyancy induced by sunlight heating the ground beneath the canopy, and wind penetrating it on the sides of hills. The expression is thus dependent on irradiance G , and the slope of the local terrain, θ (in radians).

$$r_{dc} = 100[1 + 1000(G + 10)^{-1}](1 + 1000\theta)$$

(3-34)

The last pathway on the network tree consists of two resistances. r_{ac} is the resistance of gas transfer which is dependent on the canopy height and density. As the model does not have any input regarding the specific plants, the values for this resistance is assigned only on the basis on landuse and season, and the values are found in Appendix A.

The resistances of buoyancy and gas transfer in the canopy are placed in parallel in this model to more easily be manipulated to match empirical findings. It would be more realistic to have them placed in series for especially deep and dense vegetation.

The final resistance is that of soil and ground litter beneath the canopy, water bodies and bare ground. The expression for this varied surface is

$$r_{gsx} = \left[\frac{H^*}{10^5 r_{gss}} + \frac{f_o}{r_{gso}} \right]^{-1}$$

(3-35)

All surfaces represented by r_{cl} and r_{gs} are expected to increase the resistance to uptake when cold, and corrections are made in cases of low surface temperatures.

3.5 Measured data

The modelled results of this thesis are compared to measurements published in part in Gerosa et al. (2009a.). Dr. Gerosa and his colleges in Brescia provided data from this field campaign for comparison and validataion of the model.

The data was sampled during a field campaign in in a typical maquis ecosystem in Castelporziano, Italy (N 41° 40' 49.3'', E 12° 23' 30.6'') in 2007. The measurements were made over the period May 5th to July 31st (Gerosa, Finco et al. 2009a).

Simulations by the EMEP model has shown the



3-1: Location of measurements; Grotta di Piastra, Castelporziano Presidential estate near Rome, Italy. (Picture from Gerosa, Vitale et al. 2005)

Mediterranean ecosystems to be some of the highest risk areas in Europe for ozone induced damage to vegetation (Simpson, Ashmore et al. 2007). This is because of high emissions of ozone precursors close to the ecosystems and favourable climatic conditions for ozone formation (Gerosa, Finco et al. 2009a). The risk of damage to the vegetation was investigated during this field campaign, using both AOT40 and AFstY metrics, adopting UNECE critical values and thresholds ($Y=1,6 \text{ nmol m}^{-2} \text{ s}^{-1}$, $CL=4 \text{ mmolm}^{-2} \text{ PLA}$, 5000 ppb h for AOT40), resulting in values well above the critical levels at which adverse effects could be expected for both metrics.

Ozone, water and energy fluxes were measured over the period, by the eddy covariance technique. This technique is turbulence based, and states that the fluxes are equal to the covariance between the vertical component of the wind and the measured scalar quantity. Assuming the average vertical wind component equals zero, and the absence of chemical loss- and production processes between the ground and measuring height, the vertical fluxes of ozone, sensible and latent heat can be calculated as

$$F_{O_3} = \overline{w'C'} \quad (\text{ppb ms}^{-1}) \quad (3-36)$$

$$H = \rho c_p \overline{w'T'} \quad (\text{W m}^{-2}) \quad (3-37)$$

$$\lambda E = \lambda \rho \overline{w'q'} \quad (\text{W m}^{-2}) \quad (3-38)$$

where C is the ozone concentration (ppb), T is the air temperature ($^{\circ}\text{C}$), q is the specific humidity (kg water vapour/kg air), ρ is the air density (kg m^{-3}), c_p is the specific heat of the air ($\text{J kg}^{-1} \text{ K}^{-1}$), and λ is the constant for water vaporization ($\text{J kg}^{-1} \text{ K}^{-1}$). The primes represent the fluctuations of the variable around its mean, and the bars represent averages over the selected time period of 30 minutes. For more details about the eddy covariance method, and the instrumentation used for measurements, see Gerosa et al. (2009a).

The stomatal flux of ozone was estimated utilizing a Dry Depositions Inferential Method (DDIM) based on a big leaf assumption. As in W89, the deposition process is considered to consist of three main phases, represented by three main resistances; the aerodynamical resistance (r_a), the resistance of the sublaminal boundary layer (r_b), and the surface resistance (r_c). The total resistance can then be expressed as the sum of these three, and equal to the ozone concentration at canopy height (C_m) (assuming the concentration inside the soil and vegetation is zero), divided by the flux from the air into the vegetation (F_{O_3});

$$r_{tot} = r_a + r_b + r_c = \frac{C_m}{F_{O_3}}$$

(3-1)

The concentration and the flux are derived directly from measurements, giving the value for the total resistance. The aerodynamic resistance is derived using Monin-Obukhov similarity theory, and the sub-laminar resistance is calculated using parameterization by Hicks et al. (1987). The surface resistance is then given as a residual as all of the other variables are known.

The surface resistance is divided in two; stomatal and non-stomatal resistance, and placed in parallel. The stomatal resistance is calculated by inverting the Penman-Monteith equation (Monteith 1981; Gerosa, Vitale et al. 2005) and solving it for the water vapour resistance, which is then scaled by the ratio of the diffusivity of ozone in air to that of water vapour, giving an expression for the stomatal resistance of ozone. When the stomatal resistance is known the non-stomatal one can be found as a residual, and finally the stomatal flux of ozone can be expressed as

$$F_{st} = \frac{r_c}{(r_a + r_b + r_c)r_{st}} C_m$$

(3-2)

Further details of the Penman-Monteith equation and calculations of the stomatal flux are found in Gerosa et al. (2005). Results of the measurements and its derivations are shown in the next chapter, together with the modelled estimates.

4 Results and Discussion

The results of the WRF-Chem simulations for the two 6-day periods covering Italy, and the 7-month long simulation in Africa will be presented in this chapter.

Comparison the modelled flux and ozone concentration with the measured ones from Castelporziano described in Gerosa et al. (2009a) (G09a hereafter) will give an indication of how well the model is estimating the surface ozone flux. Next the results are evaluated utilizing two different approaches for implementing water status in the form of VPD on the vegetation in the flux calculations.

Finally the results for the Southern African domain are presented, and evaluated according to UNECE standards for risk assessment, giving an estimate of the total accumulated flux over a 7-month growing season from October to April, 2000-2001.

4.1 Castelporziano, Italy

The location of the measuring site in Castelporziano, Italy (N 41 40' 49, 3", E 12 23' 30, 6") is covered by the WRF-Chem inner domain of 9km x9km resolution. The grid cell covering the site is picked, and the results presented here are the mean values of this grid cell. This gridcell is quite appropriately falls into the USGS landuse category of "mixed grassland/shrubland".

WRF-Chem simulations were executed for a selected six-day period for each of the spring and summer period. As can be seen from Figure 4-1 the two periods are quite representative of the field campaign as a whole. The first day of each of the periods is considered a "spin-up" day and is excluded from the presented results.

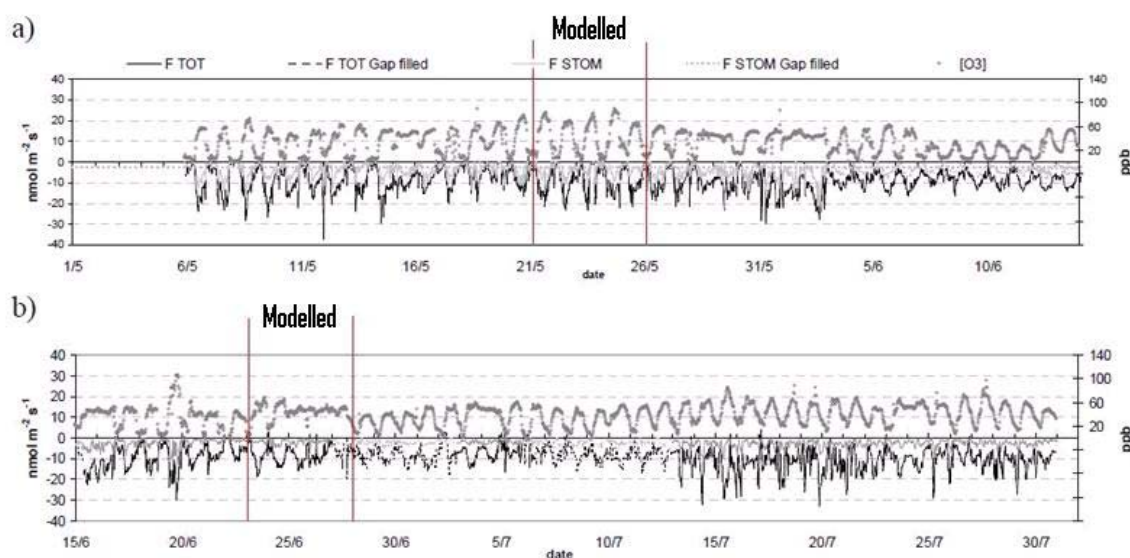


Figure 4-1: Measured ozone concentrations and fluxes for a) the spring period, and b) the summer period. The vertical lines indicate the two periods which have been simulated in WRF-Chem. (Modified from Gerosa, Finco et al. 2009a)

May 21-26

The first period is from May 20-26 and part of the “late-spring period” as defined in G09a. The meteorological conditions for this period were dominated by a regular night-time inversion, causing dew on the canopies in the night-time- and early-morning hours. The measured average temperature over the period was 21.2°C, and no rainfall was recorded over the period.

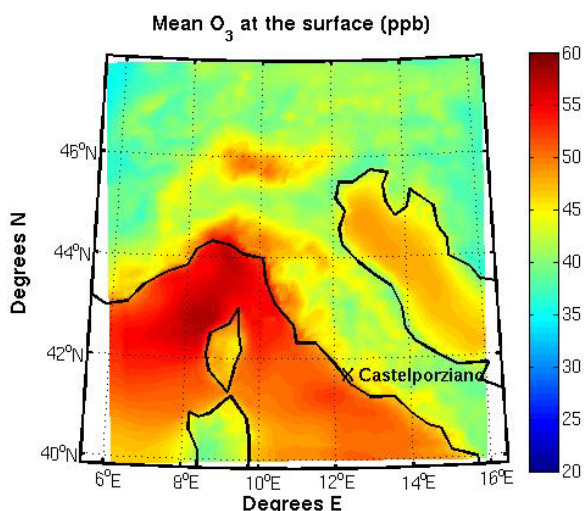


Figure 4-2: The average modelled ozone mixing ratio (ppb) over the period May 21-26.

The average ozone concentration at the measuring site was 32.6 ppb in the total late-spring period. The selected days are well above the average concentration, with a mean value of 42.1 ppb. This is not far from the modelled average of 41.4 ppb. According to G09a the ozone concentrations at the site were strongly influenced by the wind direction, with low values when downwind from Rome, and high values as the wind blew from the sea. Figure 4-2 shows the modelled average mixing ratio of ozone in the model bottom layer. The mean ozone concentration is higher over sea, and lower over land, as a result of the higher dry deposition to the

land surface. This seems to be consistent with the recorded measurements, where the ozone concentration at the Castelporziano site was higher when the wind was blowing from the sea.

The 9km x 9km grid cell covering the measurement site was selected and following time series and diurnal means are average values of this area.

In the wind-plots of Figure 4-3 show a regular diurnal variation in the measured wind at the Castelporziano site over the period. The wind is regularly blowing from south/southwest during the day, bringing with it high ozone concentrations from the sea. The wind reverses during night time. The same pattern is not recognized in the modelled results, where the plots show a more stable wind profile from north/north-west also during the day time over middle days of the period.

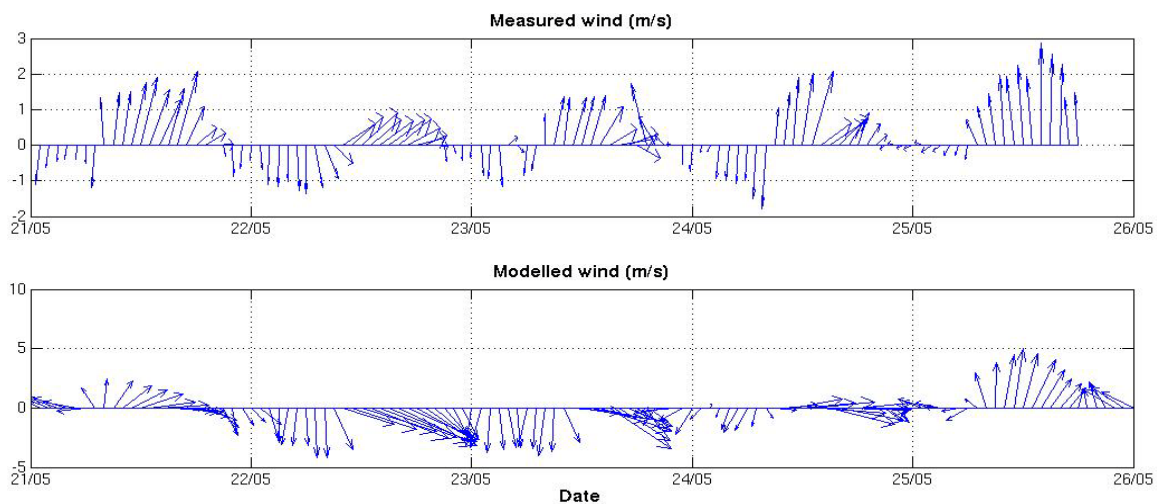


Figure 4-3: Measured wind speed and direction (top panel) and modelled wind speed and direction at 10m height (bottom panel), over the period May 21-26.

The modelled ozone mixing ratio, given as both the model bottom layer mean, and at modelled concentration at the projected canopy height is plotted in Figure 4-4, together with the measured ozone mixing ratio.

As seen in Figure 4-4 the measured ozone mixing ratio typically began rising at around 8 o'clock in the morning, local time (UTC+2 hours in summertime), and reached their top values in the early afternoon, displaying a typical bell-shaped form. The modelled values show a much more even diurnal mean distribution, although bell-shaped, with a significantly lower variability around the mean value, displaying both higher values in the night-time and early morning, and significantly lower mid-day maximum values. The lower daytime values of the modelled results might in part be explained by the difference in the modelled mean wind direction over the period, compared to the measured one. An underestimation of ozone precursor emissions is also possible. The high modelled values during the night might be due to an overestimation of the night-time boundary layer height, not efficiently enough “trapping” the ozone at the ground to be deposited.

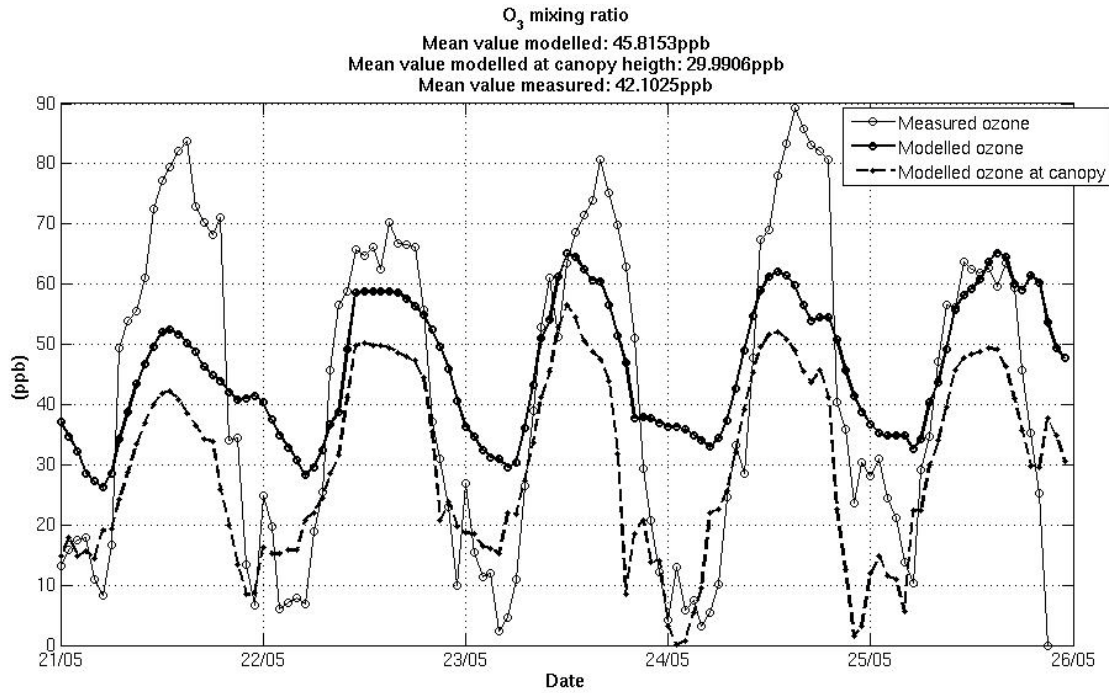


Figure 4-4: Ozone mixing ratio from measurements (thin line) and modelled (thick line) for the period may 21-26. The average value for the modelled ratio over the period is 45.9 ppb, and the average measured mixing ratio is 42.1 ppb. Maximum modelled value is 65.2 ppb, while the measured data reach a maximum value of 89.2 ppb. The average modelled value at canopy height is 30.0ppb.

The model bottom layer ozone concentration shown as the thick line in Figure 4-4 is given as the mean of the entire bottom layer. To more accurately present the concentration at the canopy height, the concentration has been scaled yielding the concentration actually used in the calculation of the stomatal flux. By using Equation 3-20 on page 54, the concentration at the reference point assumed to be close to the canopy height can be expressed

$$c(z_r) = c_1 \left(\frac{\bar{v}_g}{v_g(z_r)} \right)$$

(4-1)

where z_r is the reference height and \bar{v}_g is the total deposition velocity for the bottom layer, which has the mean ozone concentration of c_1 . By plotting this concentration the night-time values for ozone are substantially lower, as they are scaled by the reciprocal of the atmospheric stability, which is bigger during night time. The day-time values of the reference-height concentration however, are even more underestimated compared to the measured ones. The measuring height at the site is at 3.8 meters. Measuring the concentration of this height, some of the resistance below the measuring height might not be accounted for, like the quasilaminar sublayer resistance adjacent to the leaf, which is taken into account in the modelled concentration at the reference height. This might explain some of the deviance between the model's lower daytime concentration.

The average diurnal variation for the three described concentrations is shown in Figure 4-5. The average measured diurnal variation shows a considerable higher mean-daytime concentration than the modelled ones.

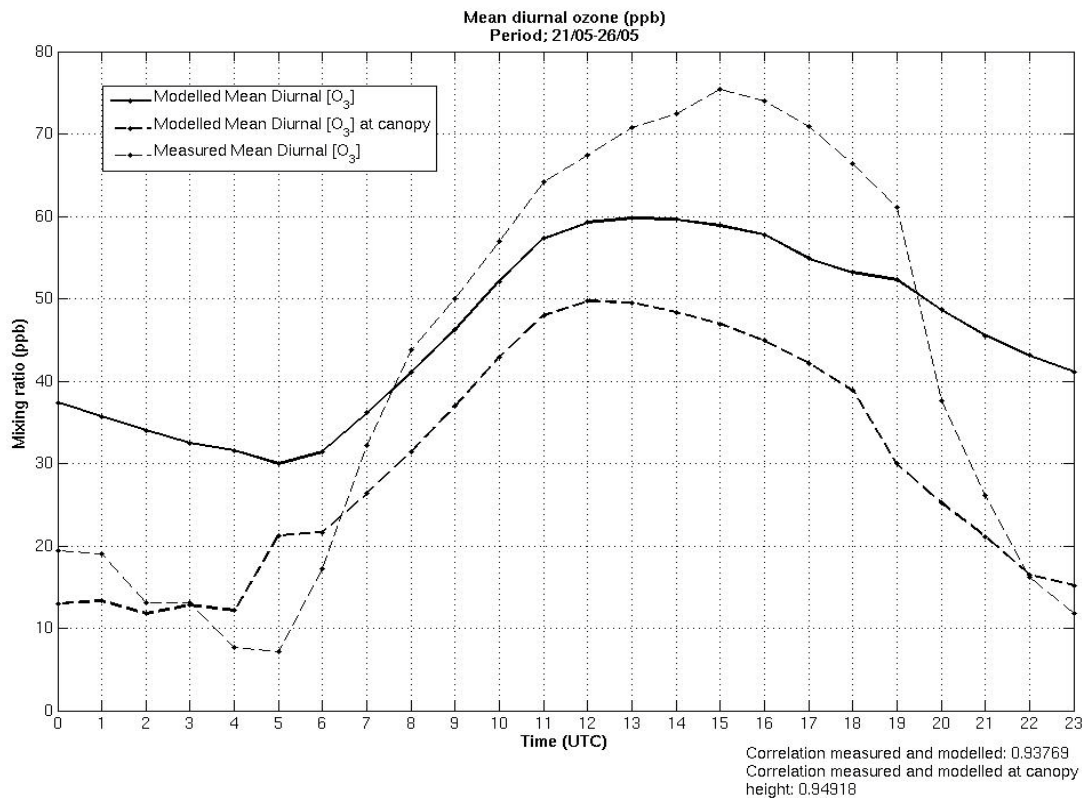


Figure 4-5: Average diurnal variation of ozone mixing ratios (ppb) over the period May 21-26. Modelled (thick line) measured (thin line) and the modelled scaled to canopy height (stippled line). The correlation between measurements and modelled bottom layer mean is 0,94, and between measured and scaled modelled mean is 0.95, as it better accounts for night-time and early morning concentrations.

The deposition velocity of the surface is given as the reciprocal of the surface resistance, in other words the conductance. The surface conductance and its components for the may-period are shown in Figure 4-6.

The different resistances represented by the conductances in Figure 4-6 are placed in series and in parallel according to the model resistance network as shown in Figure 3-7 on page 49. The horizontal lines are easily recognized as the resistances only dependent on the landuse category and season, as the season does not change within the timeperiod, and the red star-dotted line represents the combination of them all, the total surface conductance.

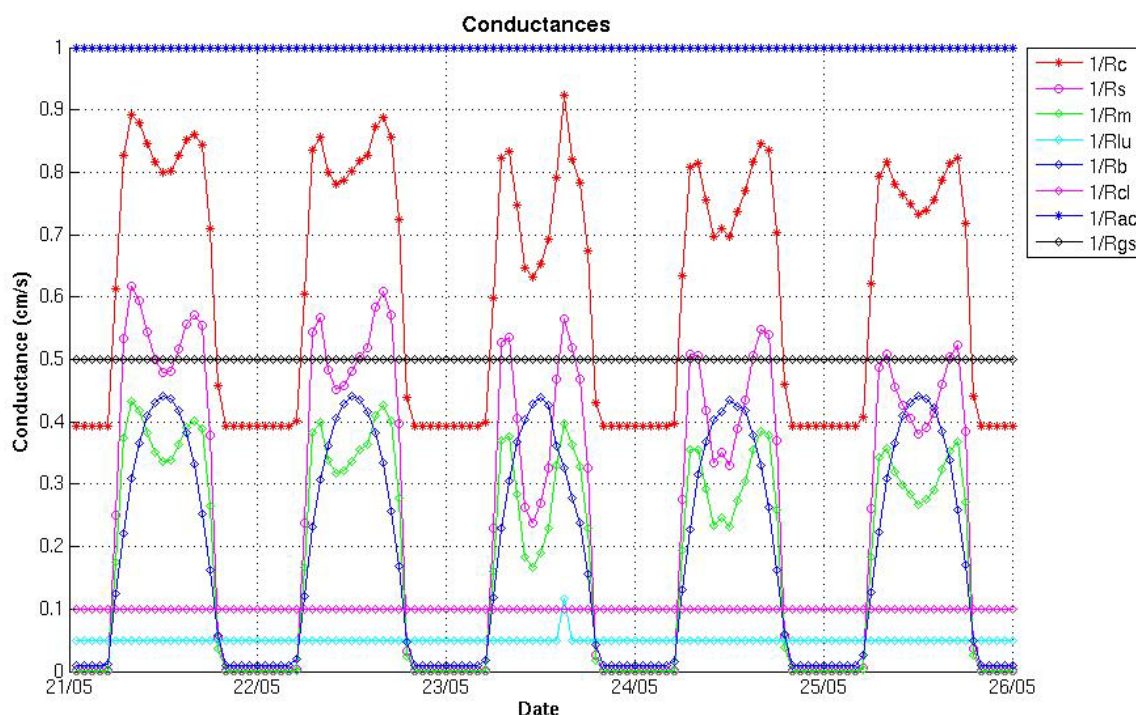


Figure 4-6: Values for the total plant and soil conductance given as $1/r_c$ (red line), and the seven different conductances it consists of. (R_s = stomatal resistance, R_m =combined stomatal and mesophyll resistance, R_{lu} = upper bulk canopy and healthy leaf cuticular resistance, R_b = resistance due to buoyancy within the canopy, R_{cl} = lower canopy cuticular resistance, R_{ac} = resistance due to air transfer within the canopy, R_{gs} = resistance of soil and ground litter)

The blue diamond-dotted line represents the conductance dependent on the buoyancy of the air inside the canopy, dependent on the incoming radiation, hence showing a bell shaped curve with a midday maximum. The pink line represents the stomatal conductance, dependent on the surface temperature and the incoming short wave radiation, and placed in series with the mesophyll conductance, which for ozone is assumed to be zero. This conductance is however not the one directly taking part in the calculation of the total surface conductance. The bright green line representing the combined minimum stomatal and mesophyll conductance, is scaled by the ratio of the molecular diffusivity of water vapor to that of ozone, and is the one representing the stomatal conductance of ozone into the vegetation.

The relative importance of the parallel pathways of the ozone flux is more accurately illustrated in Figure 4-7, where the sum of the lower conductances, representing each of the “branches” on the resistance network of Figure 3-7 on page 49, equals the red star-dotted line representing the total conductance of the surface vegetation and soil.

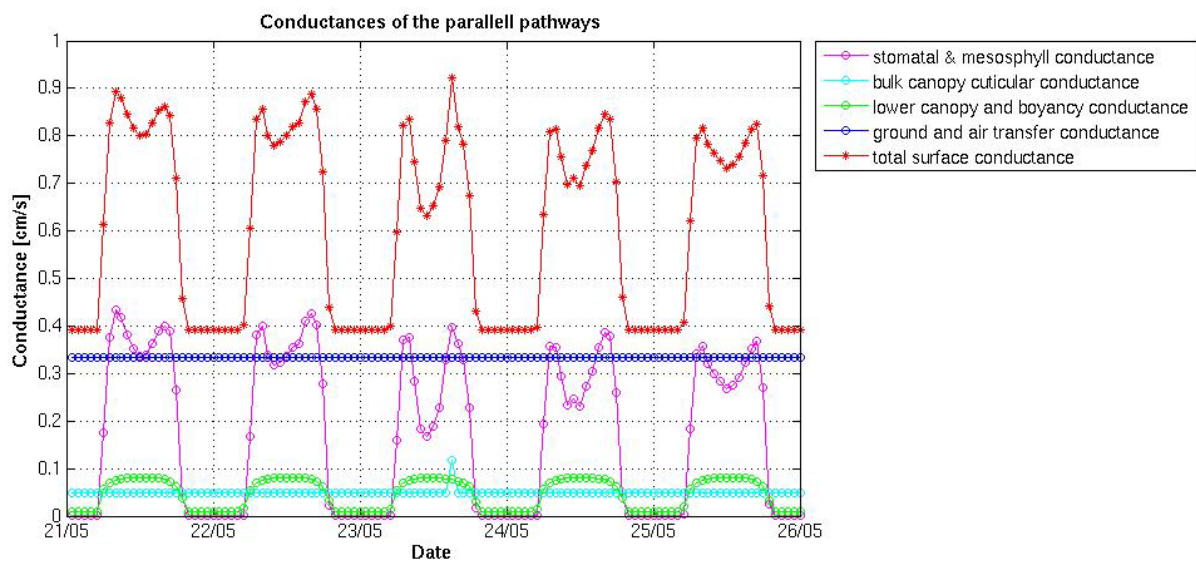


Figure 4-7: The total surface conductance given as $1/r_c$ and the conductances of the different pathways it consists of.

Notice in Figure 4-7 that the stomatal conductance (pink line) is zero during the night, a result of its dependance on short wave radiation (see Eq. 3-25 on page 55). Also notice the the conductance “dips” more or less during mid-day every day, and especially on May 23. This effect is a result of the stomatal conductance’s dependancy on surface temperature, causing it to close when it exceeds the “cut-off temperature” of 40°C, and partially close when it comes close, to simulate the plant’s defence against waterloss by closing the stomata when the surface temperature is high. As the temperature decreases again in the afternoon the stomatal conductance increases. The value of 40°C might be considered a somewhat coarse simplification as the optimal temperature for photosynthesis vary greatly across plant species, as explained in Chapter 2.2.1.

The total flux of ozone from the air to the surface is calculated by multiplying the models bottom layer ozone concentration by the total deposition velocity (conductance), scaled by the ratio of the stomatal conductance to that of the total surface conductance (or the total surface resistance to the stomatal resistance). The resulting stomatal flux over the May-period is compared to the stomatal flux derived from measurements in Figure 4-8.

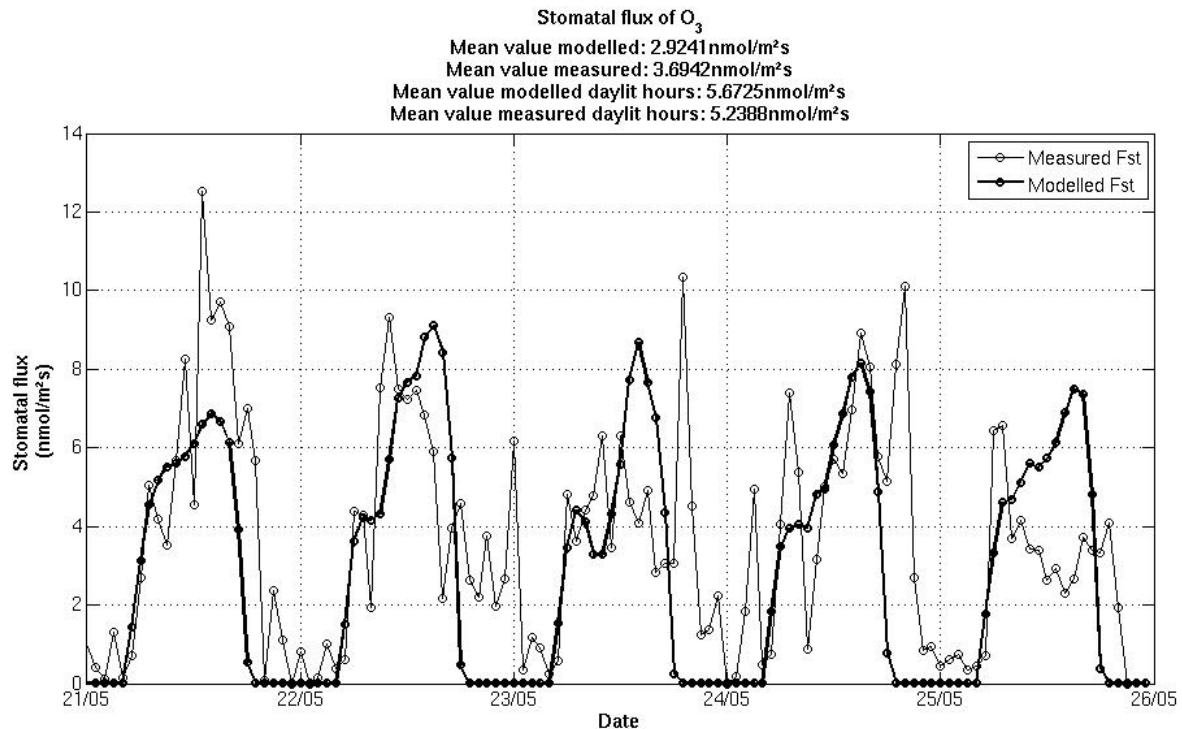


Figure 4-8: Stomatal flux modelled (thick line), and derived from measurements (thin line) in the period May 21-26. Average modelled value for daylight hours is $5.67 \text{ nmol m}^{-2}\text{s}^{-1}$, the average value derived from measurements during daylight hours is $5.24 \text{ nmol m}^{-2}\text{s}^{-1}$.

The stomatal flux derived from measurements shows a highly irregular pattern as a result to its link to the atmospheric turbulence. The eddy covariance method is efficient when turbulence is high, but not as reliable during night. According to recommendation from Dr. Gerosa, we chose to only compare the modelled results with data measured in the time between 8a.m. to 7p.m, local time. Comparing the average measured and modelled flux from this timeperiod only, result in a modelled mean value of $5.7 \text{ nmol m}^{-2}\text{s}^{-1}$, to the average value derived from measurements during daylight hours of $5.2 \text{ nmol m}^{-2}\text{s}^{-1}$.

Within this selected dataset there are some uncertainties; a signaling error on the afternoon of May 23 is leading to an unphysical peak in the stomatal flux. The late afternoon peak on May 24 and on May 25 are linked to air advection from a different sector of high pollution, but might also be due to field campaign personel working under the measuring tower, stirring up turbulence detected by the instruments. As the site was also very humid, dew on the canopies in the early morning could lead to an overestimation of the evapotranspiration, from which the stomatal flux is derived, resulting in an overestimation of the stomatal flux in the early morning hours.

The modelled fluxes show a more even curve, and due to the stomatal conductance reflecting a closed stomata during the night, the flux is zero during the night-time. The first day, May 21, show a significantly lower mid-day flux than the measured one. As the conductance is high, the low flux is due to the already discussed underestimation of the ozone concentration. On May 23, the flux decreases at 11-12 a.m., reflecting the fall-off in conductance as seen in Figure 4-7. This decrease is associated with high surface temperature as can be seen in Figure 4-9 below.

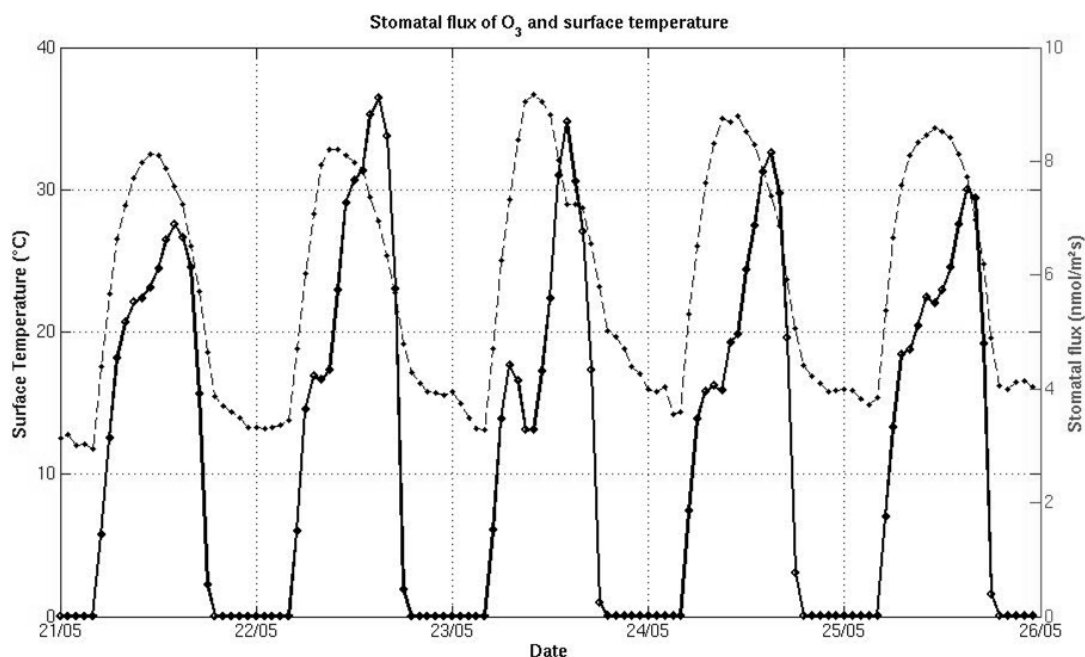


Figure 4-9: Modelled stomatal flux (thick line, right axis) and surface temperature (thin line, left axis) for the period May 21-26. The stomatal conductance “cut-off-temperature” is 40 °C, not reached on any of the days within this period.

The fall in measured flux during the afternoon on May 26, might be related to the lower measured ozone concentration at the same time. A second possibility might be that the evapotranspiration is low due to water stress in the form of low soil water content and/or high vapour pressure deficit, effects which are not captured by the model. The average diurnal variation of stomatal flux derived from measurements and from the model simulation for the selected May-period is shown in Figure 4-10 below.

The measurements show an on average higher flux in the early morning hours, possibly due to overestimation because of dew, and in the late afternoon, possibly in part as a result of error measurements and night-time disturbances. The correlation between the measured average and modelled for the daylight hours between 8a.m. and 7p.m. local time is of 0.75.

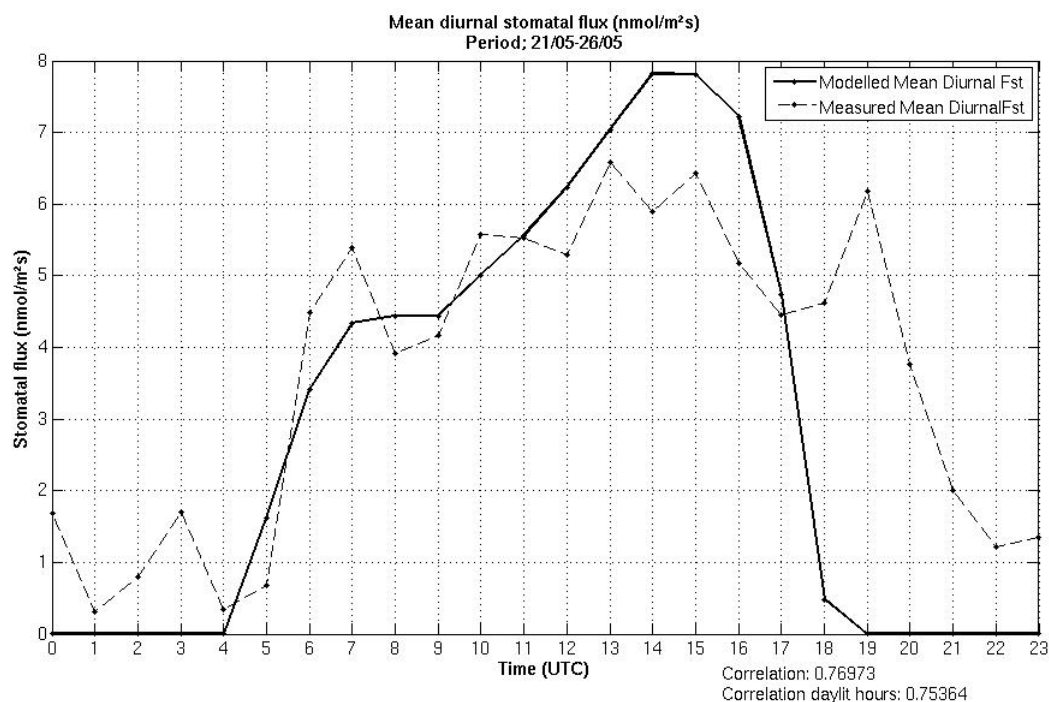


Figure 4-10: Average diurnal variation of stomatal flux over the period May 21-26. Modelled (thick line) and derived from measurements (thin line). The correlation coefficient is 0,77. Correlation coefficient for only daylight hours is 0.75.

June 23-28

The June period is part of the “summer period” as described in G09a, characterized by lower water availability resulting in lower evapotranspiration and stomatal fluxes compared to the spring period. The temperature average over the period was 24.4°C. No precipitation was

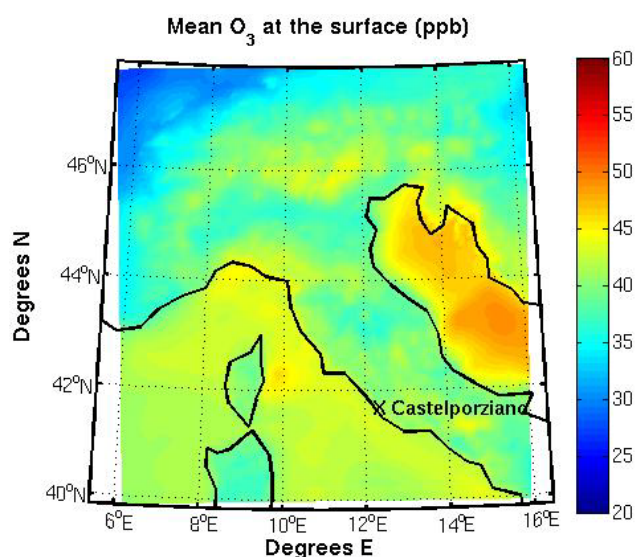


Figure 4-11: Average ozone mixing ratio for the model bottom layer over the June-period (ppb).

recorded over the period. The average ozone concentration over the summer period was 38.6ppb, slightly higher compared to the spring period. The selected five days of June 23-28 show a somewhat higher average value of 43.3ppb, compared to the total summer period. The modelled mean value over the June five-day period is 40.9ppb, and like in the May-period the modelled mean is a bit lower than the measured one. The variability of the measured data is lower for this period, with a maximum value of 68.43ppb and a bottom measured value of 5.4ppb.

The measured ozone mixing ratio over the

period is presented in Figure 4-12, together with the modelled bottom layer ozone concentration and the scaled reference-height concentration.

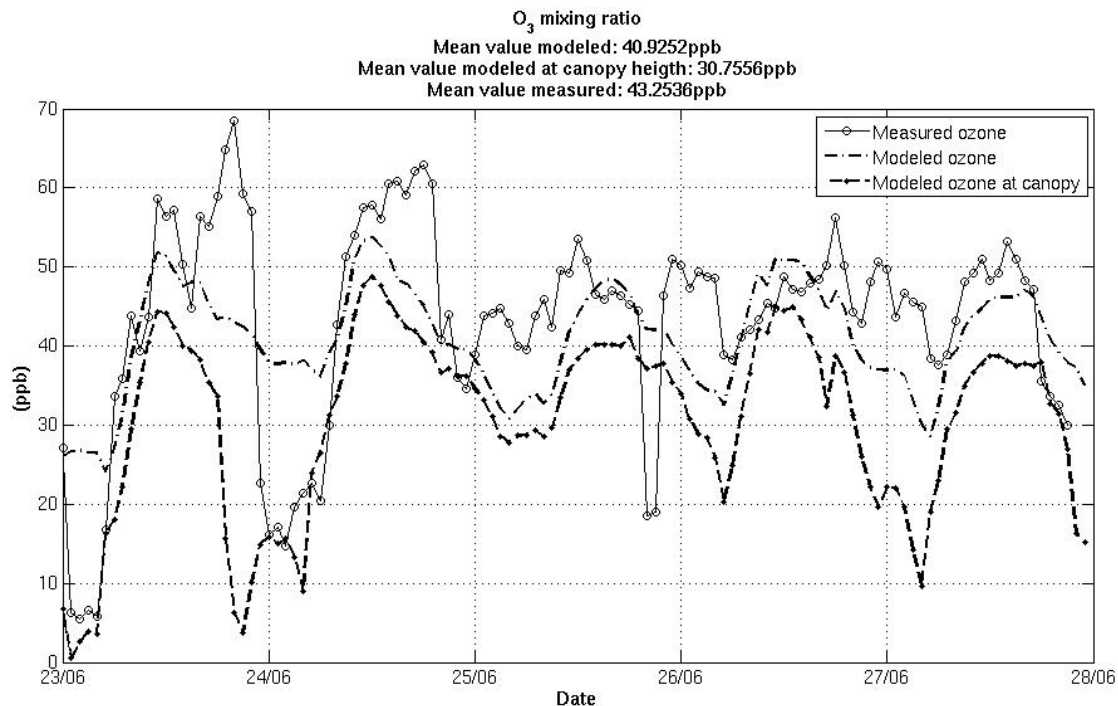


Figure 4-12: Ozone mixing ratios from measurements (thin line) and modelled (thick line) for the period June 23-28. The average value for the modelled bottom layer mixing ratio over the period is 40.9 ppb, and average measured mixing ratio is 43, 3 ppb. The modelled reference-height average is 30.8ppb

The first two days of this period show a similar pattern as to the May-period, with high measured ozone values during the day and very low values at night. From the windplot of the period in Figure 4-13, we see that the rest of the June-period was not characterized by the regular breeze-regime as the first period, and does not show the same distinct diurnal variability in measured ozone concentrations. The measured day-time values do not reach the same values, and are fairly well estimated by the model. The night-time values are not as low, and underestimated by the scaled model concentration.

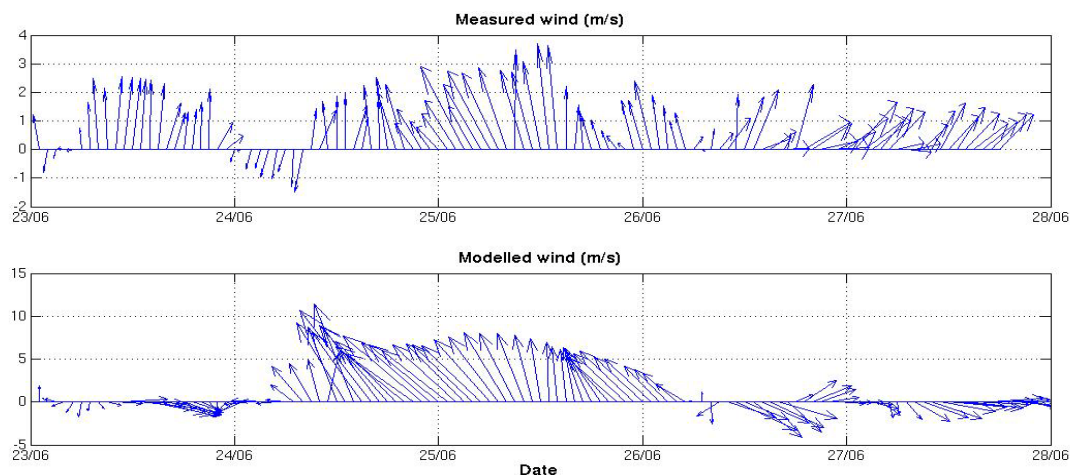


Figure 4-13: Measured wind speed and direction (top panel) and modelled wind speed and direction at 10m height (bottom panel), over the period June 23-28.

The mean diurnal concentration over the period is presented in Figure 4-14, and shows a considerably lower measured mean day-time maximum value compared to the May-period, of 52.9ppb to 75.4ppb, respectively. On average the night-time values are higher, and the correlation with the modelled ozone concentration for the bottom model layer is 0.95.

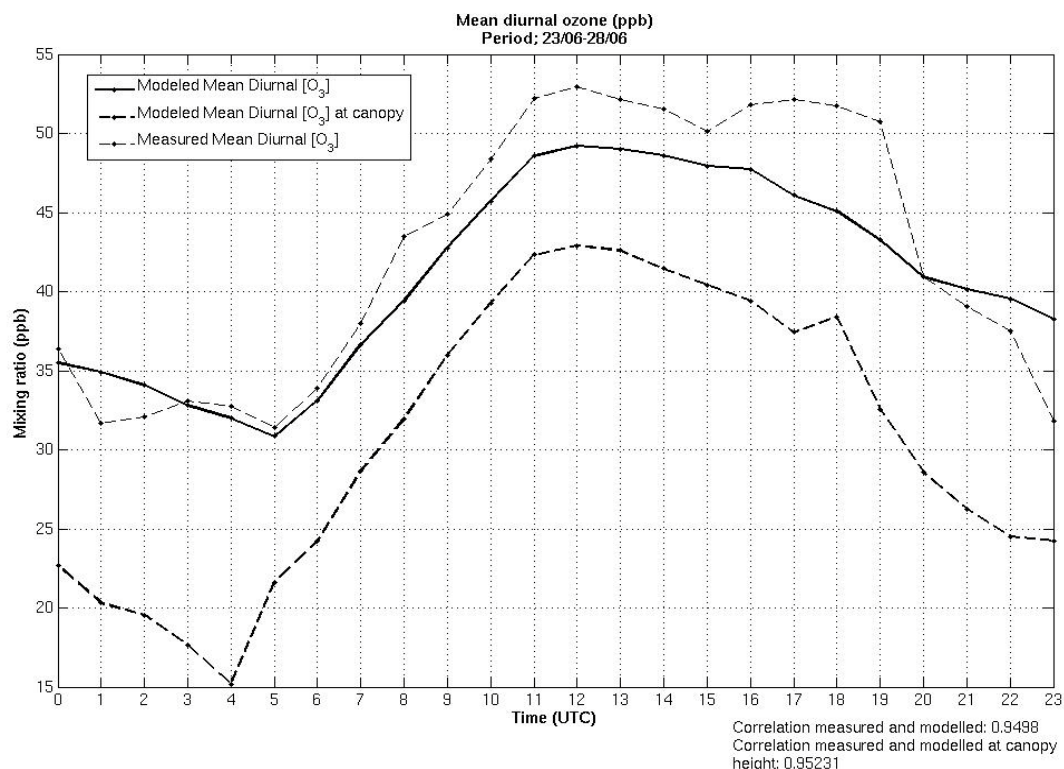


Figure 4-14: Average diurnal variation of ozone mixing ratios (ppb) over the period June 23-28. Modelled (thick line) and modelled derived from measurements (thin line), and the scaled ozone concentration at reference height (stippled line). The correlation coefficient is 0, 95 between the measured and the modelled bottom layer average, and the same (to two decimal round off) for the scaled concentration.

The stomatal conductances in Figure 4-15 show a different typical pattern this period, with an increased and more frequent mid-day decrease, as before due to high surface temperature in the middle of the day, as shown in Figure 4-17. The conductance is in general lower in this period, only on the last day reaching values exceeding 0.8 cm/s, which is exceeded every day of the May-period.

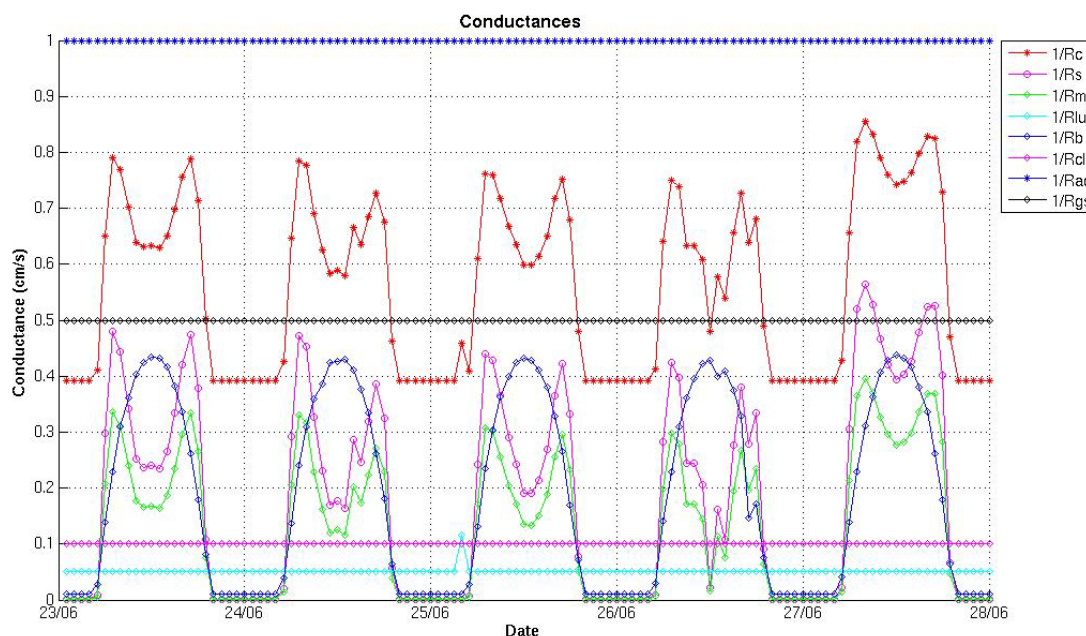


Figure 4-15: Total surface conductance and the seven conductances it consists of for the period June 23-28. (R_s = stomatal resistance, R_m =combined stomatal and mesophyll resistance, R_{lu} = upper bulk canopy and healthy leaf cuticular resistance, R_b = resistance due to buoyancy within the canopy, R_{cl} = lower canopy cuticular resistance, R_{ac} = resistance due to air transfer within the canopy, R_{gs} = resistance of soil and ground litter)

The conductances of the parallel pathways show that the stomatal conductance for this period is also on average slightly lower in this period than in the May-period. As the incoming shortwave radiation shows no big differences, the temperature dependence is probably the main reason.

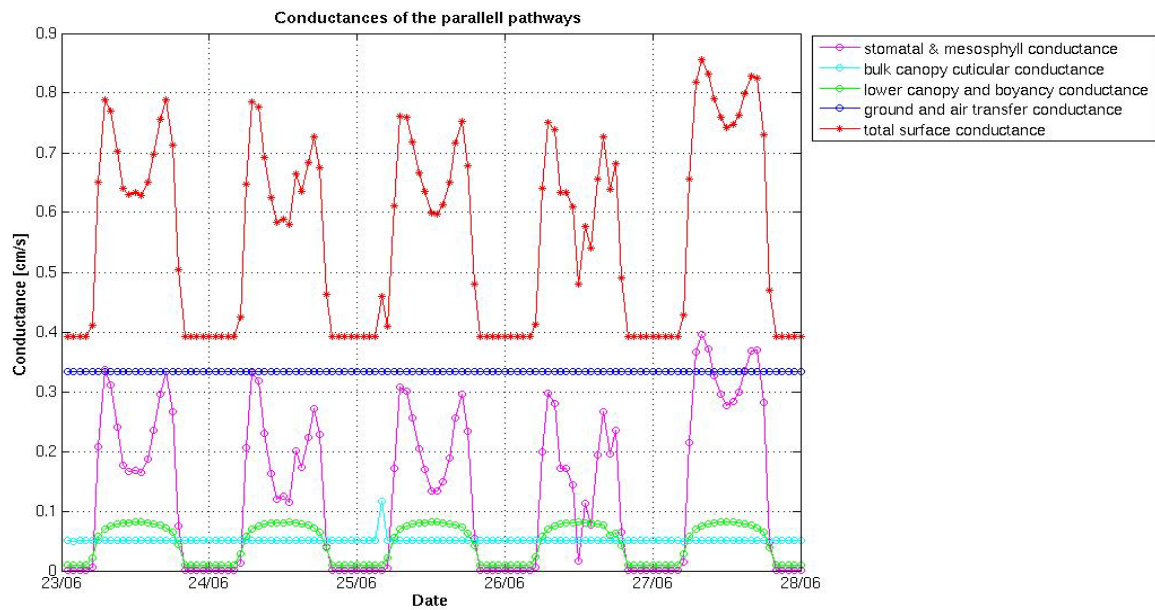


Figure 4-16: The total surface conductance and the conductance of the four parallel pathways it consists of.

The modelled flux and surface temperature can be seen in Figure 4-17. It is clear from this figure that the modelled temperature is in general higher in this period than in the May-period, with an average of 27.1°C, where the day-time temperature reaches high enough to cause the stomatal conductance, hence the flux to dip a bit lower during the middle of the day. The surface temperature almost reaches the cut-off temperature of 40°C (39.7°C) on mid-day May 26th, causing the conductance, hence the flux to steep.

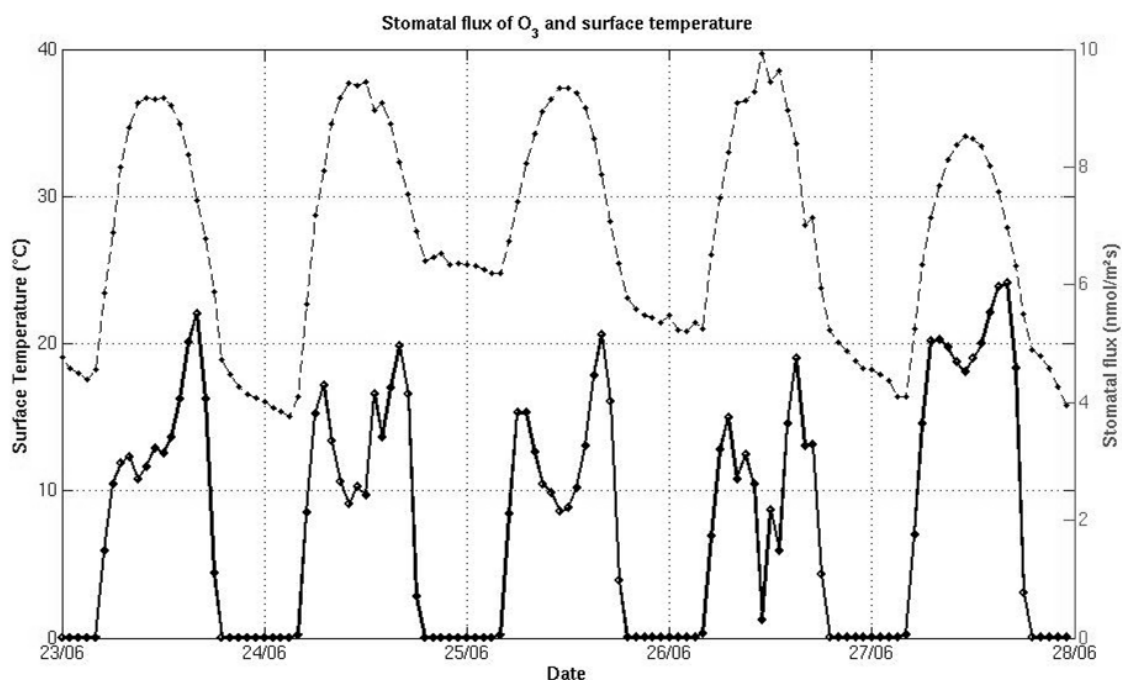


Figure 4-17: Modelled stomatal flux (thick line, right axis) and surface temperature (thin line, left axis) for the period June 23-28. The stomatal conductance “cut-off-temperature” is 40 °C.

The measured and the modelled flux over the June-period are shown in Figure 4-18. The measured fluxes has no suspiciously high peaks in this last period, except the peak on June 26, late in the evening, which can be considered due to some disturbance.

The measured stomatal fluxes decreased in their diurnal mean by 44% in the total summer period compared to the spring period according to G09a. This decrease from spring to summer is also reflected in the five day periods selected, where the measured mean value for the day lit hours of the June-period is $1.98 \text{ nmol m}^{-2} \text{ s}^{-1}$, only 38% of the May-period average value of $5.24 \text{ nmol m}^{-2} \text{ s}^{-1}$. The modelled average value for the day lit hours over this period is $3.64 \text{ nmol m}^{-2} \text{ s}^{-1}$, 64% of the May-period average value.

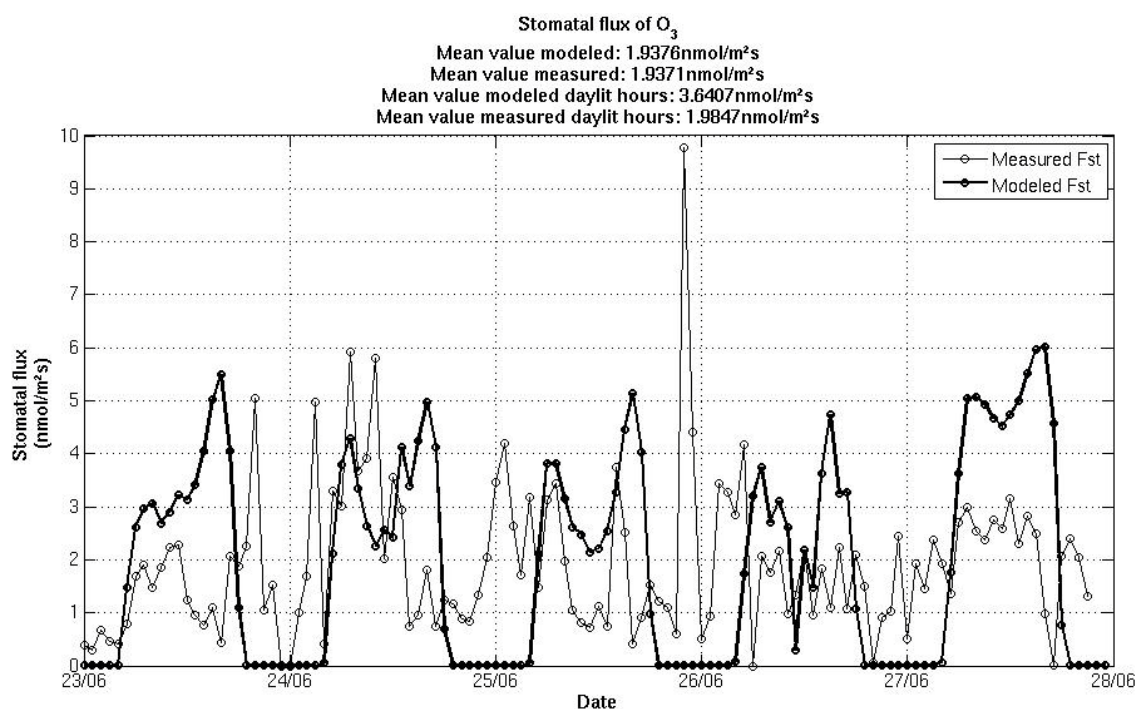


Figure 4-18: Stomatal flux modelled (thick line), and derived from measurements (thin line) in the period June 23-28. The average value derived from WRF is 1.94 nmol/m²s and the average flux derived from measurements is 1.94 nmol/m²s. The average value for day lit hours derived from WRF is 3.6 nmol/m²s and the average flux derived from measurements is 2.0 nmol/m²s.

The general diurnal trend of this period can be seen in Figure 4-19. For the measured stomatal flux, the trend was increasing flux until about 7 a.m. (9 a.m. local time), and then a slight decrease towards the evening. The modelled diurnal mean variation is however very different, with a sharp increase in flux in the morning, then a pronounced decrease in the mid-day hours, followed by an increase in the afternoon before falling off towards the evening. The correlation of the mean measured day lit hours flux and the modelled day lit hours is not surprisingly as low as -0.37.

In G09a the decreased stomatal flux during the summer period is due to water stress. The summer period was generally dryer, with a shallower soil water table, making the ecosystem more vulnerable to the evaporative power of the atmosphere, and causing the evapotranspiration to decrease by more than 60% in the central day lit hours of the summer period, compared to the spring period (G09a).

The limiting factors of water stress are not specifically accounted for in the WRF-Chem dry deposition scheme. The stomata are predicted to close at high temperatures, as seen in the temperature plots of the two periods, but will according to this parameterization re-open as the temperature increases towards the evening. However, if the ecosystem does not acquire enough water during these warm hours, the stomata are not likely to re-open in the afternoon, according to Pleijel et al. (2007) (see Section 2.2.3 page 38).

In the following the two different parameterizations for the limiting effect of the atmospheric water vapour pressure deficit on the stomatal flux, as described in the Jarvis approach to calculate stomatal conductance (Section 2.2.3), are applied to the modelled results.

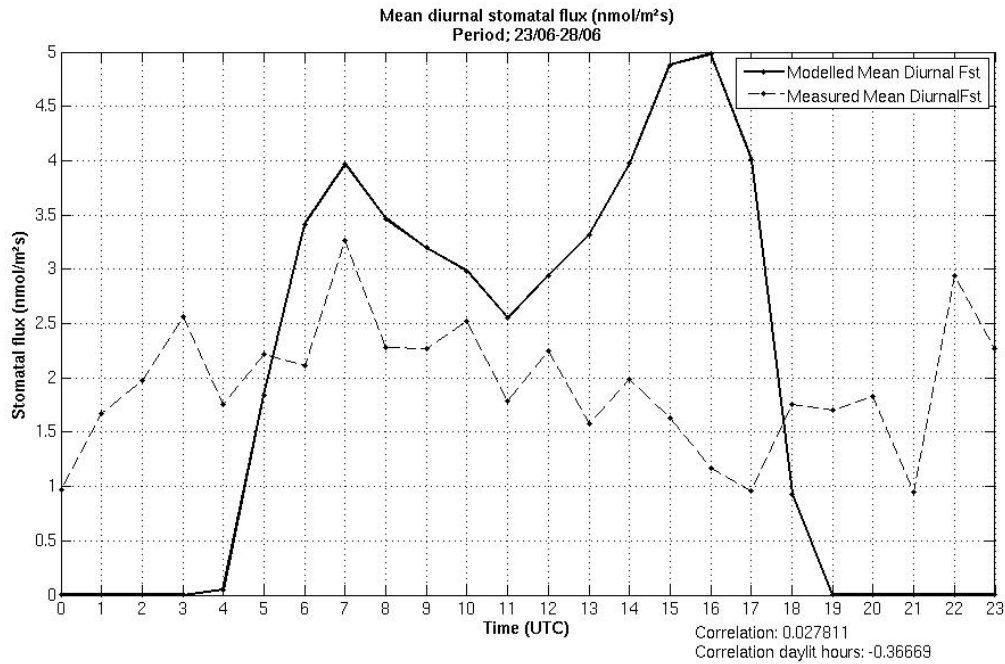


Figure 4-19: Average diurnal variation of stomatal flux over the period June 23-28. Modelled (thick line) and derived from measurements (thin line). The correlation coefficient is 0,03. The correlation coefficient for only the daytime hours is -0.37.

4.1.1 Vapour Pressure Deficit limitations

The water pressure deficit (VPD) has been calculated from the available model parameters. The VPD can be expressed as the difference between the saturation water vapour pressure at temperature T , and the actual water vapour pressure of the air, e_a

$$VPD = e_{sat}(T) - e_a$$

(4-2)

where e_{sat} is the water vapour saturation pressure at the temperature T , where T is expressed as the mean of the surface temperature and the air temperature at 2 m above ground, and e_a is the actual water vapor pressure of the air. According to Bolton (1980) the water saturation pressure for a temperature T can be fitted to within 0.1% over the temperature range $-30^\circ\text{C} \leq T \leq 35^\circ\text{C}$ by the empirical formula 4-3. For a temperature of 40°C the formula result is within 0.2% of the value for e_s at the given temperature found by Wexler (1976).

$$e_{sat}(T) = 6.112 \exp\left(\frac{17.67 T}{T + 243.5}\right)$$

(4-3)

The actual water vapour pressure of the air is according to Wallace et al.(2006) given as

$$e_a = \frac{w}{(w + \varepsilon)} p$$

(4-4)

Where w is the water vapor mixing ratio, p is the pressure and ε is the ratio of the gas constant for 1kg dry air to that of 1kg water vapor, $R_d/R_v = 0.622$.

The VPD function

The VPD function used here is the same one as derived from open top measurements in the Po Valley in the northern part of Italy by Gerosa et al. (2008), for the moderately ozone-sensitive tree *Fagus Sylvatica* (European Beech), given as

$$f_{VPD} = \frac{(1 - 0.1)(c - VPD)}{c - d} + 0.1$$

(4-5)

where c represents the value of VPD where the influence on the conductance reaches its highest value, and d is the VPD value above which the conductance begins to suffer limitations. As long as the VPD is lower than d , the VPD-function has no effect on the conductance, and if the VPD exceeds the value of c , the VPD-function is set to the value of 0.1, implementing the maximum limitation to the conductance. The values for c and d are species-specific. Due to limited observational data for these values for the species dominating the Maquis ecosystem, the values for *Fagus Sylvatica* are adopted for the purpose of this study, and the values of 4.0kPa and 1.8kPa are used for c and d , respectively.

Applying the same function constants derived for this specific species on an entire ecosystem is a crude approximation, but may nevertheless give some indication of how the VPD affects the modelled conductances and fluxes.

The VPD function's effect on the stomatal conductance for the May period and the June period is shown in the top panels of Figure 4-20, a. and b., respectively. The limiting effect of the VPD function has the greatest impact during the mid-day hours, amplifying the effect of the temperature-dependence on the conductance, by increasing the mid-day depression. For the June period, which is part of the dry summer-period, the effect of the VPD function is increased, and affecting a greater part of the day, reducing the daily conductance significantly. The same pattern is recognized in the stomatal flux (bottom panels), which is reduced somewhat during the mid-day hours of the May-period, from an average of $5.7 \text{ nmol m}^{-2} \text{ s}^{-1}$ to $5.0 \text{ nmol m}^{-2} \text{ s}^{-1}$, and to a greater extent in the June-period, from an average value of $1.9 \text{ nmol m}^{-2} \text{ s}^{-1}$ to $1.3 \text{ nmol m}^{-2} \text{ s}^{-1}$ for the day lit hours.

The middle panels show the f_{VPD} as a function of the calculated VPD. The modelled hourly values for the conductance over the five day period are plotted with and without the limitation of the VPD-function.

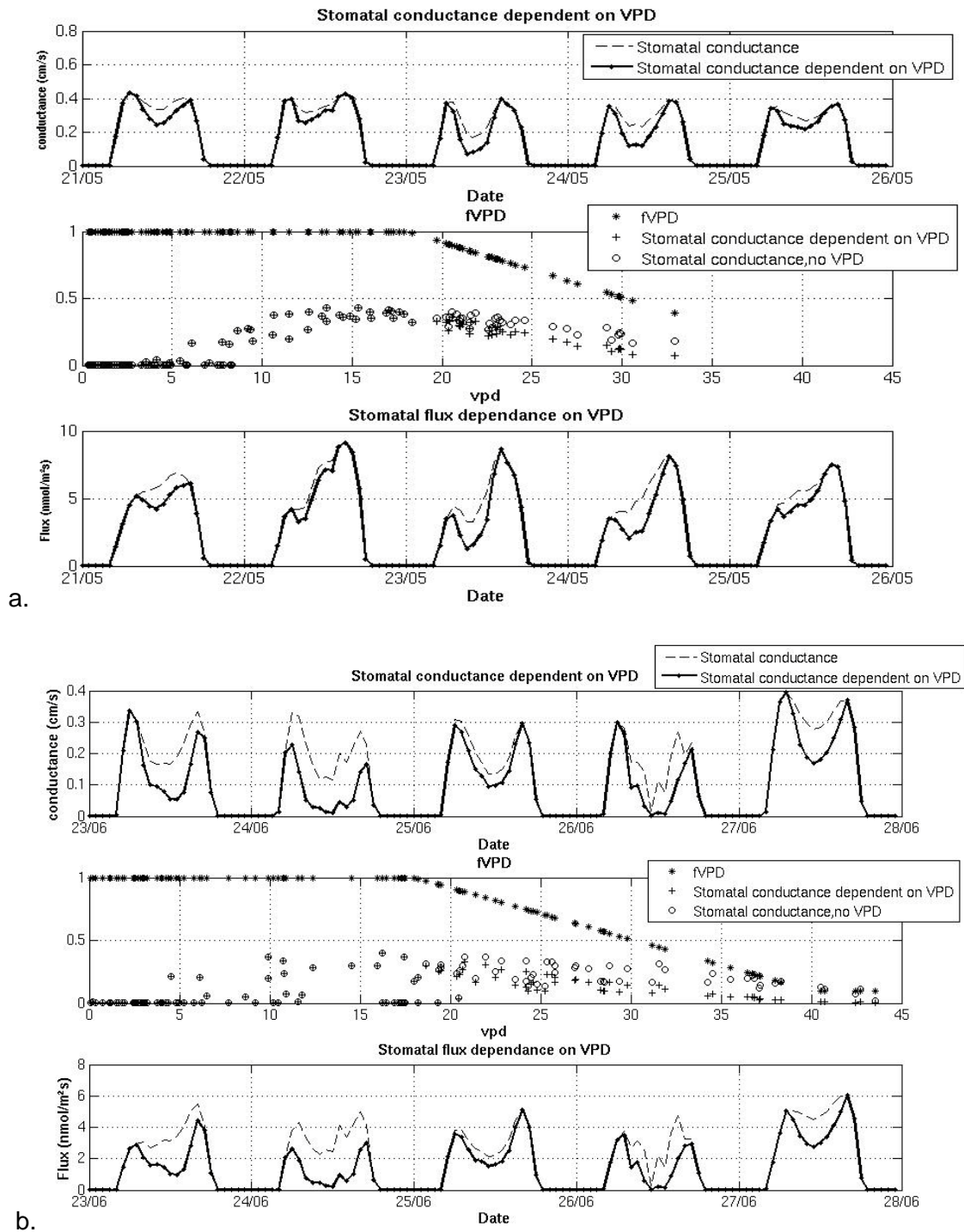


Figure 4-20: The influence of the VPD-function for the May-period (a.) and the June period (b). The top panels show the limiting effect of the VPD function on stomatal conductance, the middle panel show the f_{VPD} as a function of the calculated VPD (*), and the hourly modelled values for the stomatal conductance with (+), and without (o) the VPD function limitation. Bottom panels show the modelled flux with (thick line), and without VPD function limitations.

The sum VPD function ($\sum VPD$)

The sum VPD function applied to the modelled data is the same as the one used by e.g. Pleijel et al. (2007), described in Chapter 2.2.3, on page 38. In Pleijel et al. (2007), the critical value for the accumulated VPD is set to 8 kPa for wheat, and 10 kPa for potato. Based on the hypothesis that the general vegetation in the Mediterranean Maquis ecosystem does endure a greater deal of water stress before the stomatal opening is affected, a somewhat arbitrary critical value of 12 kPa has been applied for the purpose of this study. The VPD is accumulated over the sun lit hours.

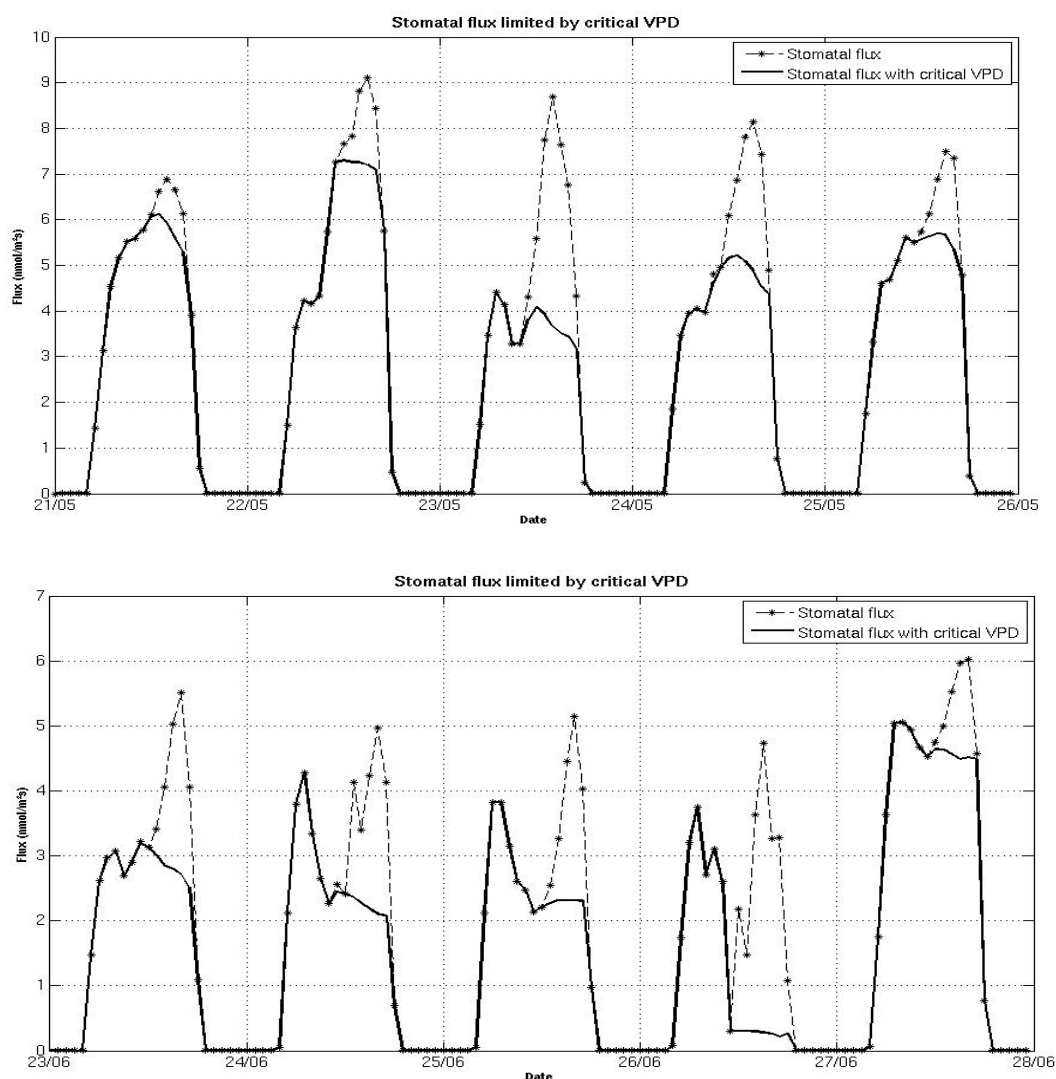


Figure 4-21: Modelled flux (thin line) and modelled flux limited by the sum VPD function with critical value 12kPa (thick line) for May 21-26 (top panel) and June 22-28 (bottom panel).

The effect of the VPD sum function on the stomatal flux of the May-period is displayed in Figure 4-21, top panel. The critical value is reached every day in this period, limiting the afternoon fluxes. The warmer and dryer days are especially effected, as the sum VPD function is blocking the conductance from rising again after the temperature dependence of the conductance is causing it to steep during the mid-day hours.

The implementation of the sum VPD function has a more pronounced effect on the June-period, as seen in the bottom panel of Figure 4-21, efficiently cutting the modelled afternoon peak of every day in the period. The result is a very different mean diurnal variation over the period, as shown in Figure 4-22.

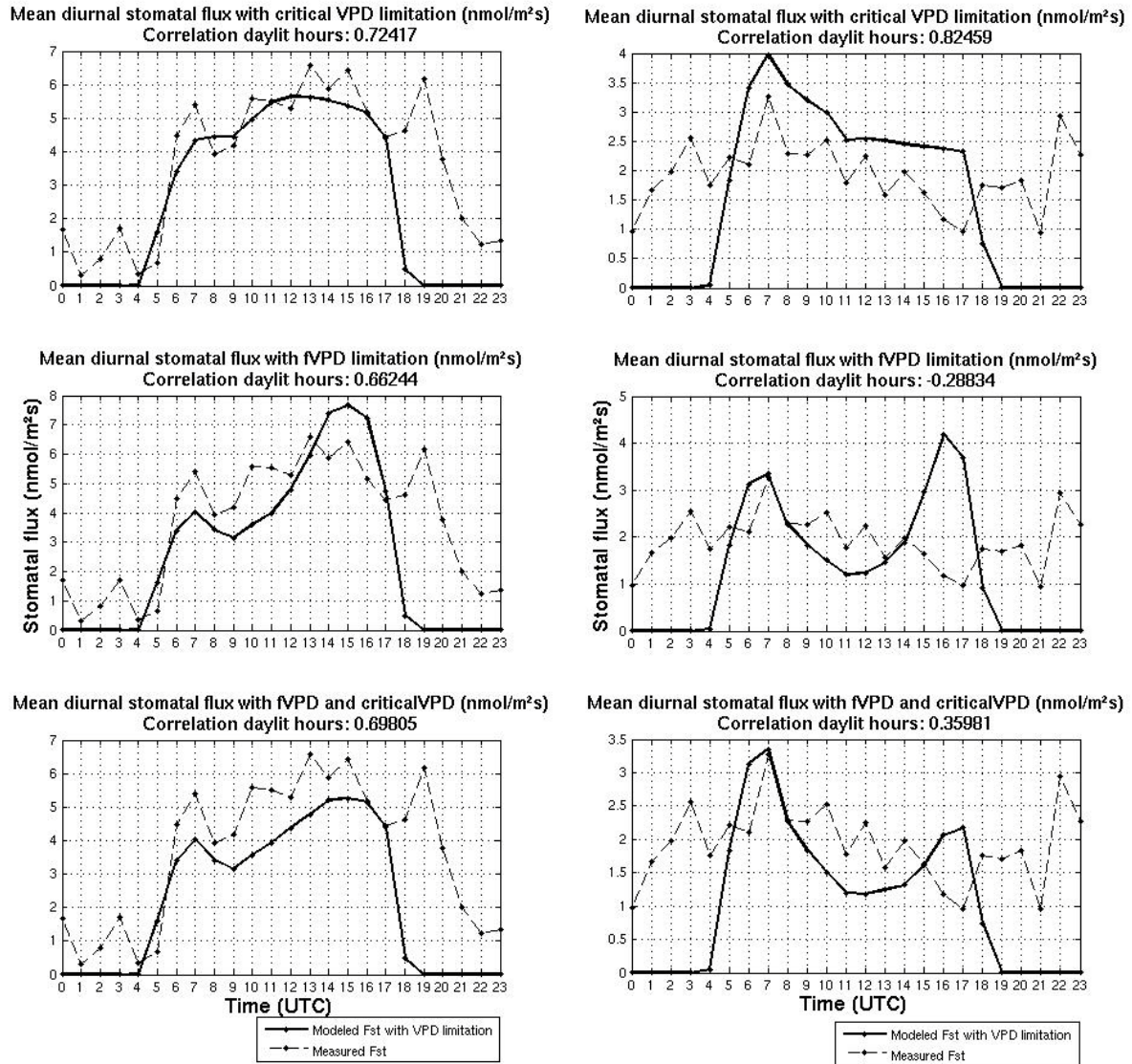


Figure 4-22: Mean diurnal flux limited by VPD functions for May period (left) and June period (right). The top panels show mean diurnal flux limited by the VPD critical sum function, with the critical sum being 12kPa, compared to the average diurnal flux derived from measurements. Middle panels show diurnal flux limited by the f_{VPD} function from Gerosa et al. (2008), compared to the average diurnal flux derived from measurements. The bottom panels show the flux limited by both the VPD critical sum function and the f_{VPD} function compared to the average diurnal flux derived from measurements.

The top panels of Figure 4-22 show the diurnal mean flux derived from measurements for each of the periods, together with the modelled diurnal mean with the critical sum VPD function limitation. The result of applying the critical sum function to the May period, shown in the left panel, is a more bell-shaped diurnal mean, somewhat underestimating the afternoon flux, compared to the measured flux. The correlation for the day lit hours is in this case

reduced from 0.75 to 0.72. Apparently the 12kPa critical value is overestimating the limiting effect of the VPD somewhat during this period.

The result of applying the critical sum function to the June period is shown in the right top panel. The curve of the average diurnal flux has substantially changed form, and the afternoon peak is replaced with a slightly decreasing afternoon flux, clearly more in line with the measured diurnal mean. The correlation for the day lit hours for this period is increased from -0.37 to 0.82 by applying the VPD sum function.

The middle panels in Figure 4-22 show the effect of the f_{VPD} function on the mean diurnal flux of each period. For both periods the mid-day decrease in stomatal flux is increased as a result of applying the f_{VPD} -function, resulting in a slight decrease in the correlation of the day lit hours for the May-period, and a slight improvement of the correlation in the June period, but still negative.

The bottom two panels of Figure 4-22 show the mean diurnal fluxes of the two periods after applying both of the VPD limiting functions described, by multiplying the f_{VPD} function by the stomatal conductance derived by applying the sum -VPD function. The correlation of the May period is slightly decreased by the application of the combined VPD-functions and the result for the June period is an increase in correlation, mostly due to the sum-VPD-function.

Table 4-1: Calculated correlation coefficient for the mean modelled fluxes limited by VPD functions, to the average flux values derived from measurements, for day lit hours.

Limited by	May 21-26 (only day lit hours) Correlation coefficient	June 23-28 (only day lit hours) Correlation coefficient
No limitations	0.75	-0.37
sum VPD function ($\sum VPD$)	0.72	0.82
VPD function (f_{VPD})	0,66	-0.29
sum VPD function ($\sum VPD$) and VPD function (f_{VPD})	0,70	0,53

It is clear from Table 4-1 that the modelled flux without any VPD limiting factors is what gives the best result for the not so dry May-period, while applying the sum-VPD function to the dry June-period results in a great improvement of the correlation to the stomatal flux derived from measurements.

4.2 Southern Africa

The results from the seven-month long simulation of the Southern African domain are presented in this chapter. The results of the modelled ozone concentrations are compared to the ones modelled by Zunckel, et al. (2006). The mean stomatal fluxes for each of the months are presented, and the accumulated dose of ozone to the vegetation is computed, first over the full 7 months modelled and then over a typical maize growing season of 4 months (120days).

Based on the findings of the previous chapter, the sum-VPD function is applied to the stomatal conductance to estimate the limiting effect on the accumulated dose to the vegetation over both the 4- and 7-month accumulative periods.

The Southern African domain is covered by 19 of the total 24 USGS landuse-categories. The domain and its landuse-categories are presented in Figure 4-23. The entire northern part of the domain is dominated by the category of “savannah”, and “broad leaf forest”, with some parts of different cropland categories. As mentioned in Chapter 3.4, the various cropland-categories are grouped together by the Wesely dry deposition scheme (see Table 3-3 on page 48). The southern part of the domain is characterized by vast areas within the categories grassland or shrub land, and also various cropland-categories. The south-western part also has large areas of desert, categorized as barren/sparsely vegetated.

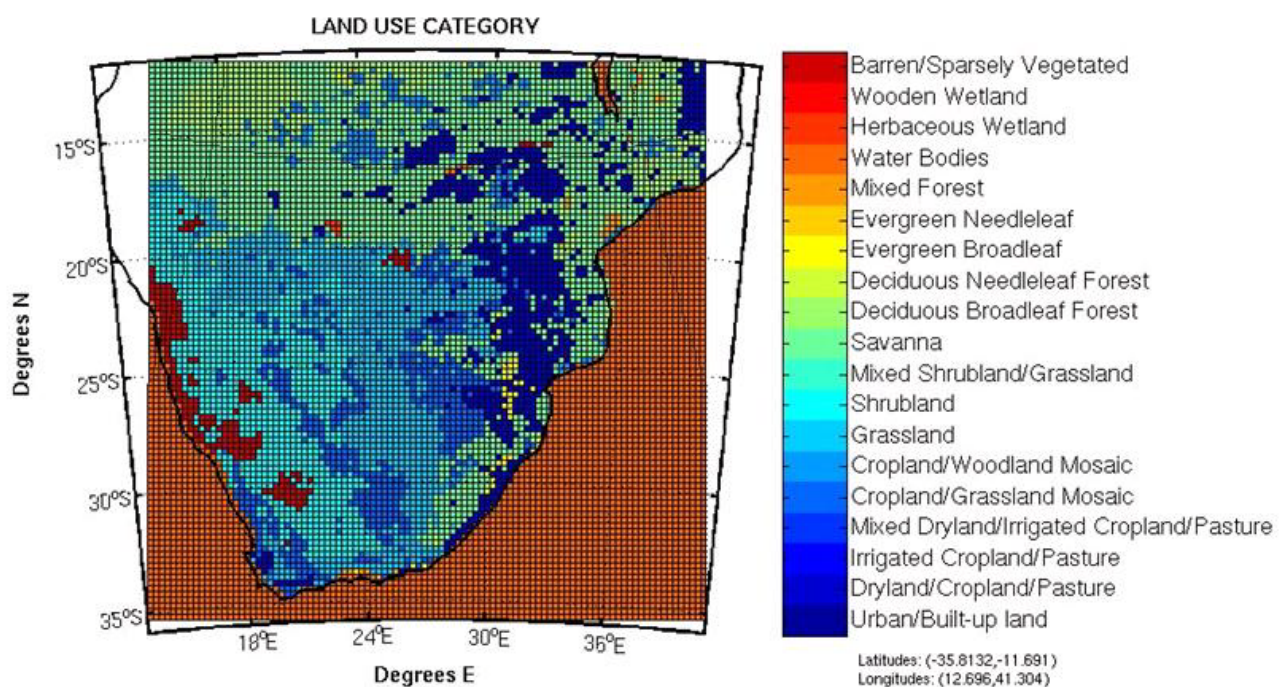
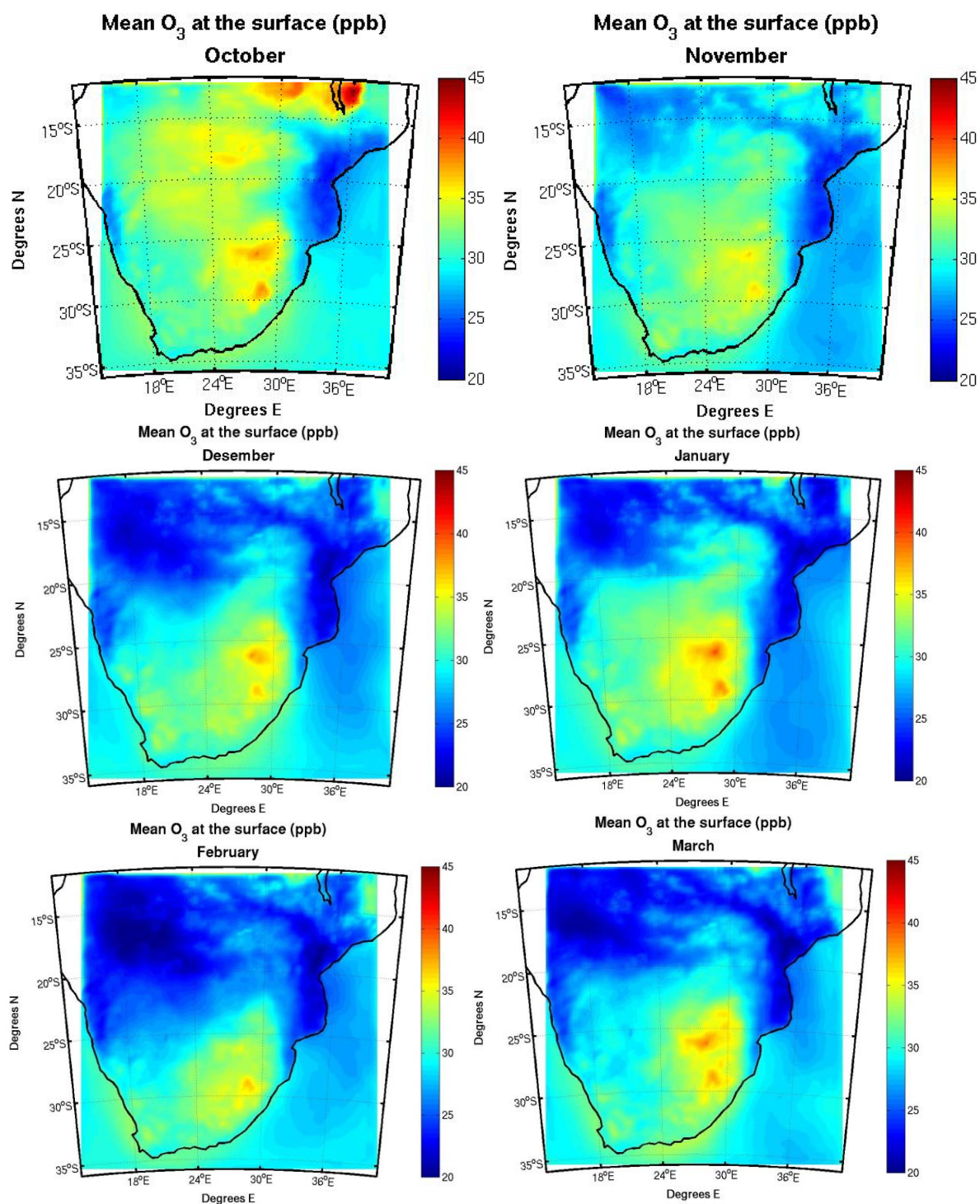


Figure 4-23: The Southern African domain with the 24 USGS landuse categories.



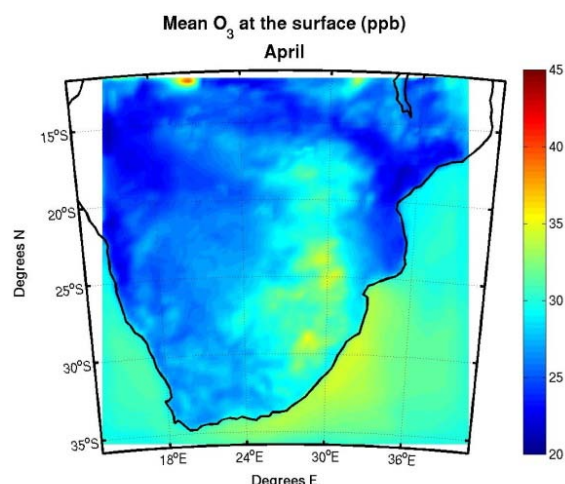


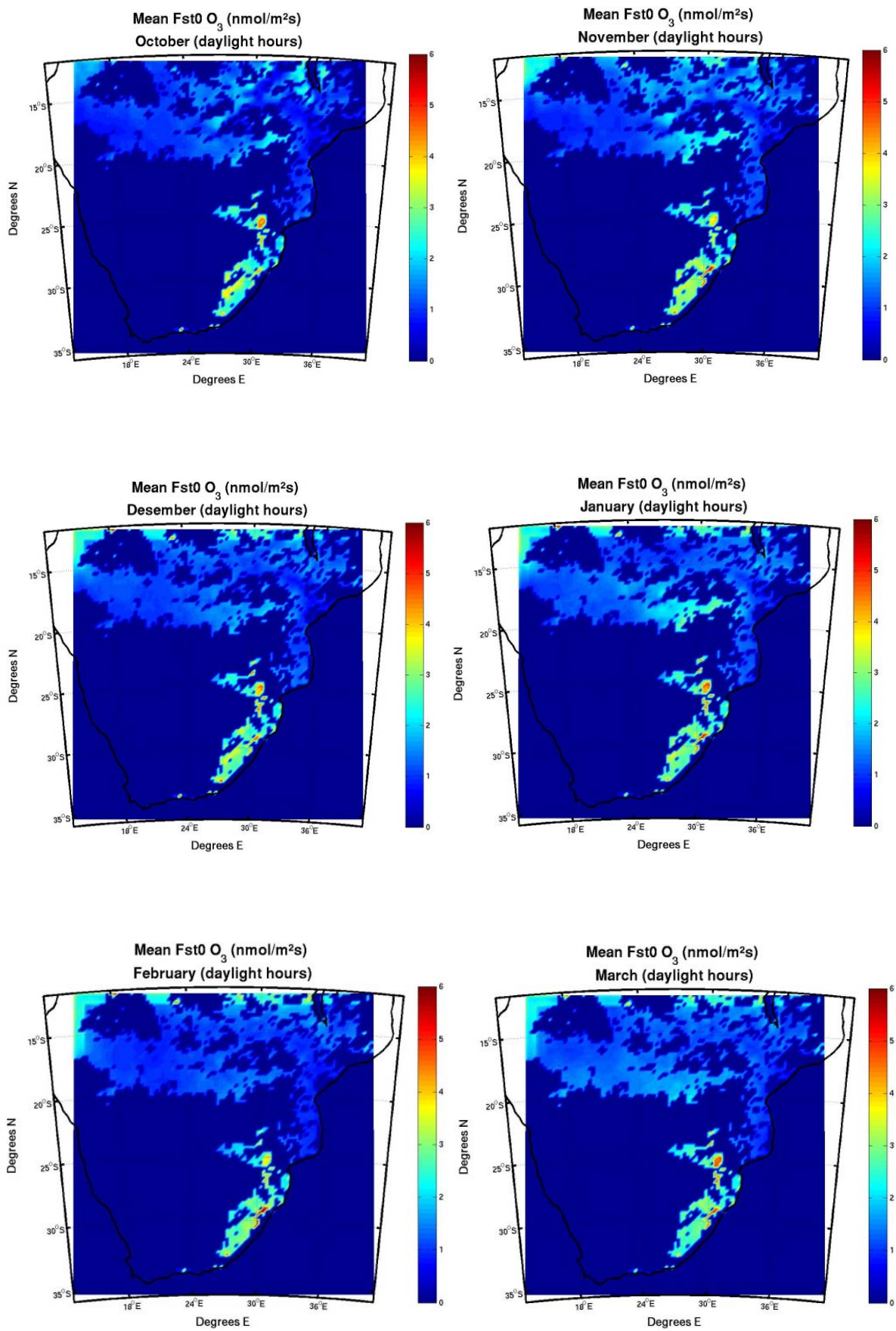
Figure 4-24: Mean modelled bottom layer ozone mixing ratios over each month from October 2000 through April 2001. All mixing ratios are given in ppb.

The average ozone mixing ratios of the model bottom layer for each of the seven months are presented in Figure 4-24. The average ozone concentrations over the whole domain are within the range of 27-32 ppb, with October being the month with the highest domain average of 31.3 ppb. October is characterized by high ozone concentrations east of Lake Malawi, and the peak value within the month exceeds 100 ppb (see Table 4-2). The maximum mean value of the domain is 44.7 ppb. The high concentrations over just this period are due to high emissions which can possibly be associated with biomass burning for farming purposes, or from a wild forest fire. For all of the other months, the South African Highveld and the surrounding areas are associated with the highest ozone concentrations of the domain, reaching the highest average concentrations in January 2001 with a maximum mean concentration of 40.4ppb. The modelled values for the monthly mean ranges from 19,8 ppb to 44,7 ppb, and are close to, but slightly lower than those modelled by Zunckel et al. (2006), where the range was 20-50 ppb, modelling only 5 days of each month. The average monthly maximum, mean, minimum and peak values for each of the modelled months are given in Table 4-2.

Month	Maximum average value (ppb)	Mean value (ppb)	Minimum average value (ppb)	Peak value during period (ppb)
October	44,65	31,29	22,92	100,68
November	37,15	29,37	23,16	71,22
December	38,47	28,02	20,69	69,84
January	40,44	28,49	20,73	71,42
February	37,02	27,33	19,79	70,59
March	38,99	27,95	19,88	73,36
April	39,73	28,07	20,86	84,21

Table 4-2: Monthly peak and domain mean values for the modelled bottom layer ozone concentration.

The average flux per month over the period is shown in Figure 4-25. Since the flux distributions show no pronounced similarity with the averaged distribution in ozone concentrations in any of the months, it is clear that the average flux of ozone into the vegetation is strongly dependent on the conductance, which depends on the land-use category.



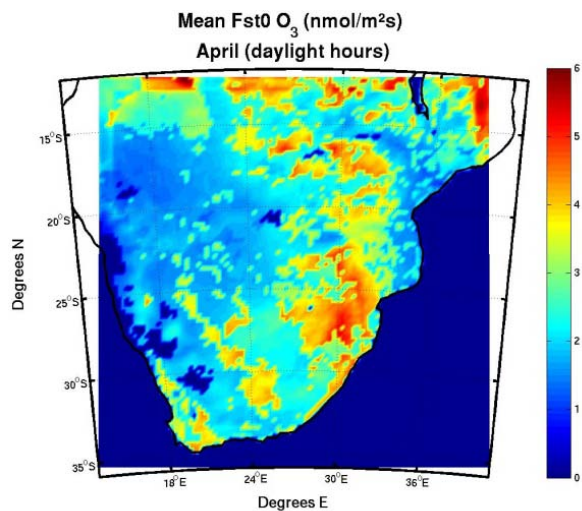


Figure 4-25: Monthly average stomatal flux over the Southern African domain. All fluxes are given in nmol/m²s.

The stomatal conductance's dependency on the seasonal category is clearly displayed in the April-plot. The seasonal category changes from March to April, from the category "midsummer with lush vegetation" to "autumn with unharvested cropland", causing the stomatal conductance to rise across almost all landuse-categories. The change in season is reducing the minimum stomatal resistance r_i (see Equation 3-25 on page 55), yielding a higher stomatal conductance over this period. Comparing the first six panels with the map over the landuse categories in Figure 4-23, we see that the categories "savannah" and "evergreen broadleaf forest" are the ones receiving the highest fluxes of ozone for the first six months. For the April-plot on the other hand, the mean stomatal flux is more evenly distributed over all landuse categories, including the cropland-categories, but still excluding the sparsely vegetated landuse categories. The abrupt change in deposition season might be considered a coarse simplification, as its consequences are significant. The ozone concentration for April is seemingly not much affected by the rise in stomatal conductance.

Another factor possibly affecting the increased flux over the April period is a considerably lower mean surface temperature compared to the other modelled months, represented by December in Figure 4-26 below.

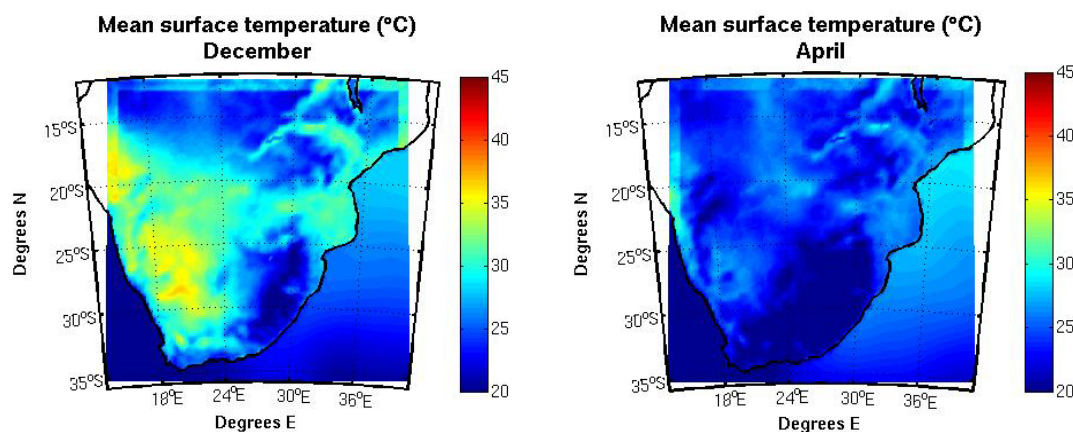


Figure 4-26: The average surface temperature for the month of December (left) and April (right).

Accumulating the stomatal flux over the day lit hours of every day from October 1 to April 30, representing the maize growing period, yields the result presented in Figure 4-27 below. The accumulation includes no threshold value, as threshold values in principal are species-specific, and the accumulation is done over all landuse categories within the domain. The flux is accumulated from 6a.m to 6p.m local time, which are the day lit hours, but as the modelled results for the stomatal flux is zero during night-time, this selection has little effect, besides on the computational time.

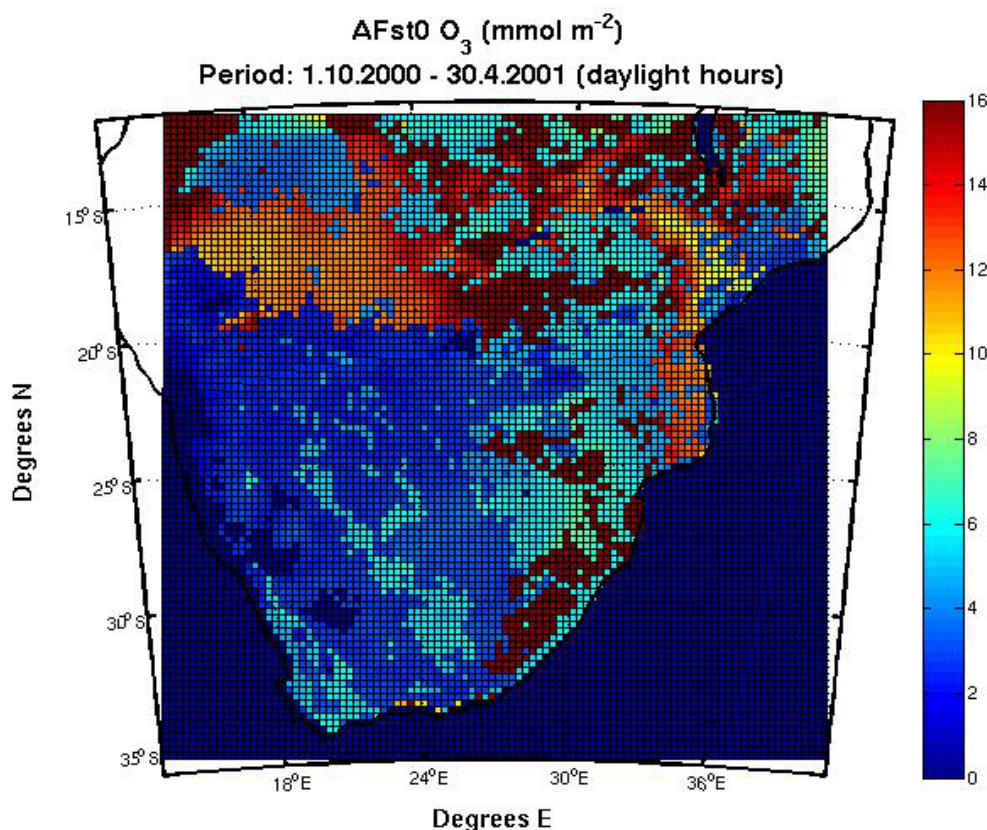


Figure 4-27: The accumulated flux of O₃ (mmol/m²) above zero threshold value, over the day lit hours of the period 1.10.2000-30.4.2001.

The pattern of high dose is recognized from the monthly mean plots of the flux. The land use categories of savannah and evergreen forests are the ones receiving the greatest dose over the 7 months. However, several of the various cropland- landuse categories are also estimated to receive doses of around 6mmol/m², which may be considered to be high enough to cause adverse effects in ozone-sensitive crop species. These specific critical levels are however considered in combination with an accumulated flux computed with a species-specific threshold value, yielding a somewhat lower dose than the one we have here. The guidance of risk-assessment given in Mills (2004) provides no critical level for assessing the risk to crops in large-scale modelling, but states that increasing flux indicates higher risk of damage.

As maize is an important crop within the area of the modelled domain, the accumulated flux over a typical single maize growing season from November through February is shown in

Figure 4-28. The flux is as before accumulated over a zero threshold value, and is given in mmol/m^2 .

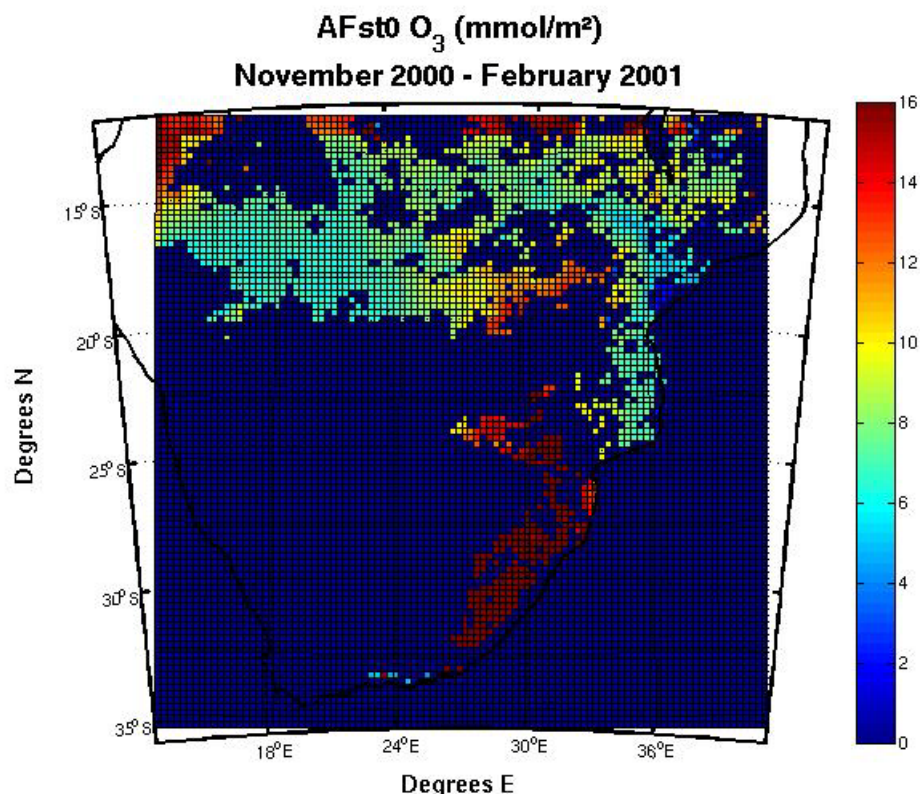


Figure 4-28: The accumulated flux O_3 above zero threshold over the maize growing season assumed estimated to the period 1.11.2000 to 30.2.2001.

The map shows low accumulated values over the part of the domain not covered by the previously mentioned sensitive landuse categories. The difference in dose from the dose-map accumulated over the full 7-month period is especially clear in the areas covered with grassland and cropland-categories. This is because the flux to these areas was especially high in April, which is not included in this accumulation period. The greatest dose values are found in the south-east part of the domain, to the landuse category of savannah and broadleaf forest. The dose is over twice as high in these areas than in the areas of the same landuse-categories across the northern part of the domain. The reason for this difference in dose might be because of the higher ozone concentration found in this area during all of the months (see Figure 4-24). A second explanation is that this area is of higher elevation, hence lower mean surface temperatures (see Figure 4-26). As explained in the previous chapter, high surface temperatures cause the stomatal conductance to decrease. The area west of Lake Malawi also displays a somewhat greater dose than the rest of the area of the same landuse category. This could be due to the previously discussed high ozone concentrations in this area in October.

Sum VPD function

The correlation between the measured and modelled mean flux for the June-period in Italy described in the previous chapter, was greatly improved by applying the sum-VPD function to the stomatal conductance. Based on this improvement in the dry and warm period of June, the same function has been applied to the stomatal conductance in the African domain, as the average temperature across the domain during the 7-month period on many cases exceeds the average temperature in Castelporziano during the June period.

The effect of applying the sum VPD function on the stomatal dose to the vegetation accumulated over the full 7-month period across the Southern African domain can be seen in Figure 4-29. The dose has been accumulated as before, with no threshold value and is given in mmol/m^2 .

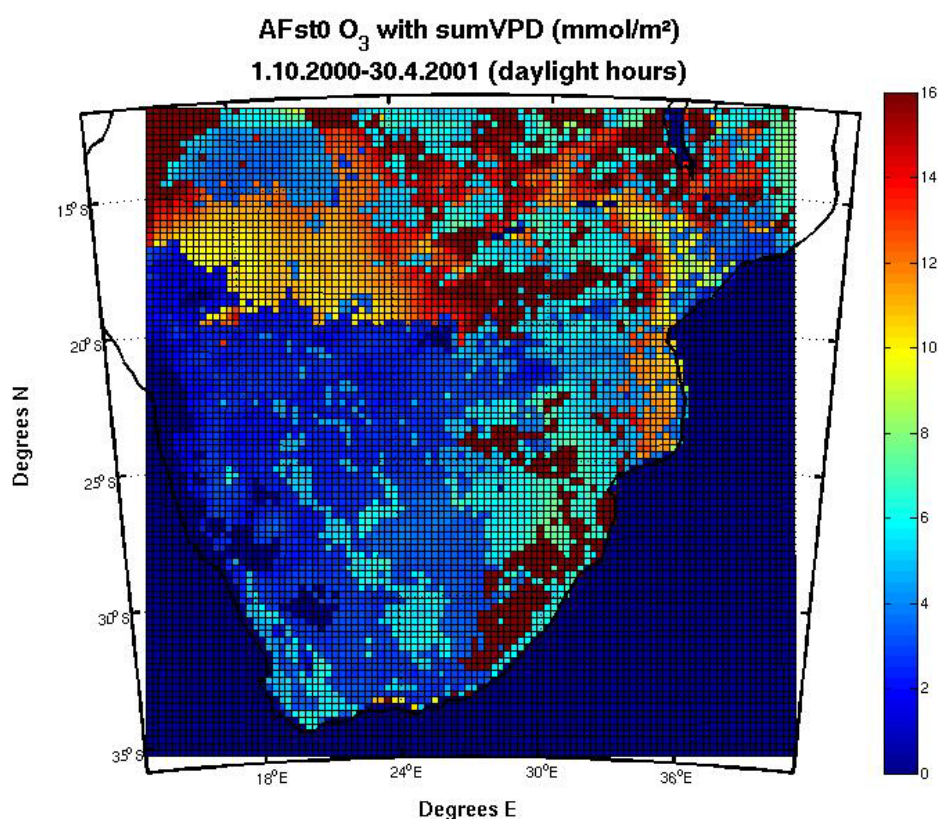


Figure 4-29: Accumulated stomatal flux over the period October 1st 2000- April 30th 2001.

The reduction in stomatal dose is greatest in the high-dose areas in the warmer north-western part of the domain. The parts of the domain with low accumulated flux show no greater difference. The average maximum-, mean- and minimum-values of the flux with and without the applied sum-VPD function are given in Table 4-3.

Table 4-3: Average values for the stomatal flux across the Southern African domain, with and without the limitations of the sum-VPD function. All values are given in nmol/m²s.

Month	Averaged flux without sum VPD		Averaged flux with sum VPD	
	Mean value (nmol/m ² s)	Maximum value (nmol/m ² s)	Mean value (nmol/m ² s)	Maximum value (nmol/m ² s)
October	0,32	5,69	0,26	5,50
November	0,36	5,39	0,31	5,10
December	0,36	5,51	0,32	5,19
January	0,39	5,70	0,35	5,59
February	0,34	5,65	0,33	5,58
March	0,37	5,16	0,36	5,09
April	1,71	6,72	1,68	6,33
Mean over all 7 months	0,55	5,68	0,52	5,48

The averaged difference across the entire domain is not very large, as the limiting effect of the sum- VPD function is concentrated in areas of both high flux rate and high temperatures.

To more accurately present the difference in dose across the 7-month period, the difference between the accumulated flux without, and the accumulated flux with the sum-VPD function is presented in Figure 4-30.

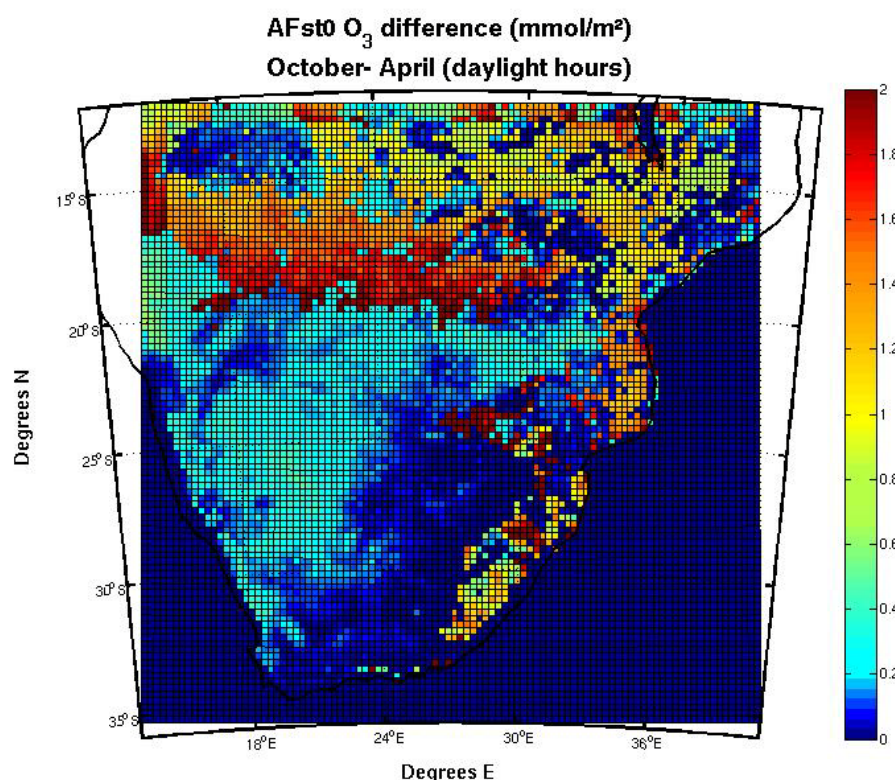


Figure 4-30: The difference in dose with and without the appliance of the sum-VPD function over the period 1.10.2000-30.4.2001. Notice the scale differs from the other dose presentations.

The total dose calculated with the limiting effect of the sum-VPD function over the maize-growing season from November through February is shown in Figure 4-31.

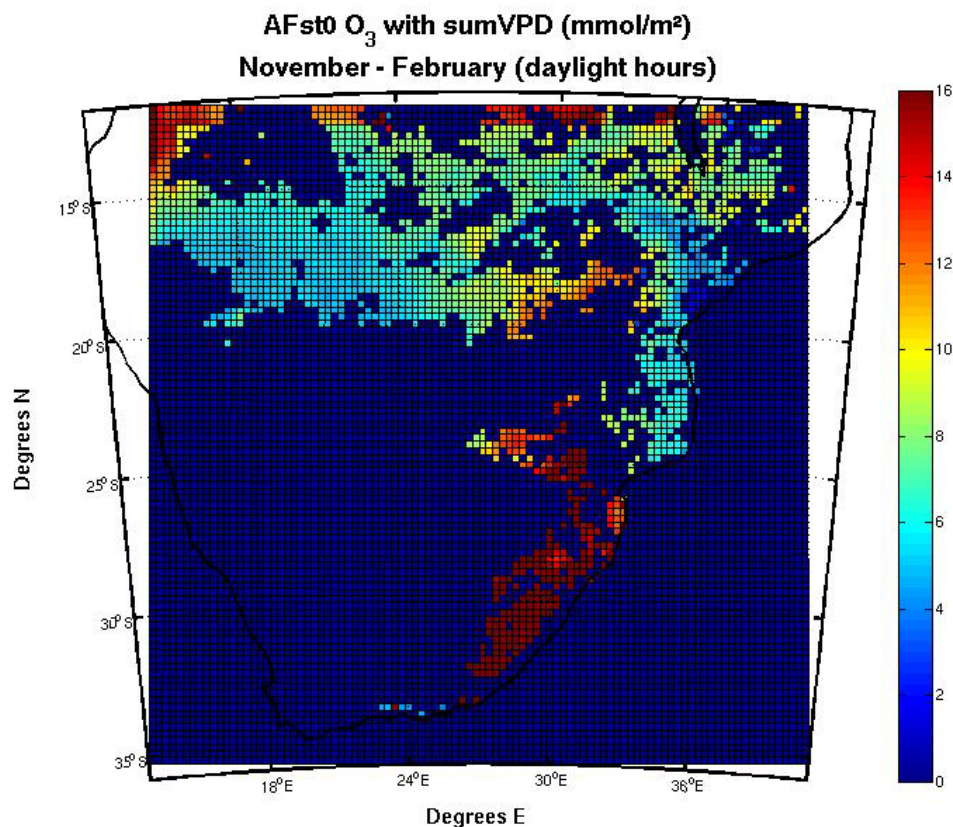


Figure 4-31: The dose of ozone to vegetation accumulated over day lit hours from 1.11.2000-28.2.2001.

As seen in the dose plot over the entire 7-month period, the difference is greatest in the north-western part of the domain, where the highest surface temperatures of the period are located. The difference between the dose calculated with and without the sum-VPD function, is presented in Figure 4-32. It shows the same pattern as the difference-plot over the whole 7-month period, however as the total doses are lower, the differences are smaller.

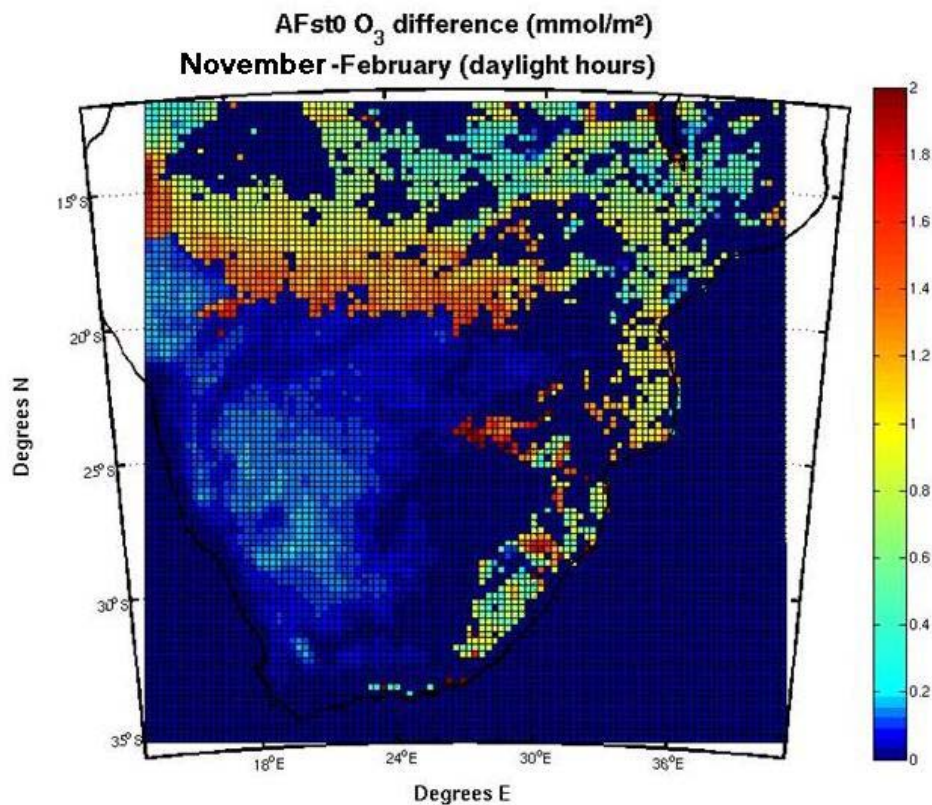


Figure 4-32: The difference in dose with and without the appliance of the sum-VPD function over the period 1.11.2000-28.2.2001.

According to the UNECE mapping manual developed for mapping critical levels of ozone to crops across Europe (Mills 2004), a simplified method is recommended for large-scale modelling like the simulations done for the purpose of this thesis. In this simplified approach only the parameters of temperature, light intensity, and VPD are accounted for in estimating the stomatal conductance. For crops across Europe the threshold value of $3\text{nmol/m}^2\text{s}$ is recommended in combination with the critical level for accumulated sum VDP of 8kPa .

Applying these threshold- and critical values derived for European crop species and conditions to the Southern African domain include some assumptions based on a less than biologically accurate basis. As seen from the previously presented flux maps, the cropland categories are not the landuse categories associated with the highest flux values. In fact, applying the UNECE- critical VPD value of 8kPa instead of 12kPa , yields fluxes in these landuse categories below $3\text{nmol/m}^2\text{s}$ for all months within the simulation, hence below the threshold value over which the accumulation is recommended to be executed.

As these threshold values are not developed African plants or climatic conditions, these results should not be regarded as conclusive in any way.

5 Summary and concluding remarks

Extensive research during the past few decades has established that the increased tropospheric background concentration of ozone due to increased emissions of ozone precursor gasses over the past century, have reached values of which adverse effects on vegetation can be expected. These effects include reduced biodiversity in some areas, as a result to ozone-sensitivity differences across plant species, economic loss due to reduced crop yield, and may in some cases affect food security in areas of high food demand due to high population growth rates in the future decades.

One main objective of this thesis has been to provide an estimate of the total stomatal dose of ozone to the vegetation of the Southern African area over a typical maize growing season. For this purpose the WRF-Chem model has been implemented, a mesoscale weather prediction system, fully coupled with a chemistry module. The dry deposition scheme developed by Wesely (1989) has been utilized to estimate the stomatal flux of ozone from the ambient air into the vegetation.

To validate the model, the results for the stomatal flux from two simulated test-periods are compared to fluxes derived from eddy covariance data gathered in Castelporziano, Italy, during the spring and summer period of 2007. Two periods of six days has been simulated from each of the periods “late spring” and “summer” as defined in Gerosa et al. (2009).

Comparison of the first period and the first days of the second period show an under-prediction of the day time canopy height ozone concentration, compared to the measured concentration, possibly due to inaccuracies in the transport, or underestimates of the emissions of ozone precursors. The modelled stomatal flux is compared to the flux derived from measurements for the daytime hours. For the first period the model slightly overestimated the stomatal flux of the day time hours, yielding a mean daytime flux of $5,7\text{nmol/m}^2\text{s}$, to the measured average value of $5,2\text{nmol/m}^2\text{s}$. The correlation coefficient of the day-time hours of the mean diurnal variation of the modelled versus the measured daytime flux for the first period is 0,73.

The second simulated period, part of the “summer period” as defined in Gerosa et al. (2009), was characterized by a lower measured stomatal flux, caused by overall dryer conditions at the measuring site, reducing the rate of evapotranspiration substantially. The modelled average day time flux for this period show an overestimated mean value of $3,6\text{nmol/m}^2\text{s}$, to the measured value of $2,0\text{nmol/m}^2\text{s}$. The higher daytime mean value is due to an overestimation of the afternoon conductance compared to the measured decreasing flux from midday towards the evening.

To account for the evaporative power of the atmosphere on the stomatal conductance, two different water vapor pressure deficit (VPD) functions were applied to the modelled results. The first one according to the Jarvis approach, with species-specific values according to open top chamber results from northern Italy, adapted from Gerosa et al (2005). The second VPD function applied is the sum VPD function as described in e.g. Pleijel et al. (2007) and Mills (2004), applied with the critical VPD value of 12hPa. The results were no greater increase in the correlation of the mean diurnal flux for the modelled part of the spring period. For the part of the dry summer period on the other hand, the application of the sum VPD

function lead to an increase in correlation with measured flux from -0.37 to 0.82. The overestimation of the modelled surface flux during the dry June period was greatly improved by implementing the sum-VPD function. As this was done in a post process, the lowered flux' influence on the modelled bottom layer ozone concentration could not be investigated, however the effect could contribute to explain the underestimation of the daytime concentrations done by the model.

The ozone concentrations simulated for the southern African domain shows similar average values for the bottom layer ozone concentrations as those estimated by Zunckel et al.(2006), with average values within the range of 20-45ppb. Peak values in the range of 70-100 ppb occurred throughout the period. These values are well above the threshold values above which plant damage can be expected.

The distribution of the average flux for each month in the period shows great differences across landuse categories, and limited similarities to the ozone distribution, leading to the conclusion that the flux is heavily dependent on the conductance, reflecting the landuse categories. The landuse categories yielding the highest flux values are those of "savannah" and "broadleaf forest". The pattern of high stomatal conductance changes abruptly as the seasonal category changes over the transition from March to April, resulting in a much more evenly distributed stomatal flux across landuse categories.

The stomatal flux of ozone was accumulated to yield the total stomatal dose of ozone to the vegetation across the domain over the full 7 month period. The dose was accumulated during only the day lit hours, and over a zero threshold value. The dose distribution reflects the high-flux pattern determined in part by the distribution of the sensitive landuse categories mentioned. The highest doses are found in the south-eastern part of the modelled domain, exceeding 16mmol/m² over the accumulation period. The high dose is reflecting the combination of high mean ozone concentrations, as a consequence of emissions from the South African Highveld, sensitive landuse categories, and low mean temperatures due to high geographical elevation.

The implementation of the limiting sum-VPD function caused an overall decrease in the flux averaged over the seven month period of 5,5%, with pronounced spatial variation in the distribution of the limiting effect. The implementation had greatest effect on the conductances in the warmer parts of the domain, coinciding with landuse categories associated with high fluxes.

Adapting the UNECE guidelines for assessing the risk of adverse effects to crops in Europe across the cropland-landuse categories of the southern African domain, implies applying threshold values derived for European species and conditions to the Southern African crops, which is biologically inaccurate. The recommended threshold value for large scale modelling in Europe of 3nmol/m²s is higher than the flux estimated for these landuse categories over all of the months resulting in no accumulated dose. However, this does not provide any conclusions about the risk of damage to Southern African crops, as there has not, to our knowledge, been developed appropriate flux threshold values, or critical VPD values for these species and climatic conditions.

5.1 Suggestions for future directions

To validate the emissions included in the simulations from both anthropogenically and natural sources, like biomass burning in the Southern African domain, the modelled NO₂ column over the domain could be compared to those observed, by e.g. satellite.

The results for the modelled dry deposition flux might differ greatly depending on the choice of boundary layer physics scheme. Simulating the same periods in Italy with different boundary layer schemes and comparing the results with measurements could prove useful in evaluating the dry deposition scheme.

To more accurately compare the modelled stomatal flux to fluxes derived from measurements, WRF-Chem simulations over a longer time-period and with a finer resolution could be advantageous. Also, in estimating the accuracy of the model, results should be compared with measurements made at sites representing different landuse categories defined in the dry deposition scheme.

As the 24 USGS landuse categories (when this land surface model is chosen) are grouped together into only a few Wesely categories, the full detail of the landuse model is not taken full advantage of when coupled to the dry deposition scheme. A review of the constant resistance values derived for each landuse category, and if possible expanding the dry deposition category set to yield a more elaborate set of categories could possibly improve the detail level of the dry deposition estimations.

Implementing the sum-VPD function to the modelled results did prove advantageous in the dry period modelled in Italy for this thesis. Implementing a dependency of the evaporative power of the atmosphere in the dry deposition scheme could, based on this result, be assumed to enhance the parameterization of the stomatal conductance. This would serve as a limitation to the stomatal flux in some cases, possibly yielding a difference to the modelled ozone concentrations especially during dry conditions. Another way of taking into account the plants dependence on water supply in the estimations of stomatal conductance would be to include the modelled soil water content in the dry deposition scheme.

As very limited data on dose-response relationships derived for the Southern African domain are available, the risk of damage to plants within the modelled domain can only be estimated by inaccurately applying relationships derived for European and North American species. The development of such relationships for species and climatic conditions typical of the Southern African area are necessary to assess the actual risk of damage to the vegetation in Africa. Such relationships should be developed for both natural species and agricultural crops of the region.

Appendix A

Values for r_i for every landuse category and season.

Landuse category	season1	seson 2	season3	season4	season5
1	0.10E+11	0.10E+11	0.10E+11	0.10E+11	0.10E+11
2	0.60E+02	0.10E+11	0.10E+11	0.10E+11	0.12E+03
3	0.60E+02	0.10E+11	0.10E+11	0.10E+11	0.12E+03
4	0.60E+02	0.10E+11	0.10E+11	0.10E+11	0.12E+03
5	0.60E+02	0.10E+11	0.10E+11	0.10E+11	0.12E+03
6	0.70E+02	0.10E+11	0.10E+11	0.10E+11	0.14E+03
7	0.12E+03	0.10E+11	0.10E+11	0.10E+11	0.24E+03
8	0.12E+03	0.10E+11	0.10E+11	0.10E+11	0.24E+03
9	0.12E+03	0.10E+11	0.10E+11	0.10E+11	0.24E+03
10	0.12E+03	0.12E+03	0.12E+03	0.10E+11	0.12E+03
11	0.70E+02	0.10E+11	0.10E+11	0.10E+11	0.14E+03
12	0.13E+03	0.10E+11	0.10E+11	0.10E+11	0.25E+03
13	0.70E+02	0.70E+02	.70E+02	0.70E+02	0.70E+02
14	0.13E+03	0.25E+03	0.25E+03	0.40E+03	0.25E+03
15	0.10E+03	0.50E+03	0.50E+03	0.80E+03	0.19E+03
16	0.10E+11	0.10E+11	0.10E+11	0.10E+11	0.10E+11
17	0.80E+02	0.10E+11	0.10E+11	0.10E+11	0.16E+03
18	0.10E+03	0.50E+03	0.50E+03	0.80E+03	0.19E+03
19	0.10E+11	0.10E+11	0.10E+11	0.10E+11	0.10E+11
20	0.80E+02	0.10E+11	0.10E+11	0.10E+11	0.16E+03
21	0.10E+03	0.50E+03	0.50E+03	0.80E+03	0.19E+03
22	0.10E+03	0.50E+03	0.50E+03	0.80E+03	0.19E+03
23	0.10E+11	0.10E+11	0.10E+11	0.10E+11	0.10E+11
24	0.10E+11	0.10E+11	0.10E+11	0.10E+11	0.10E+11
25	0.10E+11	0.10E+11	0.10E+11	0.10E+11	0.10E+11

Values for r_{lu} for every landuse category and season.

Landuse category	season1	seson 2	season3	season4	season5
1	0.20E+04	0.90E+04	0.90E+04	0.10E+11	0.40E+04
2	0.20E+04	0.90E+04	0.90E+04	0.10E+11	0.40E+04
3	0.20E+04	0.90E+04	0.90E+04	0.10E+11	0.40E+04
4	0.20E+04	0.90E+04	0.90E+04	0.10E+11	0.40E+04
5	0.20E+04	0.90E+04	0.90E+04	0.10E+11	0.40E+04
6	0.20E+04	0.90E+04	0.90E+04	0.10E+11	0.40E+04
7	0.20E+04	0.90E+04	0.90E+04	0.10E+11	0.40E+04
8	0.20E+04	0.90E+04	0.90E+04	0.10E+11	0.40E+04
9	0.20E+04	0.20E+04	0.20E+04	0.10E+11	0.20E+04
10	0.20E+04	0.90E+04	0.90E+04	0.10E+11	0.40E+04
11	0.20E+04	0.90E+04	0.90E+04	0.10E+11	0.20E+04
12	0.20E+04	0.20E+04	0.20E+04	0.20E+04	0.20E+04
13	0.20E+04	0.40E+04	0.40E+04	0.60E+04	0.20E+04
14	0.20E+04	0.80E+04	0.80E+04	0.90E+04	0.30E+04
15	0.10E+11	0.10E+11	0.10E+11	0.10E+11	0.10E+11
16	0.25E+04	0.90E+04	0.90E+04	0.90E+04	0.40E+04

17	0.20E+04	0.80E+04	0.80E+04	0.90E+04	0.30E+04
18	0.10E+11	0.10E+11	0.10E+11	0.10E+11	0.10E+11
19	0.25E+04	0.90E+04	0.90E+04	0.90E+04	0.40E+04
20	0.20E+04	0.80E+04	0.80E+04	0.90E+04	0.30E+04
21	0.20E+04	0.80E+04	0.80E+04	0.90E+04	0.30E+04
22	0.10E+11	0.10E+11	0.10E+11	0.10E+11	0.10E+11
23	0.10E+11	0.10E+11	0.10E+11	0.10E+11	0.10E+11
24	0.10E+11	0.10E+11	0.10E+11	0.10E+11	0.10E+11
25	0.10E+11	0.10E+11	0.10E+11	0.10E+11	0.10E+11

Values for r_{ac} for every landuse category and season:

Landuse category	season1	seson 2	season3	season4	season5
1	0.20E+03	0.10E+03	0.10E+03	0.10E+03	0.10E+03
2	0.20E+03	0.15E+03	0.10E+02	0.10E+02	0.50E+02
3	0.20E+03	0.15E+03	0.10E+02	0.10E+02	0.50E+02
4	0.20E+03	0.15E+03	0.10E+02	0.10E+02	0.50E+02
5	0.20E+04	0.15E+03	0.10E+02	0.10E+02	0.50E+02
6	0.10E+03	0.15E+04	0.10E+04	0.10E+04	0.12E+04
7	0.10E+03	0.10E+03	0.10E+03	0.10E+02	0.80E+02
8	0.10E+03	0.10E+03	0.10E+03	0.10E+02	0.80E+02
9	0.10E+03	0.10E+03	0.10E+03	0.10E+02	0.80E+02
10	0.20E+04	0.10E+03	0.10E+03	0.10E+02	0.10E+03
11	0.20E+04	0.15E+04	0.10E+04	0.10E+04	0.12E+04
12	0.20E+04	0.20E+04	0.20E+04	0.20E+04	0.20E+04
13	0.20E+04	0.20E+04	0.20E+04	0.20E+04	0.20E+04
14	0.20E+04	0.20E+04	0.20E+04	0.20E+04	0.20E+04
15	0.00E+00	0.17E+04	0.15E+04	0.15E+04	0.15E+04
16	0.30E+03	0.00E+00	0.00E+00	0.00E+00	0.00E+00
17	0.20E+04	0.20E+03	0.10E+03	0.50E+02	0.20E+03
18	0.00E+00	0.17E+04	0.15E+04	0.15E+04	0.15E+04
19	0.30E+03	0.00E+00	0.00E+00	0.00E+00	0.00E+00
20	0.20E+04	0.20E+03	0.10E+03	0.50E+02	0.20E+03
21	0.20E+04	0.17E+04	0.15E+04	0.15E+04	0.15E+04
22	0.00E+00	0.17E+04	0.15E+04	0.15E+04	0.15E+04
23	0.00E+00	0.00E+00	0.00E+00	0.00E+00	0.00E+00
24	0.00E+00	0.00E+00	0.00E+00	0.00E+00	0.00E+00
25	0.10E+03	0.00E+00	0.00E+00	0.00E+00	0.00E+00

Values for r_{gso} for ozone for every landuse category and season:

Landuse category	season1	seson 2	season3	season4	season5
1	0.15E+03	0.15E+03	0.15E+03	0.35E+04	0.15E+03
2	0.15E+03	0.15E+03	0.15E+03	0.35E+04	0.15E+03
3	0.15E+03	0.15E+03	0.15E+03	0.35E+04	0.15E+03
4	0.15E+03	0.15E+03	0.15E+03	0.35E+04	0.15E+03
5	0.20E+03	0.20E+03	0.20E+03	0.35E+04	0.20E+03
6	0.20E+03	0.20E+03	0.20E+03	0.35E+04	0.20E+03
7	0.20E+03	0.20E+03	0.20E+03	0.35E+04	0.20E+03
8	0.20E+03	0.20E+03	0.20E+03	0.35E+04	0.20E+03

9	0.20E+03	0.20E+03	0.20E+03	0.35E+04	0.20E+03
10	0.20E+03	0.20E+03	0.20E+03	0.35E+04	0.20E+03
11	0.20E+03	0.20E+03	0.20E+03	0.35E+04	0.20E+03
12	0.20E+03	0.20E+03	0.20E+03	0.20E+03	0.20E+03
13	0.20E+03	0.20E+03	0.20E+03	0.35E+04	0.20E+03
14	0.30E+03	0.30E+03	0.30E+03	0.35E+04	0.30E+03
15	0.20E+04	0.20E+04	0.20E+04	0.20E+04	0.20E+04
16	0.10E+04	0.80E+03	0.10E+04	0.35E+04	0.10E+04
17	0.30E+03	0.30E+03	0.30E+03	0.35E+04	0.30E+03
18	0.40E+03	0.40E+03	0.40E+03	0.40E+03	0.40E+03
19	0.10E+04	0.80E+03	0.10E+04	0.35E+04	0.10E+04
20	0.30E+03	0.30E+03	0.30E+03	0.35E+04	0.30E+03
21	0.30E+03	0.30E+03	0.30E+03	0.35E+04	0.30E+03
22	0.40E+03	0.40E+03	0.40E+03	0.40E+03	0.40E+03
23	0.35E+04	0.35E+04	0.35E+04	0.35E+04	0.35E+04
24	0.40E+03	0.40E+03	0.40E+03	0.40E+03	0.40E+03
25	0.30E+03	0.30E+03	0.60E+03	0.30E+03	0.40E+03

Values for r_{clo} for exposed surfaces in the lower canopy for ozone, for every landuse category and season:

Landuse category	season1	seson 2	season3	season4	season5
1	0.10E+04	0.40E+03	0.10E+04	0.10E+04	0.10E+04
2	0.10E+04	0.40E+03	0.10E+04	0.10E+04	0.10E+04
3	0.10E+04	0.40E+03	0.10E+04	0.10E+04	0.10E+04
4	0.10E+04	0.40E+03	0.10E+04	0.10E+04	0.10E+04
5	0.10E+04	0.40E+03	0.40E+03	0.40E+03	0.50E+03
6	0.10E+04	0.40E+03	0.40E+03	0.10E+04	0.50E+03
7	0.10E+04	0.40E+03	0.40E+03	0.10E+04	0.50E+03
8	0.10E+04	0.40E+03	0.40E+03	0.10E+04	0.50E+03
9	0.10E+04	0.10E+04	0.10E+04	0.10E+04	0.10E+04
10	0.10E+04	0.40E+03	0.40E+03	0.40E+03	0.50E+03
11	0.10E+04	0.40E+03	0.40E+03	0.40E+03	0.15E+04
12	0.10E+04	0.10E+04	0.10E+04	0.10E+04	0.10E+04
13	0.10E+04	0.10E+04	0.10E+04	0.15E+04	0.15E+04
14	0.10E+04	0.60E+03	0.60E+03	0.60E+03	0.70E+03
15	0.10E+11	0.10E+11	0.10E+11	0.10E+11	0.10E+11
16	0.10E+04	0.40E+03	0.80E+03	0.80E+03	0.60E+03
17	0.10E+04	0.60E+03	0.60E+03	0.60E+03	0.70E+03
18	0.10E+11	0.10E+11	0.10E+11	0.10E+11	0.10E+11
19	0.10E+04	0.40E+03	0.80E+03	0.80E+03	0.60E+03
20	0.10E+04	0.60E+03	0.60E+03	0.60E+03	0.70E+03
21	0.10E+04	0.60E+03	0.60E+03	0.60E+03	0.70E+03
22	0.10E+11	0.10E+11	0.10E+11	0.10E+11	0.10E+11
23	0.10E+11	0.10E+11	0.10E+11	0.10E+11	0.10E+11
24	0.10E+11	0.10E+11	0.10E+11	0.10E+11	0.10E+11
25	0.10E+11	0.10E+11	0.10E+11	0.10E+11	0.10E+11

Henry's law coefficients for pH 7:

H*(p_hno4)=2.00E+13
H*(p_h2o2)=7.45E+4
H*(p_co)=8.20E-3
H*(p_ald)=1.14E+1
H*(p_op1)=2.21E+2
H*(p_op2)=1.68E+6
H*(p_paa)=4.73E+2
H*(p_ket)=3.30E+1
H*(p_gly)=1.40E+6
H*(p_mgly)=3.71E+3
H*(p_dcb)=1.40E+6
H*(p_onit)=1.13E+0
H*(p_so2)=2.53E+5
H*(p_eth)=2.00E-3

H*(p_hc3)=1.42E-3
H*(p_hc5)=1.13E-3
H*(p_hc8)=1.42E-3
H*(p_olt)=4.76E-3
H*(p_oli)=1.35E-3
H*(p_tol)=1.51E-1
H*(p_csl)=4.00E+5
H*(p_xyl)=1.45E-1
H*(p_iso)=4.76E-3
H*(p_hno3)=2.69E+13
H*(p_ora1)=9.85E+6
H*(p_ora2)=9.63E+5
H*(p_nh3)=1.04E+4
H*(p_n2o5)=1.00E+10

Reactivity factors

f0(p_no)=0.
f0(p_pan)=0.1
f0(p_o3)=1.
f0(p_hcho)=0.
f0(p_aco3)=1.
f0(p_tpan)=0.1
f0(p_hono)=0.1
f0(p_no3)=1.
f0(p_hno4)=0.1
f0(p_h2o2)=1.
f0(p_co)=0.
f0(p_ald)=0.
f0(p_op1)=0.1
f0(p_op2)=0.1
f0(p_paa)=0.1
f0(p_ket)=0.
f0(p_gly)=0.
f0(p_mgly)=0.
f0(p_dcb)=0.
f0(p_onit)=0.
f0(p_so2)=0.

f0(p_eth)=0.
f0(p_so2)=0.
f0(p_eth)=0.
f0(p_dcb)=0.
f0(p_onit)=0.
f0(p_so2)=0.
f0(p_eth)=0.
f0(p_hc3)=0.
f0(p_hc5)=0.
f0(p_hc8)=0.
f0(p_olt)=0.
f0(p_oli)=0.
f0(p_tol)=0.
f0(p_csl)=0.
f0(p_xyl)=0.
f0(p_iso)=0.
f0(p_hno3)=0.
f0(p_ora1)=0.
f0(p_ora2)=0.
f0(p_nh3)=0.
f0(p_n2o5)=1.

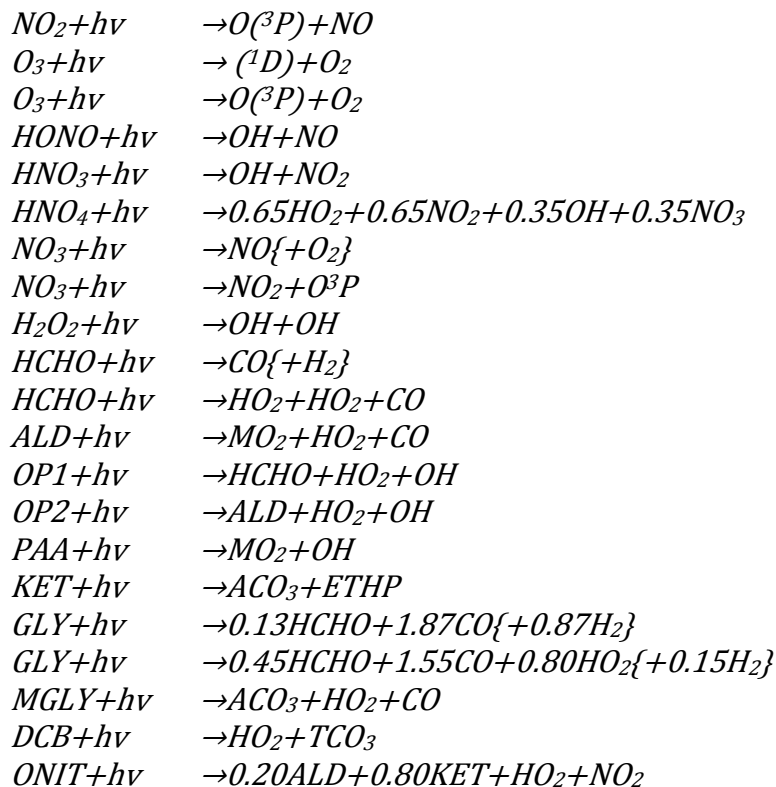
STABILITY CONDITION	$\phi_p\left(\frac{z}{L}\right)$	INTEGRAL $I = \int_{z_r}^{\Delta z} \int_{z_r}^z \phi_p\left(\frac{x}{L}\right) \frac{dx}{x} dz$
Stable ($\frac{z}{L} > 0$)	$\phi_p\left(\frac{z}{L}\right) = 0.74 + 4.7\left(\frac{z}{L}\right)$	$I = 0.74(\Delta z \ln \frac{\Delta z}{z_r} - \Delta z + z_r) + \frac{2.35}{L}(\Delta z - z_r)^2$
Neutral ($\frac{z}{L} = 0$)	$\phi_p\left(\frac{z}{L}\right) = 0.74$	$I = 0.74(\Delta z \ln \frac{\Delta z}{z_r} - \Delta z + z_r)$
Unstable ($\frac{z}{L} < 0$)	$\phi_p\left(\frac{z}{L}\right) = 0.74\left[1 - 9\left(\frac{z}{L}\right)\right]^{-\frac{1}{2}}$	$I = 0.74 \Delta z \ln \left[\left(\frac{\sqrt{1 - 9\frac{\Delta z}{L}} - 1}{\sqrt{1 - 9\frac{z_r}{L}} - 1} \right) \left(\frac{\sqrt{1 - 9\frac{z_r}{L}} + 1}{\sqrt{1 - 9\frac{\Delta z}{L}} + 1} \right) \right]$ $+ 0.104 L \left[\sqrt{1 - 9\frac{\Delta z}{L}} - \sqrt{1 - 9\frac{z_r}{L}} \right]$

Table 3-1: Integrals required to calculate cell average deposition velocity. (McRae, Goodin et al. 1982)

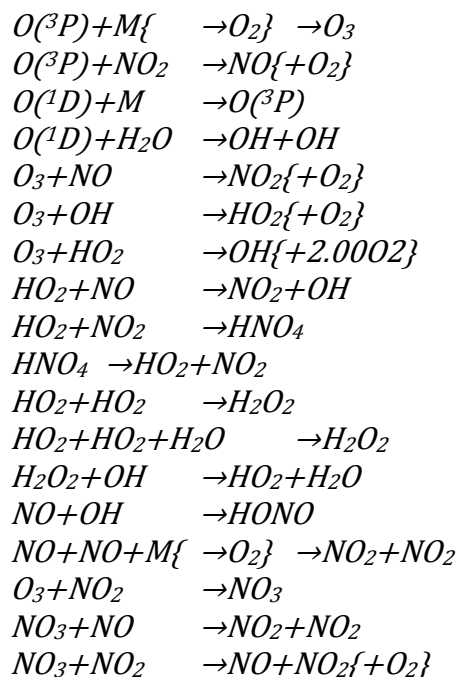
Appendix B

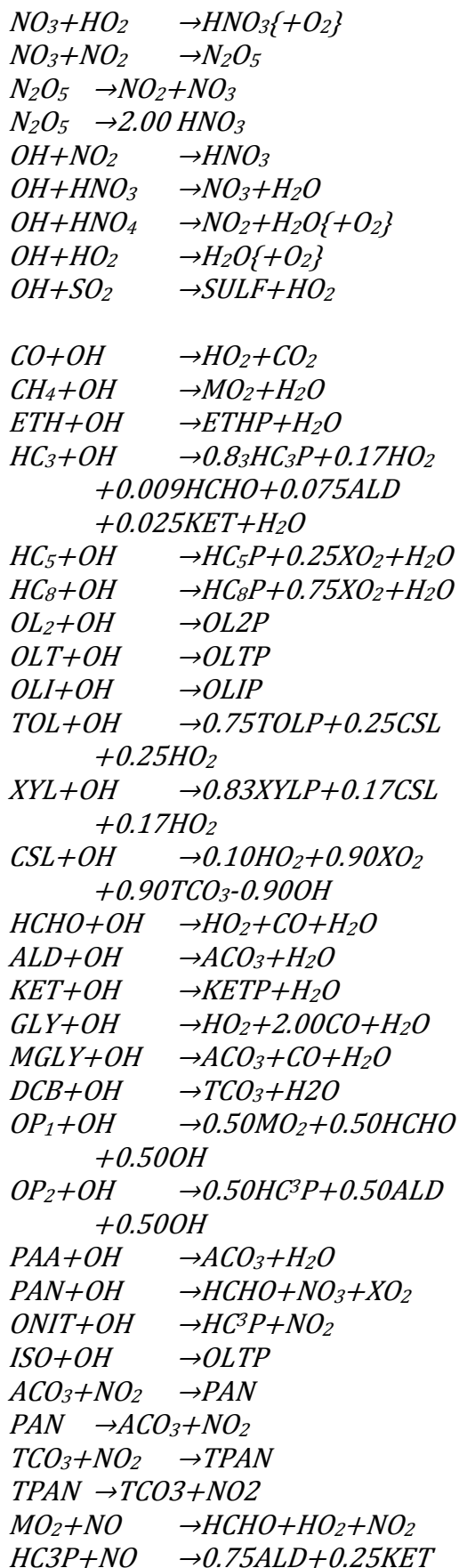
The reactions of the RADM2 chemistry scheme. The organic chemistry is represented by 26 stable species and 16 peroxy radicals.

Photolysis reactions



Chemical tropospheric reactions





$+0.09\text{HCHO}+0.036\text{ONIT}$
 $+0.964\text{NO}_2+0.964\text{HO}_2$
 $\text{HC5P}+\text{NO} \rightarrow 0.38\text{ALD}+0.69\text{KET}$
 $+0.08\text{ONIT}+0.92\text{NO}_2$
 $+0.92\text{HO}_2$
 $\text{HC8P}+\text{NO} \rightarrow 0.35\text{ALD}+1.06\text{KET}$
 $+0.04\text{HCHO}+0.24\text{ONIT}$
 $+0.76\text{NO}_2+0.76\text{HO}_2$
 $\text{OL2P}+\text{NO} \rightarrow 1.60\text{HCHO}+\text{HO}_2+\text{NO}_2$
 $+0.20\text{ALD}$
 $\text{OLTP}+\text{NO} \rightarrow \text{ALD}+\text{HCHO}+\text{HO}_2+\text{NO}_2$
 $\text{OLIP}+\text{NO} \rightarrow \text{HO}_2+1.45\text{ALD}$
 $+0.28\text{HCHO}+0.10\text{KET}+\text{NO}_2$
 $\text{ACO}_3+\text{NO} \rightarrow \text{MO}_2+\text{NO}_2$
 $\text{TCO}_3+\text{NO} \rightarrow \text{NO}_2+0.92\text{HO}_2$
 $+0.89\text{GLY}+0.11\text{MGLY}$
 $+0.05\text{ACO}_3+0.95\text{CO}$
 $+2.00\text{XO}_2$
 $\text{TOLP}+\text{NO} \rightarrow \text{NO}_2+\text{HO}_2+0.17\text{MGLY}$
 $+0.16\text{GLY}+0.70\text{DCB}$
 $\text{XYLP}+\text{NO} \rightarrow \text{NO}_2+\text{HO}_2+0.45\text{MGLY}$
 $+0.806\text{DCB}$
 $\text{ETHP}+\text{NO} \rightarrow \text{ALD}+\text{HO}_2+\text{NO}_2$
 $\text{KETP}+\text{NO} \rightarrow \text{MGLY}+\text{NO}_2+\text{HO}_2$
 $\text{OLN}+\text{NO} \rightarrow \text{HCHO}+\text{ALD}+2.00\text{NO}_2$
 $\text{HCHO}+\text{NO}_3 \rightarrow \text{HO}_2+\text{HNO}_3+\text{CO}$
 $\text{ALD}+\text{NO}_3 \rightarrow \text{ACO}_3+\text{HNO}_3$
 $\text{GLY}+\text{NO}_3 \rightarrow \text{HNO}_3+\text{HO}_2+2.00\text{CO}$
 $\text{MGLY}+\text{NO}_3 \rightarrow \text{HNO}_3+\text{ACO}_3+\text{CO}$
 $\text{DCB}+\text{NO}_3 \rightarrow \text{HNO}_3+\text{TCO}_3$
 $\text{CSL}+\text{NO}_3 \rightarrow \text{HNO}_3+\text{XNO}_2+0.50\text{CSL}$
 $\text{OL2}+\text{NO}_3 \rightarrow \text{OLN}$
 $\text{OLT}+\text{NO}_3 \rightarrow \text{OLN}$
 $\text{OLI}+\text{NO}_3 \rightarrow \text{OLN}$
 $\text{ISO}+\text{NO}_3 \rightarrow \text{OLN}$
 $\text{OL2}+\text{O}_3 \rightarrow \text{HCHO}+0.42\text{CO}+0.40\text{ORA1}$
 $+0.12\text{HO}_2$
 $\text{OLT}+\text{O}_3 \rightarrow 0.53\text{HCHO}+0.50\text{ALD}$
 $+0.33\text{CO}+0.20\text{ORA1}$
 $+0.20\text{ORA2}+0.23\text{HO}_2$
 $+0.22\text{MO}_2+0.10\text{OH}$
 $+0.06\text{CH}_4$
 $\text{OLI}+\text{O}_3 \rightarrow 0.18\text{HCHO}+0.72\text{ALD}$
 $+0.10\text{KET}+0.23\text{CO}$
 $+0.06\text{ORA1}+0.29\text{ORA2}$
 $+0.09\text{CH}_4+0.26\text{HO}_2$
 $+0.31\text{MO}_2+0.14\text{OH}$

$ISO+O_3 \rightarrow 0.53HCHO+0.50ALD$
 $+0.33CO+0.20ORA1$
 $+0.20ORA2+0.23HO_2$
 $+0.22MO_2+0.10OH$
 $HO_2+MO_2 \rightarrow OP1$
 $HO_2+ETHP \rightarrow OP2$
 $HO_2+HC3P \rightarrow OP2$
 $HO_2+HC5P \rightarrow OP2$
 $HO_2+HC8P \rightarrow OP2$
 $HO_2+OL2P \rightarrow OP2$
 $HO_2+OLTP \rightarrow OP2$
 $HO_2+OLIP \rightarrow OP2$
 $HO_2+KETP \rightarrow OP2$
 $HO_2+ACO_3 \rightarrow PAA$
 $HO_2+TOLP \rightarrow OP2$
 $HO_2+XYLP \rightarrow OP2$
 $HO_2+TCO_3 \rightarrow OP2$
 $HO_2+OLN \rightarrow ONIT$
 $MO_2+MO_2 \rightarrow 1.50HCHO+HO_2$
 $MO_2+ETHP \rightarrow 0.75HCHO+HO_2$
 $+0.75ALD$
 $MO_2+HC_3P \rightarrow 0.75HCHO+HO_2$
 $+0.15ALD+0.6KET$
 $MO_2+HC5P \rightarrow 0.77HCHO+HO_2$
 $+0.41ALD+0.75KET$
 $MO_2+HC8P \rightarrow 0.80HCHO+HO_2$
 $+0.46ALD+1.39KET$
 $MO_2+OL2P \rightarrow 1.55HCHO+HO_2$
 $+0.35ALD$
 $MO_2+OLTP \rightarrow 1.25HCHO+HO_2$
 $+0.75ALD$
 $MO_2+OLIP \rightarrow 0.89HCHO+HO_2$
 $+0.725ALD+0.55KET$
 $MO_2+KETP \rightarrow 0.75HCHO+HO_2$
 $+0.75MGLY$
 $MO_2+ACO_3 \rightarrow HCHO+0.50HO_2$
 $+0.50MO_2+0.50ORA2$
 $MO_2+TOLP \rightarrow HCHO+2.00HO_2$
 $+0.17MGLY+0.16GLY$
 $+0.70DCB$
 $MO_2+XYLP \rightarrow HCHO+2.00HO_2$
 $+0.45MGLY+0.806DCB$
 $MO_2+TCO_3 \rightarrow 0.50HCHO+0.50ORA_2$
 $+0.445GLY+0.055MGLY$
 $+0.025ACO_3+0.475CO$
 $+0.46HO_2+XO_2$
 $ETHP+ACO_3 \rightarrow ALD+0.50HO_2$

$+0.50\text{MO}_2+0.50\text{ORA}_2$
 $\text{HC3P}+\text{ACO}_3 \rightarrow 0.2\text{ALD}+0.8\text{KET}$
 $+0.50\text{HO}_2+0.50\text{ORA}_2$
 $+0.50\text{MO}_2$
 $\text{HC5P}+\text{ACO}_3 \rightarrow 0.14\text{ALD}+0.86\text{KET}$
 $+0.50\text{HO}_2+0.50\text{ORA}_2$
 $+0.50\text{MO}_2$
 $\text{HC8P}+\text{ACO}_3 \rightarrow 0.1\text{ALD}+0.9\text{KET}$
 $+0.50\text{HO}_2+0.50\text{ORA}_2$
 $+0.50\text{MO}_2$
 $\text{OL2P}+\text{ACO}_3 \rightarrow 0.80\text{HCHO}+0.60\text{ALD}$
 $+0.50\text{HO}_2+0.50\text{ORA}_2$
 $+0.50\text{MO}_2$
 $\text{OLTP}+\text{ACO}_3 \rightarrow \text{ALD}+0.50\text{HCHO}$
 $+0.50\text{HO}_2+0.50\text{ORA}_2$
 $+0.50\text{MO}_2$
 $\text{OLIP}+\text{ACO}_3 \rightarrow 0.725\text{ALD}+0.55\text{KET}$
 $+0.14\text{HCHO}+0.50\text{HO}_2$
 $+0.50\text{MO}_2+0.50\text{ORA}_2$
 $\text{KETP}+\text{ACO}_3 \rightarrow \text{MGLY}+0.50\text{HO}_2$
 $+0.50\text{ORA}_2+0.50\text{MO}_2$
 $\text{ACO}_3+\text{ACO}_3 \rightarrow 2.00\text{MO}_2$
 $\text{ACO}_3+\text{TOLP} \rightarrow 0.8\text{MGLY}+0.2\text{GLY}$
 $+1.00\text{DCB}+\text{HO}_2+\text{MO}_2$
 $\text{ACO}_3+\text{XYLP} \rightarrow \text{MO}_2+1.00\text{MGLY}$
 $+1.00\text{DCB}+\text{HO}_2$
 $\text{ACO}_3+\text{TCO}_3 \rightarrow \text{MO}_2+0.92\text{HO}_2$
 $+0.89\text{GLY}+0.11\text{MGLY}$
 $+0.05\text{ACO}_3+0.95\text{CO}$
 $+2.00\text{XO}_2$
 $\text{XO}_2+\text{HO}_2 \rightarrow \text{OP}_2$
 $\text{XO}_2+\text{MO}_2 \rightarrow \text{HCHO}+\text{HO}_2$
 $\text{XO}_2+\text{ACO}_3 \rightarrow \text{MO}_2$
 $\text{XO}_2+\text{XO}_2 \rightarrow \text{H}_2\text{O}$
 $\text{XO}_2+\text{NO} \rightarrow \text{NO}_2$
 $\text{XNO}_2+\text{NO}_2 \rightarrow \text{ONIT}$
 $\text{XNO}_2+\text{HO}_2 \rightarrow \text{OP}_2$
 $\text{XNO}_2+\text{MO}_2 \rightarrow \text{HCHO}+\text{HO}_2$
 $\text{XNO}_2+\text{ACO}_3 \rightarrow \text{MO}_2$
 $\text{XNO}_2+\text{XNO}_2 \rightarrow \text{H}_2\text{O}$
 $\text{MO}_2+\text{OLN} \rightarrow 1.75\text{HCHO}+.5\text{HO}_2$
 $+ \text{ALD}+\text{NO}_2$
 $\text{ACO}_3+\text{OLN} \rightarrow \text{HCHO}+\text{ALD}+0.50\text{ORA}_2$
 $+ \text{NO}_2+0.50\text{MO}_2$
 $\text{OLN}+\text{OLN} \rightarrow 2.00\text{HCHO}+2.00\text{ALD}$
 $+2.00\text{NO}_2$

List of figures

Figure 2-1: Modelled changes in surface ozone concentrations from pre-industrial times to 2008. Multi-model annual surface mean mixing ratio in ppb for pre-industrial times (left) and 2008 (right). (Modified from Fowler et al. 2008).	11
Figure 2-2: Per-capita emissions of the ozone precursors (NO_x , nmVOCs, CH_4 , CO) in the year 2000, for the world, the EU-27 and the UK (From Fowler and et.al. 2008)	14
Figure 2-3: Ozone production and loss dependent on NO_x in different regimes The solid line corresponds to CH_4/CO oxidation, yielding either O_3 production or loss. Broken curves illustrate the effect of additional nmVOC inputs. (From Fowler et al. 2008)	19
Figure 2-4: Schematic representation of the main O_3 production and loss processes in the very low- NO_x regime. The dominant processes are shown in black. From (Fowler and et.al. 2008)	20
Figure 2-5: Schematic representation of the main O_3 production and loss processes in the low- NO_x regime. The dominant processes are shown in black. From (Fowler et.al. 2008).	22
Figure 2-6: Schematic representation of the main O_3 production and loss processes in the high- NO_x regime. The dominant processes are shown in black. From (Fowler and et.al. 2008)	23
Figure 2-7: Geographical distribution of the estimated global present-day crop production loss in metric tons/ km^2 , derived from the gridded average relative yield loss (Van Dingenen, Dentener et al. 2009)	25
Figure 2-8: Indirect radiative forcing from O_3 increases alone compared to 1900. Derived from simulated changes in land-carbon storage. Upper line for high plant sensitivity to O_3 , lower line for low sensitivity. Black bars and symbols are estimates of direct O_3 radiative forcing for 2000 (square) and 2100 (triangle). (Sitch, Cox et al. 2007)	26
Figure 2-9: Schematic transverse section through a leaf, illustrating the arrangement of various cell types. (Nobel 2005)	27
Figure 2-10: Response functions combined into three sensitivity categories. Solid line represents sensitive crops (wheat, water melon, pulses, cotton, turnip, tomato, onion, soybean and lettuce), dotted line moderately sensitive (sugar beet, potato, oilseed rape, tobacco, rice, maize, grape and broccoli), and stippled line resistant crops (barley and fruit represented by plum and strawberry). (Mills, Buse et al. 2007)	32
Figure 2-11: Modelled R_{CL} values for crops across Europe for the year 2000. R_{CL} (the relative exceedance above the critical value (CL), 3000ppb h for AOT40 metrics, 1mmol m^{-2} for Afst6) represents the ratio of modelled flux or exposure to the relevant critical level for AOT40 metrics (left), and Afst 6 metrics (right), and are only displayed for $R_{\text{CL}} > 1.0$. (From Simpson, Ashmore et al. 2007).	33
Figure 2-12: The stomatal conductance algorithm estimates the flux of ozone through the stoma by utilizing the resistance analogy. (Modified from Nobel (2005))	34

Figure 2-13: The parameterization used for the phenology function (f_{phen}) for wheat. (From P2007)	36
Figure 2-14: a) The function of f_{light} , representing the short-term response of light on the stomatal conductance. b) The function of f_{temp} , representing the short-term response of temperature on the stomatal conductance. The boundary line is used to define the maximal influence on the conductance. All the data points used are from different investigations, for references see P2007. (From P2007).....	37
Figure 2-15: a) The VPD-function representing the short-term response of ambient air VPD on the stomatal conductance. The boundary line is used to define the maximal influence on the conductance. All the data points used are from different investigations, for references see P2007. b) The ozone function f_{O3} , describing the long-term effect of ozone induced leaf senescence for wheat. AFst 0 is the accumulated flux with no flux threshold. (From P2007)38	
Figure 3-1: The WRF model system components. (From Skamarock, Klemp et al. 2008)	40
Figure 3-3: Horizontal and vertical grids used in the ARW. (From Skamarock, Klemp et al. 2008)	41
Figure 3-2: The terrain-following hydrostatic-pressure vertical coordinate η , and P_{ht} is the pressure at the top constant pressure surface. (From Skamarock, Klemp et al. 2008)	41
Figure 3-4: The two European domains plotted with their 24 USGS landuse category, plotted in matlab,.....	44
Figure 3-5: The southern African domain, with the 24 category USGS landuse categories. .	45
Figure 3-6: Emissions of NO_x (top panels) and CO (bottom panels). European emissions for June 2007 12:00 local time (left panels), emissions in the Southern African domain for Desember 2000, 12:00 local time (right panels). All emissions are in mole/km ² hr.....	47
Figure 3-7: Schematic diagram of the pathway resistances used in the Wesely module. (Modified from Wesely (1989))	49
Figure 3-8: Idealized representation of the airshed surface.(modified from (McRae, Goodin et al. 1982))	50
Figure 3-9: Simple illustration of the models two bottom layer cells. (McRae, Goodin et al. 1982)	54
Figure 3-10: Variation of the average deposition velocity as a function of atmospheric stability and the cell height. ($z_0 = 0.01m, u = 2.5 m/s, v_{g,zr} = 0.01 m/s$) (McRae, Goodin et al. 1982)	55
Figure 4-1: Measured ozone concentrations and fluxes for a) the spring period, and b) the summer period. The vertical lines indicate the two periods which have been simulated in WRF-Chem. (Modified from Gerosa, Finco et al. 2009a)	61
Figure 4-2: The average modelled ozone mixing ratio (ppb) over the period May 21-26.....	62

Figure 4-3: Measured wins speed and direction (top panel) and modelled windspeed and direction at 10m height (bottom panel), over the period May 21-26.	63
Figure 4-4: Ozone mixing ratio from measurements (thin line) and modelled (thick line) for the period may 21-26. The average value for the modelled ratio over the period is 45.9 ppb, and the average measured mixing ratio is 42.1 ppb. Maximum modelled value is 65.2 ppb, while the measured data reach a maximum value of 89.2 ppb. The average modelled value at canopy height is 30.0ppb.....	64
Figure 4-5: Average diurnal variation of ozone mixing ratios (ppb) over the period May 21-26. Modelled (thick line) measured (thin line) and the modelled scaled to canopy height (stippled line). The correlation between measurements and modelled bottom layer mean is 0,94, and between measured and scaled modelled mean is 0.95, as it better accounts for night-time and early morning concentrations.....	65
Figure 4-6: Values for the total plant and soil conductance given as $1/rc$ (red line), and the seven different conductances it consists of. (R_s = stomatal resistance, R_m =combined stomatal and mesophyll resistance, R_{lu} = upper bulk canpy and healthy leaf cuticular resistance, R_b = resistance due to boyancy within the canopy, R_{cl} = lower canopy cuticular resistance, R_{ac} = resistance due to air transfer within the canopy, R_{gs} = resistance of soil and ground litter)	66
Figure 4-7: The total surface conductance given as $1/rc$ and the conductances of the different pathways it consists of.....	67
Figure 4-8: Stomatal flux modelled (thick line), and derived from measurements (thin line) in the period May 21-26. Average modelled value for daylit hours is $5.67 \text{ nmol m}^{-2}\text{s}^{-1}$, the average value derived from measurements during daylit hours is $5.24 \text{ nmol m}^{-2}\text{s}^{-1}$	68
Figure 4-9: Modelled stomatal flux (thick line, right axis) and surface temperature (thin line, left axis) for the period May 21-26. The stomatal conductance “cut-off-temperature” is 40°C , not reached on any of the days within this period.	69
Figure 4-10: Average diurnal variation of stomatal flux over the period May 21-26. Modelled (thick line) and derived from measurements (thin line). The correlation coefficient is 0,77. Correlation coefficient for only daylit hours is 0.75.....	70
Figure 4-11:Average ozone mixing ratio for the model bottom layer over the June-period (ppb).....	70
Figure 4-12: Ozone mixing ratios from measurements (thin line) and modelled (thick line) for the period June 23-28. The average value for the modelled bottom layer mixing ratio over the period is 40.9 ppb, and average measured mixing ratio is 43, 3 ppb. The modelled reference-height average is 30.8ppb	71
Figure 4-13:Measured wins speed and direction (top panel) and modelled windspeed and direction at 10m height (bottom panel), over the period May 21-26.	72

Figure 4-14: Average diurnal variation of ozone mixing ratios (ppb) over the period June 23-28. Modelled (thick line) and modelled derived from measurements (thin line), and the scaled ozone concentration at reference height (stippled line). The correlation coefficient is 0, 95 between the measured and the modelled bottom layer average, and the same (to two decimal round off) for the scaled concentration.	72
Figure 4-15: Total surface conductance and the seven conductances it consists of for the period June 23-28. (R_s = stomatal resistance, R_m =combined stomatal and mesophyll resistance, R_{lu} = upper bulk canopy and healthy leaf cuticular resistance, R_b = resistance due to buoyancy within the canopy, R_{cl} = lower canopy cuticular resistance, R_{ac} = resistance due to air transfer within the canopy, R_{gs} = resistance of soil and ground litter).....	73
Figure 4-16: The total surface conductance and the conductance of the four parallel pathways it consists of.....	74
Figure 4-17: Modelled stomatal flux (thick line, right axis) and surface temperature (thin line, left axis) for the period June 23-28. The stomatal conductance “cut-off-temperature” is 40°C.	75
Figure 4-18: Stomatal flux modelled (thick line), and derived from measurements (thin line) in the period June 23-28. The average value derived from WRF is 1.94 nmol/m ² s and the average flux derived from measurements is 1.94 nmol/m ² s. The average value for day lit hours derived from WRF is 3.6 nmol/m ² s and the average flux derived from measurements is 2.0 nmol/m ² s.	76
Figure 4-19: Average diurnal variation of stomatal flux over the period June 23-28. Modelled (thick line) and derived from measurements (thin line). The correlation coefficient is 0,03. The correlation coefficient for only the daytime hours is -0.37.	77
Figure 4-20: The influence of the VPD-function for the May-period (a.) and the June period (b). The top panels show the limiting effect of the VPD function on stomatal conductance, the middle panel show the f_{VPD} as a function of the calculated VPD (*), and the hourly modelled values for the stomatal conductance with (+), and without (o) the VPD function limitation. Bottom panels show the modelled flux with (thick line), and without VPD function limitations.	79
Figure 4-21: Modelled flux (thin line) and modelled flux limited by the sum VPD function with critical value 12kPa (thick line) for May 21-26 (top panel) and June 22-28 (bottom panel)....	80
Figure 4-22: Mean diurnal flux limited by VPD functions for May period (left) and June period (right). The top panels show mean diurnal flux limited by the VPD critical sum function, with the critical sum being 12kPa, compared to the average diurnal flux derived from measurements. Middle panels show diurnal flux limited by the f_{VPD} function from Gerosa et al. (2008), compared to the average diurnal flux derived from measurements. The bottom panels show the flux limited by both the VPD critical sum function and the f_{VPD} function compared to the average diurnal flux derived from measurements.....	81
Figure 4-23: The Southern African domain with the 24 USGS landuse categories.	83

Figure 4-24: Mean modelled bottom layer ozone mixing ratios over each month from October 2000 through April 2001. All mixing ratios are given in ppb.	85
Figure 4-26: The average surface temperature for the month of December (left) and April (right).....	87
Figure 4-25: Monthly average stomatal flux over the Southern African domain. All fluxes are given in nmol/m ² s.	87
Figure 4-27: The accumulated flux of O ₃ (mmol/m ²) above zero threshold value, over the day lit hours of the period 1.10.2000-30.4.2001.	88
Figure 4-28: The accumulated flux O ₃ above zero threshold over the maize growing season assumed estimated to the period 1.11.2000 to 30.2.2001.	89
Figure 4-29: Accumulated stomatal flux over the period October 1st 2000- April 30th 2001.	90
Figure 4-30: The difference in dose with and without the appliance of the sum-VPD function over the period 1.10.2000-30.4.2001. Notice the scale differs from the other dose presentations.....	91
Figure 4-31: The dose of ozone to vegetation accumulated over day lit hours from 1.11.2000-28.2.2001.	92
Figure 4-32: the Southern African domain with its 24 USGS landuse categories.	93
Table 2-1: Air quality standards and other indices used for ozone. (From Fowler et al. (2008))	12
Table 2-2: Global budget of NO _x in the Troposphere. (Brasseur et al. 1999).....	15
Table 2-3: Global Budget for Carbon Monoxide (Tg yr ⁻¹). Modified from Brasseur (1999) based on Khalil and Rasmussen (1990) and Bates et al. (1995).	16
Table 2-4: Estimated Sinks and Sources of Methane in the Atmosphere (Tg CH ₄ yr ⁻¹). (Modified from Brasseur (1999), from the IPCC (1994, 1996)).....	17
Table 2-5: Estimates of Global nmVOC Emissions (Tg C yr ⁻¹). Modified from Brasseur (1999), adapted from Singh and Zimmerman (1992), and Guenther et al. (1995).....	18
Table 3-1: Resolution, dimensions and timestep of each of the simulations.	43
Table 3-2: The choices for physics schemes made for the simulations in this study.	45
Table 3-3: USGS landuse categories and corresponding Wesely type and/or season.....	48
Table 4-1: Calculated correlation coefficient for the mean modelled fluxes limited by VPD functions, to the average flux values derived from measurements, for day lit hours.....	82

Table 4-2: Monthly peak and domain mean values for the modelled bottom layer ozone concentration.....	85
Table 4-3: Average values for the stomatal flux across the Southern African domain, with and without the limitations of the sum-VPD function. All values are given in nmol/m ² s.	91
Table 3-4: Integrals required to calculate cell average deposition velocity. (McRae, Goodin et al. 1982)	101

Bibliography

- Ashmore, M. R. (2005). "Assessing the future global impacts of ozone on vegetation." Plant Cell and Environment **28**(8): 949-964.
- Bolton, D. (1980). "The computation of equivalent potential temperature." Monthly Weather Review **108**(7): 1046-1053.
- Brasseur, G. P., J. J. Orlando, et al. (1999). Atmospheric Chemistry and Global Change. New York, Oxford University Press.
- Danielsson, H., G. P. Karlsson, et al. (2003). "Ozone uptake modelling and flux-response relationships--an assessment of ozone-induced yield loss in spring wheat." Atmospheric Environment **37**(4): 475-485.
- Danielsson, H., G. P. Karlsson, et al. (2003). "Ozone uptake modelling and flux-response relationships - an assessment of ozone-induced yield loss in spring wheat." Atmospheric Environment **37**(4): 475-485.
- Emberson, L. D., M. R. Ashmore, et al. (2000). Impacts of air pollutants on vegetation in developing countries. Meeting of the 6th International Conference on Acidic Deposition on Acid Rain 2000, Tsukuba, Japan, Kluwer Academic Publ.
- Emberson, L. D., M. R. Ashmore, et al. (2000). Modelling and mapping ozone deposition in Europe. 6th International Conference on Acidic Deposition, Tsukuba, Japan, Kluwer Academic Publ.
- Fowler, R. e. a. (2008). Ground-level ozone in the 21st century: future trends, impacts and policy implications. London, The Royal Society. **15/08**.
- Gerosa, G., A. Finco, et al. (2009a). "Interactions among vegetation and ozone, water and nitrogen fluxes in a coastal Mediterranean maquis ecosystem." Biogeosciences **6**(8): 1783-1798.
- Gerosa, G., A. Finco, et al. (2009b). "Comparison of seasonal variations of ozone exposure and fluxes in a Mediterranean Holm oak forest between the exceptionally dry 2003 and the following year." Environmental Pollution **157**(5): 1737-1744.
- Gerosa, G., R. Marzuoli, et al. (2008). "Visible leaf injury in young trees of *Fagus sylvatica* L. and *Quercus robur* L. in relation to ozone uptake and ozone exposure. An Open-Top Chambers experiment in South Alpine environmental conditions." Environmental Pollution **152**(2): 274-284.
- Gerosa, G., R. Marzuoli, et al. (2009c). "Validation of the stomatal flux approach for the assessment of ozone visible injury in young forest trees. Results from the TOP (transboundary ozone pollution) experiment at Curno, Italy." Environmental Pollution **157**(5): 1497-1505.
- Gerosa, G., R. Marzuoli, et al. (2010). Stomatal uptake of ozone in plants and its impacts. Brescia, Dipartimento di Matematica e Fisica, Università Cattolica del S.C.
- Gerosa, G., R. Marzuoli, et al. (2009d). "A flux-based assessment of the effects of ozone on foliar injury, photosynthesis, and yield of bean (*Phaseolus vulgaris* L. cv. Borlotto Nano Lingua di Fuoco) in open-top chambers." Environmental Pollution **157**(5): 1727-1736.
- Gerosa, G., M. Vitale, et al. (2005). "Ozone uptake by an evergreen Mediterranean Forest (*Quercus ilex*) in Italy. Part I: Micrometeorological flux measurements and flux partitioning." Atmospheric Environment **39**(18): 3255-3266.
- Grell, G. A., S. E. Peckham, et al. (2005). "Fully coupled "online" chemistry within the WRF model." Atmospheric Environment **39**(37): 6957-6975.
- Guenther, A., P. Zimmerman, et al. (1994). "Natural volatile organic-compound emission rate estimates for United-States woodland landscapes." Atmospheric Environment **28**(6): 1197-1210.
- Hayes, F., G. Mills, et al. (2007). Evidence of Widespread Ozone Damage to Vegetation in Europe (1990-2006). Thematic Reports. I. C. P. Vegetation. Bangor, UK, Centre for Ecology and Hydrology **November 2007**.

- Hicks, B. B., D. D. Baldocchi, et al. (1987). "A preliminary multiple resistance routine for deriving dry deposition velocities from measured quantities." Water Air and Soil Pollution **36**(3-4): 311-330.
- Hodnebrog, Ø. (2008). Impacts of fine scale variability on large scale atmospheric chemistry. Oslo, The University of Oslo.
- Jacob, D. J. (1999). Intoduction to Atmospheric Chemistry. Princeton, New Jersey, Princeton University Press.
- Janjic, Z. I. (2002). "Nonsingular Implementation of the Mellor-Yamada Level 2.5 Scheme in the NCEP Meso model." NCEP Office Note **No. 437**.: 61 pp.
- Jarvis, P. G. (1976). "Interpretation of variations in leaf water potential and stomatal conductance found in canopies in field." Philosophical Transactions of the Royal Society of London Series B-Biological Sciences **273**(927): 593-610.
- McKeen, S. A., G. Wotawa, et al. (2002). "Ozone production from Canadian wildfires during June and July of 1995." Journal of Geophysical Research-Atmospheres **107**(D14): 25.
- McRae, G. J., W. R. Goodin, et al. (1982). Mathematical modeling of Photochemical Air Pollution, California Institute of Technology.
- Middleton, P., W. R. Stockwell, et al. (1990). "Aggregation and analysis of volatile organic-compound emissions for regional modeling." Atmospheric Environment Part a-General Topics **24**(5): 1107-1133.
- Mills, G. (2004). Mapping critical levels for vegetation. Manual on Methodologies and Criteria for Mappig Critical Loads and Levels and Air Pollution Effects, Risks and Trends. UNECE, Convention on Long-range Transboundary Air Pollution. **Constantly updated version available at www.oekodata.com/icpmapping**.
- Mills, G., A. Buse, et al. (2007). "A synthesis of AOT40-based response functions and critical levels of ozone for agricultural and horticultural crops." Atmospheric Environment **41**(12): 2630-2643.
- Monteith, J. L. (1981). "Evaporation and surface temperature." Quarterly Journal of the Royal Meteorological Society **107**(451): 1-27.
- Nali, C., C. Pucciariello, et al. (2005). "On the different sensitivity of white clover clones to ozone: Physiological and biochemical parameters in a multivariate approach." Water Air and Soil Pollution **164**(1-4): 137-153.
- Nobel, P. S. (2005). Physiochemical and environmental plant physiology. Burlington, MA, Elsevier Academic Press.
- Peckham, S. E., Georg A. Grell, et al. (2009). WRF/Chem Version 3.1 User's Guide. WRF/Chem User's Guide
- Pleijel, H., H. Danielsson, et al. (2007). "Ozone risk assessment for agricultural crops in Europe: Further development of stomatal flux and flux-response relationships for European wheat and potato." Atmospheric Environment **41**(14): 3022-3040.
- RETRO. (2006). "REanalysis of the TROpospheric chemical composition over the past 40 years." from <http://retro.enes.org>.
- Schoenemeyer, T., K. Richter, et al. (1997). Vorstudie uber ein raumlich und zeitlich aufgelostes Kataster anthropogener und biogener Emissionen fuer Bayern mit Entwicklung eines Prototyps und Anwendung fur Immissionsprognosen. Abschluss bericht an das Bayerische Landesamt fur Umweltschutz. Garmisch-Partenkirchen, Fraunhofer-Institut fuer Atmosphaerische Umweltforschung
- Simpson, D. (1995). "Biogenic emissions in Europe. 2. Implications for ozone control strategies." Journal of Geophysical Research-Atmospheres **100**(D11): 22891-22906.
- Simpson, D., M. R. Ashmore, et al. (2007). "A comparison of two different approaches for mapping potential ozone damage to vegetation. A model study." Environmental Pollution **146**(3): 715-725.

- Sitch, S., P. M. Cox, et al. (2007). "Indirect radiative forcing of climate change through ozone effects on the land-carbon sink." Nature **448**(7155): 791-U4.
- Skamarock, W. C., J. B. Klemp, et al. (2008). A Description of the Advanced Research WRF Version 3. NCAR TECHNICAL NOTE. Boulder, Colorado, USA, National Center for Atmospheric Research. **June 2008**.
- Van Dingenen, R., F. J. Dentener, et al. (2009). "The global impact of ozone on agricultural crop yields under current and future air quality legislation." Atmospheric Environment **43**(3): 604-618.
- Wallace, J. M. and P. V. Hobbs (2006). Atmospheric Science, Elsevier Academic press.
- Wang, W., C. Bruyère, et al. (2010). ARW Version 3 Modeling System User's Guide, National Center for Atmospheric Research
- Wesely, M. L. (1989). "Parameterization of surface resistances to gaseous dry deposition in regional-scale numerical-models." Atmospheric Environment **23**(6): 1293-1304.
- Wesely, M. L. and B. B. Hicks (1977). "Some factors that affect deposition rates of sulfur-dioxide and similar gases on vegetation." Journal of the Air Pollution Control Association **27**(11): 1110-1116.
- Wexler, A. (1976). "Vapor-pressure formulation for water in range 0 to 100 degreesC - revision." Journal of Research of the National Bureau of Standards Section a-Physics and Chemistry **80**(5-6): 775-785.
- Wicker, L. J. and W. C. Skamarock (2002). "Time splitting methods for elastic models using forward time schemes." Mon. Wea. Rev **130**: 2088-2097.
- Zunckel, M., A. Koosailee, et al. (2006). "Modelled surface ozone over southern Africa during the Cross Border Air Pollution Impact Assessment Project." Environmental Modelling & Software **21**(7): 911-924.